RSC Advances

ROYAL SOCIETY OF CHEMISTRY

PAPER

View Article Online
View Journal | View Issue

Check for updates

Cite this: *RSC Adv.*, 2026, **16**, 18022

First-principles investigation and device simulation of $TlPbI_3$-based perovskite solar cells with machine learning-driven efficiency prediction

Md. Harun-Or-Rashid, *[a] Hanane Etabti,[b] Md. Tauki Tazwar,[c] Md Amzad Sadik Abid,[d] Md Farhan Shahriyar, [e] Nosir Khurramov,[f] Hayitov Abdulla Nurmatovich,[g] Sardor Sabirov,[h] Lakhdar Benahmedi, [i] Md. Monirul Islam [a] and Md. Ferdous Rahman [a]

The development of sustainable, cost-effective, and environmentally friendly photovoltaic absorbers is essential for advancing next-generation solar cell technologies. In this study, we investigate the thallium-based halide perovskite $TlPbI_3$ through a synergistic combination of density functional theory (DFT), solar cell capacitance simulator in one dimension (SCAPS-1D) device simulation, and machine learning (ML). Structural optimization, tolerance factor, formation energy, and phonon dispersion curve confirmed the structural, dynamic, thermodynamic, and mechanical stability of cubic $TlPbI_3$, with elastic constants fulfilling Born's stability criteria. The calculated direct band gap of 1.26 eV at the *R* point falls within the optimal range for single-junction photovoltaics. Charge density mapping indicated mixed ionic-covalent bonding, ensuring structural robustness. Mechanical analysis confirmed ductility and thermal stability, with an estimated melting temperature of ~757 K. Optical results showed strong absorption in the visible region, a high static dielectric constant ($\varepsilon_0 \approx 4.6$), and low reflectivity, underlining the suitability of $TlPbI_3$ for optoelectronic devices. SCAPS-1D simulations were performed on different heterojunction configurations, optimizing absorber thickness, doping density, defect density, and buffer layers. The best-performing device, fluorine-doped tin oxide (FTO)/cadmium sulfide (CdS)/thallium lead triiodide ($TlPbI_3$)/copper (Cu), delivered a power conversion efficiency (PCE) of 22.20% with open-circuit voltage (V_{OC}) = 0.7987 V, short-circuit current density (J_{SC}) = 34.56 mA cm^{-2}, and fill factor (FF) = 80.40%, confirming the strong photovoltaic potential of $TlPbI_3$. Machine learning models, trained on simulation datasets, successfully identified absorber thickness and defect density as the most critical factors influencing device performance. This integrated computational framework demonstrates the potential of $TlPbI_3$ as a viable absorber material for next-generation solar cells and provides valuable predictive insights to guide experimental development.

Received 13th February 2026
Accepted 26th March 2026

DOI: 10.1039/d6ra01288d

rsc.li/rsc-advances

1 Introduction

The rapid growth of global energy demand, combined with the urgent need to mitigate climate change, has intensified the search for renewable energy technologies that are sustainable, efficient, and environmentally friendly.[1] Solar photovoltaics (PV) have emerged as a central pillar in this transition due to their ability to directly harvest energy from the sun. However, traditional PV technologies, particularly crystalline silicon, still suffer from several limitations, including high production costs, energy-intensive fabrication processes, and reliance on relatively complex infrastructures.[2,3] Alternative thin-film technologies such as cadmium telluride (CdTe) and copper indium gallium selenide (CIGS), although efficient, face challenges associated with material scarcity.[4] Thus, the development of next-generation absorber materials that are low-cost, abundant, and easily processable has become a critical necessity for

---

[a] Department of Electrical and Electronic Engineering, Begum Rokeya University, Rangpur 5400, Bangladesh. E-mail: harunorrashid1816017@gmail.com

[b] LIMAS, Faculty of Sciences Dhar El Mahraz, Sidi Mohamed Ben Abdellah University, Fez 30000, Morocco

[c] Department of Electrical and Electronic Engineering, Bangladesh Army University of Science and Technology (BAUST), Saidpur 5311, Nilphamari, Bangladesh

[d] Department of Information Systems, Lamar University, Beaumont, Texas 77705, USA

[e] Department of Computer Science and Engineering, Hajee Mohammad Danesh Science and Technology University, Dinajpur-5200, Bangladesh

[f] Department of Information Technology and Exact Sciences, Termez University of Economics and Service, Termez 190100, Uzbekistan

[g] Department of Technical Science, Urgench State University, Urgench 220100, Uzbekistan

[h] Department of General Professional Sciences, Mamun University, Khiva 220900, Uzbekistan

[i] Technology and Solids Properties Laboratory, Faculty of Science and Technology, Mostaganem University, Mostaganem 27000, Algeria

advancing the deployment of solar energy on a global scale. Such materials would not only support large-scale power generation but also broaden the applications of PV technologies in flexible, wearable, and embedded systems.

Within this context, metal halide perovskites have attracted considerable attention over the past decade as promising alternatives to traditional absorbers.[5] Perovskites with the general formula ABX_3, where A is a monovalent cation, B is a metal cation, and X is a halide anion, exhibit a unique combination of optoelectronic properties that make them highly suitable for solar cell applications.[6,7] Their exceptional light-harvesting ability, tunable band gaps, defect tolerance, and long carrier diffusion lengths have enabled rapid progress in PCEs, which increased from 3.8% in 2009 to over 27% in recent years.[8] Furthermore, their solution processability and compatibility with low-temperature fabrication methods point toward low production costs and large-scale manufacturability. For these reasons, halide perovskites are increasingly considered as strong candidates to complement or even replace traditional materials in photovoltaic applications.[9,10]

Numerous studies have explored the potential of perovskite compounds, and a significant body of literature has demonstrated their versatility. Kojima *et al.* first introduced organometal halide perovskites as sensitizers in dye-sensitized solar cells, marking the beginning of this field.[11] Subsequent studies by Zhou *et al.*, Parket *et al.*, Snaithet *et al.*, and Green *et al.* further documented their remarkable efficiency improvements and device stability challenges[12–15] More recently, Jacob *et al.* employed DFT to screen several of the perovskite compositions, identifying stable and non-toxic candidates.[16] Li *et al.* introduced ML models trained on experimental data points to guide material selection and device design.[17] Additional works by Kulkarni *et al.*, Noh *et al.*, Yoo *et al.*, and Duan *et al.* have examined the structural, optical, and electronic behavior of halide perovskites, revealing both their advantages and their persistent challenges in stability and toxicity. Together, these studies have laid the foundation for both computational and experimental advances in perovskite photovoltaics[18–21] Among the many families of perovskite compounds, thallium-based perovskites have only recently begun to attract attention. In particular, $TlPbI_3$ has been identified as a candidate absorber with unique optoelectronic features. Liu *et al.* performed a first-principles study of $TlPbI_3$, reporting a band gap of approximately 1.33 eV, which is close to the optimal value for single-junction solar cells.[22] They also highlighted its improved structural stability compared with other inorganic halide perovskites. Lin *et al.* demonstrated that $TlPbI_3$ single crystals possess wide band gaps and high densities, making them suitable for ionizing radiation detection, though their optical properties remain promising for PV applications.[23] More recently, Yan *et al.* investigated the layered form of $TlPbI_3$ and showed how lattice contraction affects band dispersion and carrier effective masses, revealing the potential of structural engineering to tune its electronic performance.[24] These results suggest that thallium-based perovskites, despite being less widely studied than lead or tin perovskites, could offer valuable opportunities in the search for efficient and stable absorber materials.

In the present study, we build on this growing body of research by adopting a combined approach that integrates first-principles density functional theory, SCAPS-1D device simulation, and machine learning techniques. DFT provides detailed insights into the fundamental structural, electronic, and optical properties of $TlPbI_3$, while SCAPS-1D enables the evaluation of realistic device configurations, accounting for absorber thickness, defect densities, and interface properties. Machine learning, in turn, accelerates the screening and prediction of performance trends, helping to identify the most critical parameters and guiding further optimization. Similar strategies have recently been employed by researchers such as Moulebhar *et al.*, Jacobs *et al.*, and other groups that successfully combined computational materials design with ML models to predict stability and efficiency.[16,25,26] Our approach follows this line of research but extends it to the case of thallium-based perovskites, where relatively little systematic work has been reported to date. The motivation for our work lies in addressing two main gaps. First, despite promising results from theoretical studies, $TlPbI_3$ remains poorly understood in terms of its performance in solar cell devices. By combining DFT with SCAPS, we provide insights that directly link material properties to device-level behavior. Second, while machine learning has been applied to broader classes of perovskites, few studies have targeted Tl-based compounds specifically. By integrating ML into our investigation, we aim to accelerate the understanding of this material and provide predictions that can guide future experimental efforts.

2 Computational methods

2.1 DFT analysis

The investigation of $TlPbI_3$ was conducted utilizing first-principles density functional theory (FP-DFT) based on the Perdew–Burke–Ernzerhof (PBE)[27] exchange–correlation functional in combination with norm-conserving (NC) pseudopotentials[28–30] All computational analyses were executed using the Quantum ESPRESSO (QE) simulation package.[27,31] To explore the structural, mechanical, electronic, and optical characteristics of the material, an optimised Monkhorst–Pack k-point mesh of $3 \times 3 \times 3$ was employed (shown in Fig. 1(c)). The optimised kinetic energy and charge density cut-off values were set at 50 Rydberg (Ry) (shown in Fig. 1(d)) and 350 Rydberg (Ry), respectively. The optimization process maintained a maximum force threshold of less than 3.89×10^{-4} Ry Bohr^{-1}, while the self-consistent field (SCF) calculations achieved convergence with a precision limit of 10^{-6} atomic units. During the relaxation stage, a tighter convergence tolerance of 10^{-4} atomic units was applied to ensure numerical accuracy and structural stability.

2.2 SCAPS-1D analysis

In this study, the solar cell configuration comprising FTO/(CdS/In_2S_3/SnS_2)/$TlPbI_3$/Cu was designed and analyzed through

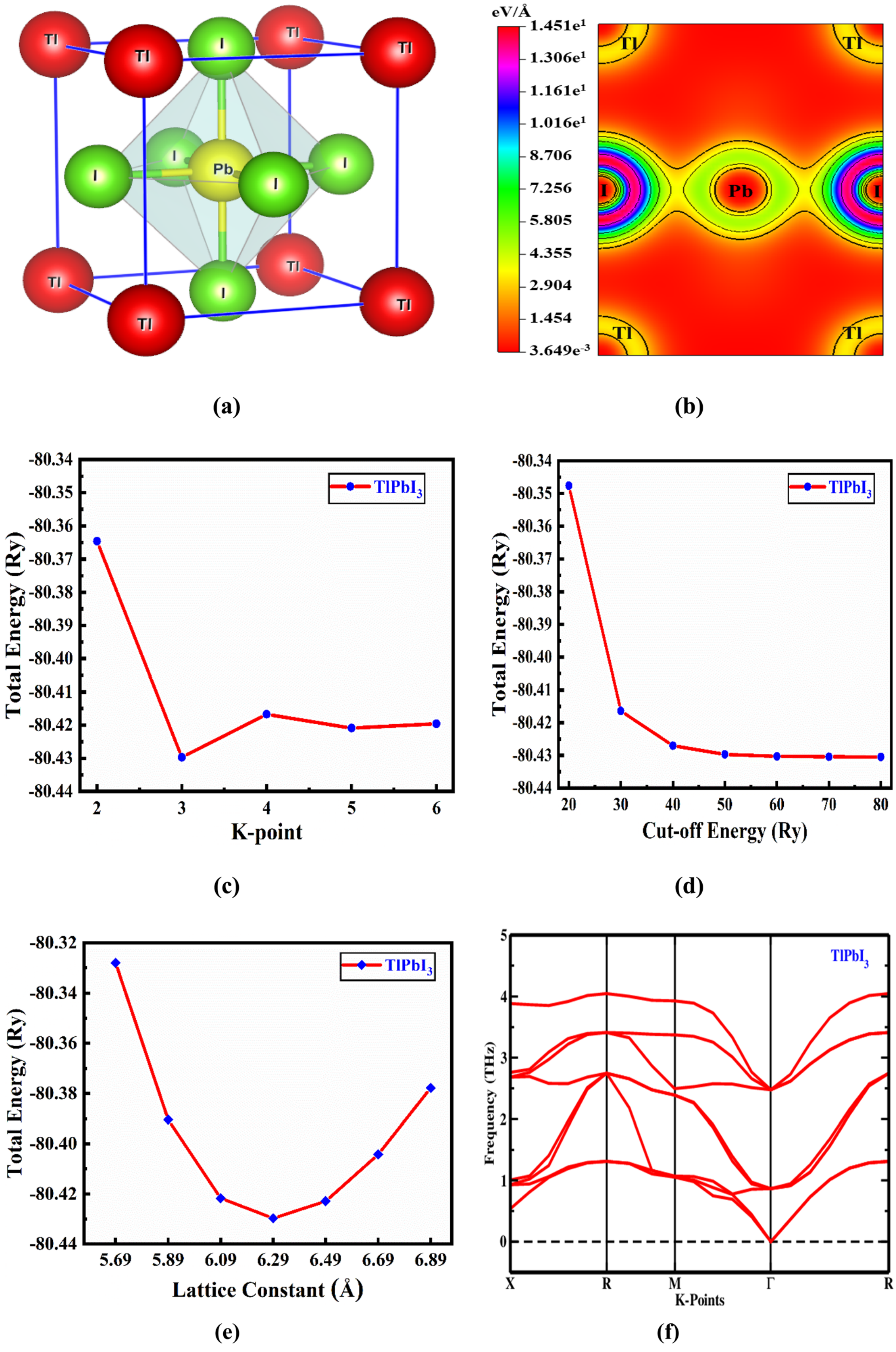

Fig. 1 The (a) crystal structure, (b) charge density mapping, (c) k-point optimization, (d) kinetic cut-off energy optimization, (e) lattice constant optimization, and (f) phonon dispersion curve of $TlPbI_3$ perovskite.

numerical modeling using the SCAPS-1D, version 3.3.0.12. This simulation tool was originally developed by the Department of Electronics and Information Systems (ELIS) at Ghent University, Belgium.[32,33] The SCAPS-1D framework allows the incorporation of up to seven distinct layers, including six interfaces and two electrode contacts.[34] It is widely adopted in photovoltaic research due to its strong consistency between simulated outputs and experimental data.[35] The program determines essential photovoltaic parameters—such as PCE, V_{OC}, J_{SC}, and FF—by solving fundamental semiconductor equations, including the Poisson equation, carrier continuity equations, and current density equations. These equations are numerically computed to simultaneously resolve the electron and hole transport through both the continuity and Poisson relations:[36–40]

$$\frac{\partial^2\psi}{\partial x^2} = -\frac{\partial E}{\partial x} = -\frac{\rho}{\varepsilon_r\varepsilon_0} = -\frac{q}{\varepsilon_s}\left[p(x) - n(x) + N_D{}^+(x) - N_D{}^-(x) + p_t(x) - n_t(x)\right] \quad (1)$$

$$\frac{\partial j_n}{\partial x} = q\left(R_n - G + \frac{\partial n}{\partial t}\right) \quad (2)$$

$$\frac{\partial j_p}{\partial x} = -q\left(R_p - G + \frac{\partial p}{\partial t}\right) \quad (3)$$

In the aforementioned equations, each symbol carries a distinct physical meaning. The parameter ψ denotes the electrostatic potential, while q corresponds to the elementary charge. The symbol ε_s signifies the dielectric permittivity of the semiconductor medium, expressed as $(\varepsilon_r\varepsilon_0)$. The variables p and n represent the respective concentrations of holes and electrons, whereas N_D and N_A refer to the donor and acceptor doping densities. Similarly, p_t and n_t indicate the densities of trapped holes and trapped electrons. The term G describes the generation rate of charge carriers, and R_p and R_n correspond to the recombination rates of holes and electrons, respectively. Moreover, j_p and j_n denote the current densities associated with holes and electrons. Eqn (4) and (5) mathematically express the hole and electron current densities as:[39,41]

$$j_p = q\left(n\mu_p E - D_p\frac{\partial p}{\partial x}\right) \quad (4)$$

$$j_n = q\left(n\mu_n E + D_n\frac{\partial n}{\partial x}\right) \quad (5)$$

Here, μ_p and μ_n signify the mobilities of holes and electrons, respectively, while D_p and D_n represent the corresponding diffusion coefficients of holes and electrons within the semiconductor medium.

2.3 Machine learning analysis

Random Forest (RF), Gradient Boosting (GB), Decision Tree (DT), and Light Gradient Boosting Machine (LightGBM) are all powerful ensemble machine-learning algorithms that combine multiple decision trees to improve model accuracy and generalization. The Random Forest algorithm utilizes a bagging (bootstrap aggregating) strategy, in which numerous decision trees are constructed independently using different random subsets of the training data. At each decision node, a random subset of features is selected to ensure diversity among trees and reduce overfitting.[42] For regression problems, the final model prediction is obtained by averaging the outputs of all trees, expressed mathematically as:[42]

$$F(x) = \frac{1}{M}\sum_{m=1}^{M} h_m(x) \quad (6)$$

where $h_m(x)$ represents the prediction made by the m-th tree, and M denotes the total number of trees in the ensemble.

Gradient boosting adopts a boosting approach, constructing trees in a sequential manner such that each subsequent tree attempts to correct the residual errors of the preceding ensemble by minimizing a specific loss function through gradient descent optimization.[43] The iterative model update can be represented as:

$$F_m(x) = F_{m-1}(x) - \eta\frac{\partial L(y, F_{m-1}(x))}{\partial F_{m-1}(x)} \quad (7)$$

where η refers to the learning rate, controlling the contribution of each tree, and L is the designated loss function that guides the model toward minimizing prediction errors.

A decision tree is a supervised machine learning algorithm that uses a hierarchical tree structure to classify or predict outcomes based on a set of rules. It works by recursively splitting data into subsets based on feature values until each subset belongs to the same class. The splitting criterion uses Information Gain, calculated as:[44]

$$\text{Information gain} = \text{etrophy(parent)} - \sum\frac{n_{\text{child}}}{n_{\text{arent}}} \times \text{etrophy(child)} \quad (8)$$

where entropy measures the randomness in the data.

LightGBM is a high-performance gradient Boosting framework developed by Microsoft that builds upon decision tree algorithms. Unlike traditional level-wise tree growth, LightGBM uses leaf-wise growth, selecting the leaf with the maximum loss reduction to split next. Key innovations include Gradient-based One-Side Sampling (GOSS) and Exclusive Feature Bundling (EFB) for efficiency. The split gain is computed as:[45]

$$\text{Gain} = \frac{g_L{}^2}{h_L + \lambda} + \frac{g_R{}^2}{h_R + \lambda} - \frac{(g_L + g_R)^2}{h_L + h_R + \lambda} \quad (9)$$

where g represents gradient sums, h represents Hessian sums, and λ is the regularization parameter. LightGBM achieves up to 20× faster training than conventional GB and DT while maintaining similar accuracy.

3 Result and discussion

3.1 Structural properties and electron charge density

Thallium lead iodide ($TlPbI_3$) is a fully inorganic metal halide compound that crystallizes in a cubic structure belonging to the *Pm*-3*m* (No. 221) space group. The fundamental unit cell of this crystal consists of five atoms arranged in a perfectly symmetric configuration. In this lattice framework, the Pb atom occupies the 1b site (0.5, 0.5, 0.5), while the Tl atom resides at the 1a site (0, 0, 0). The three iodine (I) atoms are situated at the 3c sites (0, 0.5, 0.5), completing the overall atomic geometry of the crystal. A schematic illustration of this ordered cubic structure is

Table 1 Goldschmidt tolerance factor, octahedral factor, band gap, lattice constant, and formation energy for $TlPbI_3$ and comparable perovskites

Material	r_A	r_B	r_X	Goldschmidt tolerance factor, t	Octahedral factor, of	Bandgap (eV)	Lattice constant (Å)	Formation energy, ΔE_f (eV per atom)	Ref.
$TlPbI_3$	1.50	1.19	2.20	0.77	0.54	1.26 (PBE), 1.82 (HSE), 0.35 (SOC + PBE)	6.29	−2.466	This work
$TlPbI_3$	—	—	—	—	—	1.92 (HSE)	6.33	−0.584	59
$InPbI_3$	—	—	—	—	—	1.23 (PBE), 1.898 (HSE)	6.28	−2.435	57
$GaPbI_3$	—	—	—	—	—	1.30 (PBE)	6.35	−1.600	60
$AlPbI_3$	—	—	—	—	—	1.784 (HSE)	6.303	−0.181	59
$CsPbI_3$	—	—	—	0.81	—	1.28 (PBE)	6.336	−0.028	61
$RbPbI_3$	1.63	1.17	2.20	0.803	0.53	1.50 (PBE)	6.178	−0.0155	61

presented in Fig. 1(a), highlighting the spatial distribution of each atomic constituent within the lattice. Through first-principles computational analysis, the optimized lattice constant of $TlPbI_3$ was determined to be approximately 6.29 Å, indicating its compact and symmetric crystalline framework, as shown in Fig. 1(e).

The formation probability of a perovskite crystal structure is often assessed using two key geometric parameters – the Goldschmidt tolerance factor (t) and the octahedral factor (OF).[46] These empirical parameters serve as predictive indicators of the structural stability of perovskites and can be calculated using the following relationships:[47–52]

$$t = \left(\frac{r_A + r_X}{\sqrt{2}(r_B + r_X)}\right) \tag{10}$$

$$OF = \frac{r_B}{r_X} \tag{11}$$

Here, r_X represents the ionic radius of the halide anion (I^-), r_B denotes the ionic radius of the divalent metal cation (Pb^{2+}), and r_A corresponds to the ionic radius of the monovalent cation (Tl^+). For a stable perovskite phase to form, the t typically lies within the range of 0.7–1.0, while the OF generally falls between 0.29 and 0.55.[8,49,51,53] The computed t for $TlPbI_3$ is found to be 0.77, whereas the corresponding OF is 0.54. These numerical values confirm that $TlPbI_3$ maintains a cubic perovskite crystal symmetry, consistent with the stability range typically observed for such structures.

The formation energy (ΔE_f) serves as an essential parameter for evaluating the chemical and thermodynamic stability of perovskite compounds, as outlined in:[54,55]

$$\Delta E_f(TlPbI_3) = \frac{[E_{total}(TlPbI_3) - E_s(Tl) - E_s(Pb) - 3E_s(I)]}{N} \tag{12}$$

Here, N represents the total number of atoms within the unit cell, while E_{total} ($TlPbI_3$) corresponds to the overall energy of the $TlPbI_3$ perovskite structure. Similarly, E_s (Tl), E_s (Pb), and E_s (I) denote the individual atomic energies of Tl, Pb, and I, respectively. The computed values of the formation energy, ΔE_f (eV per atom), are summarized in Table 1. A negative formation energy value reflects the energetic favorability and intrinsic stability of the compound, signifying that $TlPbI_3$ can be experimentally synthesized under ambient conditions without spontaneous decomposition.[54–56] Fig. 1(f) shows the phonon dispersion of $TlPbI_3$, which is used to assess its dynamical stability. Phonon dispersion represents the variation of vibrational frequencies with wave vectors in the crystal lattice.[57,58] The absence of imaginary (negative) frequencies indicates that all vibrational modes are stable, confirming that $TlPbI_3$ is dynamically stable and not prone to spontaneous structural distortions or lattice collapse.[57,58] Furthermore, a comprehensive evaluation encompassing the tolerance factor, octahedral factor, electronic bandgap, lattice parameter, formation energy, and bond length of this compound is systematically summarized in Table 1, providing deeper insight into its structural and electronic characteristics.

To clarify the magnetic nature of $TlPbI_3$, both non-spin-polarized and spin-polarized calculations were carried out. The total energy of the non-magnetic (NM) configuration was found to be −80.42968 Ry, while the ferromagnetic (FM) trial configuration gave −80.42957 Ry. The NM configuration is the most stable phase, since its total energy is slightly lower than that of the FM state. In the spin-polarized calculation, both the total and absolute magnetic moments converged to 0 Bohr magneton per cell, demonstrating that no stable local or long-range magnetic ordering is present. These results confirm that $TlPbI_3$ has a nonmagnetic ground state within the present DFT calculations.

The charge density map shows important bonding details by showing electron charge patterns on different crystallographic planes. The (110) plane within $TlPbI_3$ displays a specific charge arrangement as shown in Fig. 1(b). The color representation of electron density distribution shows red for high-density regions and blue for low-density areas within the crystal structure. The spherical charge distribution of Tl and I atoms fails to intersect along the (110) plane because this arrangement indicates that they form an ionic bond. The ionic nature becomes more evident because Tl and Pb atoms display noticeably different electron densities. The elliptical bonding areas between Pb and I demonstrate covalence because their mutual electron charge sharing happens within the same plane of the molecular structure. The I ions possess the highest electron concentration

Table 2 Elastic properties of the cubic $TlPbI_3$ and other perovskites from the GGA functional

Parameters	$TlPbI_3$	$InPbI_3$ (ref. 57)	$InGeCl_3$ (ref. 62)
C_{11} (GPa)	34.5690	36.4715	46.02
C_{12} (GPa)	2.8775	2.4397	11.02
C_{44} (GPa)	2.8112	2.5414	10.50
Cauchy pressure, C_P (GPa)	0.0663	−0.1017	0.52
Bulk modulus, B (GPa)	13.4413	13.7836	22.69
Shear modulus, Gs (GPa)	6.1074	6.0916	12.90
Young's modulus, Y (GPa)	15.9123	15.9284	31.53
Poisson's ratio, ν	0.3027	0.3073	0.261
Pugh ratio, B/Gs	2.2008	2.2627	—
Anisotropy factor (A)	0.1774	0.1493	—
Melting temperature, T_m (K)	757.3028	768.5468	—

within specific regions of the crystals, while Tl ions demonstrate the lowest electron density according to charge density maps.

3.2 Mechanical properties

To determine whether a material functions as intended for real applications, engineers need to understand its basic mechanical characteristics. The cubic crystal system requires three elastic constants C_{11}, C_{12} and C_{44} for evaluating its structural stability levels. The satisfaction of the following conditions establishes material mechanical stability:[58]

$$C_{11} - C_{12} > 0,\ C_{11} + 2C_{12} > 0,\ \text{and}\ C_{44} > 0 \tag{13}$$

The values of C_{11}, C_{12}, and C_{44} for $TlPbI_3$ appear in Table 2. All stability conditions used to determine mechanical stability are met by these values, which show that $TlPbI_3$ achieves mechanical stability during equilibrium conditions.

A number of mechanical moduli, such as the bulk modulus, shear modulus, Pugh ratio, Young's modulus, and Poisson's ratio, were calculated from the elastic constants C_{ij}, and are shown in Table 2. These moduli offer more detailed information about the material's mechanical response. They used the following equations in their computations, which were based on the Voigt–Reuss–Hill (V.R.H.) averaging method:[63,64]

$$B = \frac{1}{2}(B_R + B_V) \tag{14}$$

$$G_s = \frac{1}{2}(G_R + G_V) \tag{15}$$

$$Y = \frac{9BGs}{3B + Gs} \tag{16}$$

$$\nu = \frac{(3B - 2Gs)}{2(3B + Gs)} \tag{17}$$

$$C_P = C_{12} - C_{44} \tag{18}$$

The bulk modulus defines how much materials oppose uniform compression. A high B value indicates strong resistance of materials to volumetric changes that occur under pressure. Studies presented in Table 2 prove that $TlPbI_3$ exhibits maximum resistance when compressed.

Eqn (15) provides the calculation method for determining the material's shear deformation resistance through the shear modulus. The material exhibits superior rigidity when its Gs value becomes higher. The material $TlPbI_3$ demonstrates high resistance to shear forces because of its mechanical durability properties.

The relation between shear and bulk moduli exists in Young's modulus, which defines material stiffness according to eqn (16). The stiffness of a material increases when its Y value reaches higher levels.

The material's lateral deformation behavior during stretching and compression can be evaluated through Poisson's ratio, which is derived from eqn (17). A material exhibits strong interatomic bonding and shows elastic flexibility when its measured Poisson ratio falls between 0.25 and 0.50. The elastic properties of $TlPbI_3$ demonstrate a proper balance according to the established range.

Ductility and malleability assessment requires evaluation through Cauchy pressure using eqn (18) combined with the Pugh ratio (with threshold 1.75).[65] $TlPbI_3$ behaves as a ductile material because its Pugh ratio of 1.75 and positive Cauchy pressure values present in Table 2 indicate so.

The elastic anisotropy factor, determined using eqn (19),[66] highlights direction-dependent mechanical properties:

$$A = \frac{2C_{44}}{C_{11} - C_{12}} \tag{19}$$

when the A value reaches 1, the material achieves a complete isotropic state, so any deviation indicates anisotropy.[67] $TlPbI_3$ demonstrates mechanical anisotropy because its A value stands at 0.17.

The determination of thermal conductivity and bonding strength depends on the melting temperature measurement that closely correlates with the elastic properties of the material. The estimation of melting temperature for cubic materials uses eqn (20),[68,69] as follows:

$$T_m = 553 + 5.91C_{11} \tag{20}$$

Based on this relation, the $TlPbI_3$ crystal is anticipated to melt at 757.302 K, which makes it suitable for high-temperature optoelectronic functions. The substance demonstrates effective

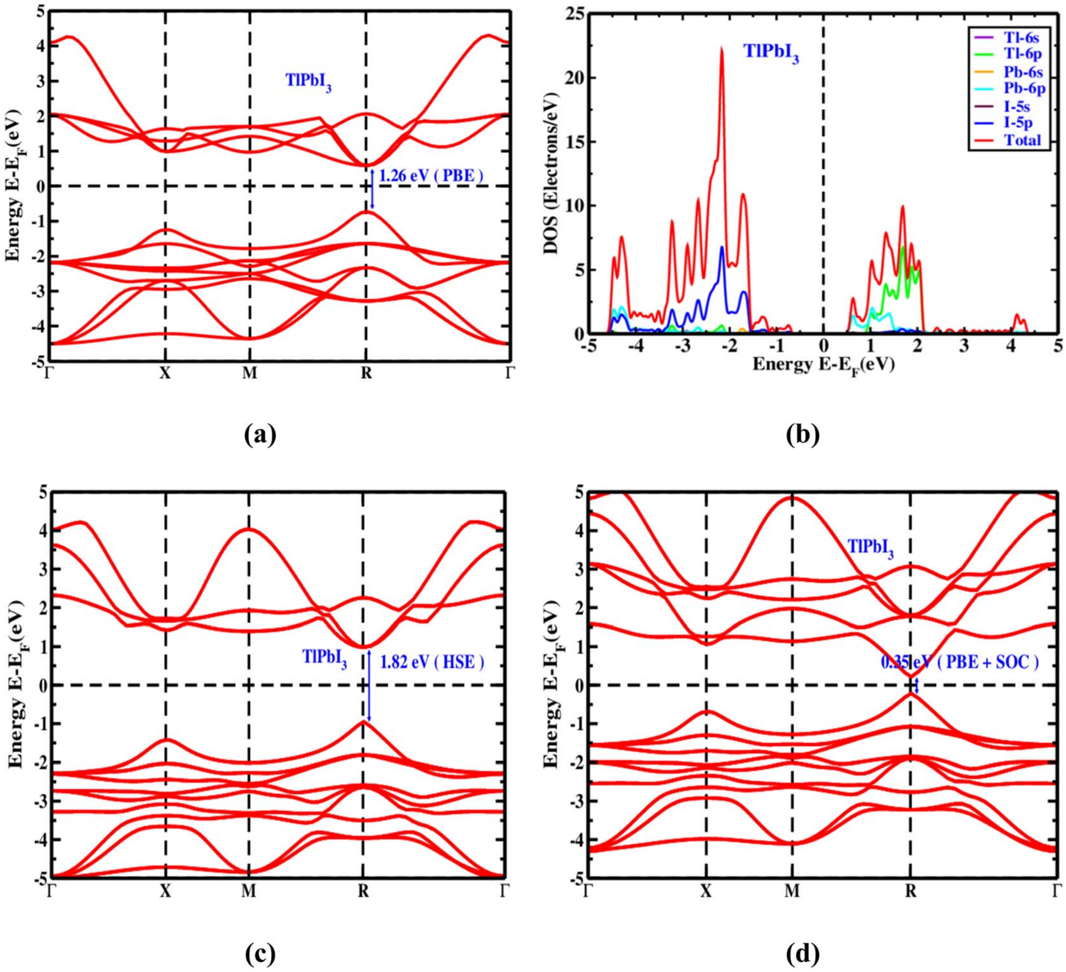

(a) (b)

(c) (d)

Fig. 2 (a) Energy band structure in PBE, (b) DOS in PBE, (c) electronic band structure in HSE, and (d) electronic band structure including spin–orbit coupling in the PBE, of the optimized inorganic perovskite TlPbI$_3$ structure.

atomic bonds and outstanding thermal conductive properties through its high melting temperature.

3.3 Electronic properties

3.3.1 Band structure, density of state (DOS), and electron affinity. The evaluation of electronic band structure enables researchers to study fundamental properties of materials together with their optical functions and charge transfer capabilities.[70,71] The band structure calculation of TlPbI$_3$ by the PBE method follows the Brillouin Zone path between *Γ*–*X*–*M*–*R*–*Γ* points, as shown in Fig. 2(a). The energy levels range between −5 to +5 eV at a Fermi level of 0 eV. Above the Fermi level exists the conduction band as well as the valence band below it. When energy reaches the *R* point, TlPbI$_3$ shows a 1.26 eV direct band gap because the maximum of the valence band and the minimum of the conduction band align precisely. This direct gap between bands results in strong light absorption capabilities that make the material suitable for producing efficient power generation. The absorption capabilities in visible light, together with minimized thermalization losses, provide extended efficiency for turning light into electricity. The combination of high electron mobility alongside its effective light emission properties makes TlPbI$_3$ suitable for various electronic and optoelectronic applications.[72,73] It should be noted that the PBE functional is known to underestimate the band gap of halide perovskites due to the intrinsic limitations of semilocal exchange-correlation approximations. To obtain a more accurate description of the electronic structure, the HSE06 hybrid functional was also employed, and the calculated band gap increases to 1.82 eV, as shown in Fig. 2(c), confirming the well-known underestimation of band gaps by the PBE functional. In addition, when spin–orbit coupling (SOC) is included within the PBE framework, the band gap is significantly reduced to 0.35 eV, as illustrated in Fig. 2(d). This strong reduction originates from the relativistic SOC effect associated with the heavy Tl and Pb atoms, which induces spin–orbit-driven splitting together with upward and downward shifts of the valence- and conduction-band states, thereby reducing the energy difference between the VBM and CBM.

The density of states (DOS) offers crucial insights into the distribution of electronic states and their roles in the valence and conduction bands. The density of states provides visible evidence about electron energy states that exist and are occupied inside solid materials. Scientific research utilizing DOS allows experts to identify electronic state quantities across numerous energy levels to study material properties better. Fig. 2(b) shows the complete and segmented DOS of $TlPbI_3$. The vertical dotted line representing the Fermi level (E_F) separates the material into the valence band on its left side and the conduction band on its right side. The analysis area stretches over −5 to +5 eV in the *x*-axis dimension, while the DOS scale reaches 25 states per eV in the *y*-axis range. In the density of states profile of $TlPbI_3$, the most intense valence-band contribution is located between −2.0 and −2.5 eV, with a maximum magnitude of approximately 22.5 electrons eV^{-1} (equivalent to 1.423×10^{19} cm^{-3}). On the conduction-band side, the DOS attains a peak value of about 10.587 electrons eV^{-1}, corresponding to 6.701×10^{18} cm^{-3}. The majority of valence band orbitals come from Iodine's I-5p orbitals, whereas the main composition of conduction band orbitals stems from Thallium's Tl-6p orbitals. The Pb-6p state functions as an important component that determines how $TlPbI_3$ constructs its total electronic structure. Electron affinity refers to the energy change, expressed in electronvolts, associated with the attachment of an electron to a neutral atom or molecule, and it plays a key role in determining the energy-level alignment between the absorber layer and the electron transport layer, thereby governing the efficiency of electron extraction and transport.[57] For the present material, the computed electron affinity is 3.75 eV, a value that is highly favorable for efficient operation in solar cell devices.

3.3.2 Electron and hole mobility. In photovoltaic absorber materials, both electron and hole mobilities are critical parameters because higher carrier mobility facilitates faster charge transport and reduces recombination losses, ultimately leading to improved device efficiency.[57] The mobility of charge carriers can be evaluated using the relation,[57]

$$\mu = \frac{\tau \times q}{m^*} \tag{21}$$

where μ denotes the carrier mobility ($cm^2\ V^{-1}\ s^{-1}$), τ represents the relaxation time, $q = 1.602 \times 10^{-19}$ C is the elementary charge, and m^* is the effective mass expressed in kilograms.

In order to determine the effective masses of holes (m_h^*) and electrons (m_h^*), the band structure data in the vicinity of the Brillouin zone *R* point were analyzed. The second-order derivatives of the valence band maximum and conduction band minimum with respect to the wave vector *k* were evaluated at the *R* point. For $TlPbI_3$, the calculated electron and hole effective masses are 0.19 m_0 (1.73×10^{-31} kg) and 0.23 m_0 (2.10×10^{-31} kg), respectively. These effective masses correspond to relaxation times of 8.7×10^{-15} s for electrons and 7.9×10^{-15} s for holes, yielding carrier mobilities of approximately 91.9 $cm^2\ V^{-1}\ s^{-1}$ for electrons and 75.9 $cm^2\ V^{-1}\ s^{-1}$ for holes.

3.4 Optical properties

Light-absorbing materials together with rectifiers and optical coatings, as well as devices that turn light into electrical energy, primarily need analysis of their optical properties to function effectively in technological implementations. External electromagnetic radiation causes materials to display specific optical reactions that both indicate their practical applications and reveal their structural information based on different energy levels. Scientists evaluate optical spectra to examine electronic band structures and bonding nature and internal configurations through both occupied and unoccupied states.[74]

$$\varepsilon(\omega) = \varepsilon_1(\omega) + i\varepsilon_2(\omega) \tag{22}$$

The real part, $\varepsilon_1(\omega)$, can be expressed using eqn (20):[61]

$$\varepsilon_1(\omega) = 1 + \frac{2}{\pi} P \int_0^{\infty} \frac{\varepsilon_2\left(\omega'\right)\omega'}{\omega'^2 - \omega^2} \mathrm{d}\omega \tag{23}$$

where *P* is the integral prime value.

The expression for the imaginary part of the dielectric function, $\varepsilon_2(\omega)$, formulated in terms of the momentum operator, is presented as follows (24):[75]

$$\varepsilon_2(\omega) = \frac{Ve^2}{2\pi\hbar m^2\omega^2} \times \int d^3k \sum |\varphi_c|p|\varphi_v|^2\ \delta(E_c - E_v - \hbar\omega) \tag{24}$$

The unit cell volume is represented by the symbol *V* in this equation, and the wave functions for the valence and conduction bands are identified by the symbols φ_v and φ_c respectively. The energy of the conduction band is represented by E_c, the energy of the valence band by E_v, the momentum operator by *p*, the reduced Planck's constant by $\hbar$, and the Dirac delta function by δ.

Using $\varepsilon_1(\omega)$ and $\varepsilon_2(\omega)$, other optical properties such as the absorption coefficient $\alpha(\omega)$, optical conductivity $\sigma(\omega)$, energy loss function $L(\omega)$, reflectivity $R(\omega)$, and refractive index $N(\omega)$ can be calculated using the following expressions (25)–(29):

$$\alpha(\omega) = \sqrt{2}\omega\left[\sqrt{\varepsilon_1{}^2(\omega) + \varepsilon_2{}^2(\omega)} - \varepsilon_1(\omega)\right]^{1/2} \tag{25}$$

$$\sigma(\omega) = \frac{\omega}{4\pi}\varepsilon_2(\omega) \tag{26}$$

$$L(\omega) = \frac{\varepsilon_2(\omega)}{\varepsilon_1{}^2(\omega) + \varepsilon_2{}^2(\omega)} \tag{27}$$

$$R(\omega) = \frac{[\varepsilon_1(\omega) + i\varepsilon_2(\omega)]^{1/2} - 1}{[\varepsilon_1(\omega) + i\varepsilon_2(\omega)]^{1/2} + 1} \tag{28}$$

$$N(\omega) = \left[\frac{\varepsilon_1(\omega)}{2} + \frac{\sqrt{\varepsilon_1{}^2(\omega) + \varepsilon_2{}^2(\omega)}}{2}\right]^{1/2} \tag{29}$$

The optical parameters associated with perovskite materials demonstrate dependence on energy through their absorption coefficient $\alpha(\omega)$, optical conductivity $\sigma(\omega)$, and dielectric function $\varepsilon(\omega)$, as well as energy loss function $L(\omega)$, reflectivity $R(\omega)$, and refractive index $N(\omega)$. This section explains the method for calculating optical properties to examine the $TlPbI_3$ photon response. The Fig. 3a–f represent the parameter spectra from 0 to 18 eV energy levels in the study.

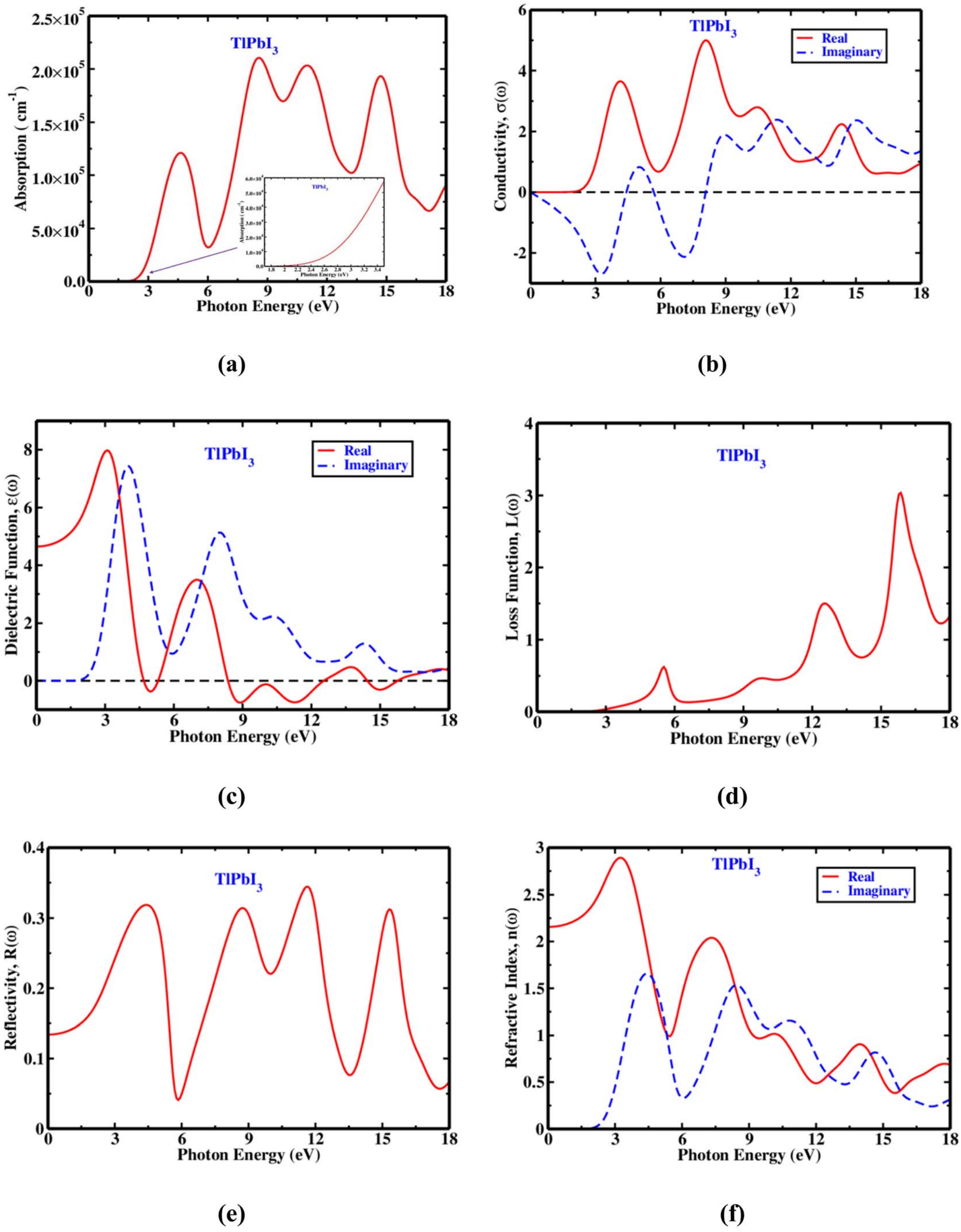

(a) (b) (c) (d) (e) (f)

Fig. 3 The (a) absorption coefficient, (b) conductivity, (c) dielectric function, (d) electron loss function, (e) reflectivity, and (f) refractive index of TlPbI$_3$ perovskites with photon energy.

The absorption coefficient functions as a basic parameter for measuring the optical energy absorption rate through material length[76–80]. Intake of optical energy occurs through a matching interaction between atomic state differences and photon frequencies, allowing photon energy absorption. The dependency of the absorption coefficient on photon frequency allows materials to choose photons based on their energy levels within particular ranges. During this process, electrons in the upper valence band transition to vacant states in the lower conduction band. A semiconductor's operating band determines its range of light absorption onset. When photon energy reaches beyond a particular level, it will energize valence electrons to create absorption events. The optical absorption coefficient $\alpha(\omega)$ of TlPbI$_3$ material appears in Fig. 3(a). The absorption of light begins at 2 eV when analyzing TlPbI$_3$, which leads to a wide optical band gap. The photon absorption behavior of TlPbI$_3$ shows robust properties for high-energy radiation, which makes this material suitable for use in optoelectronic systems.

The density of induced current depends on the electric field strength at a specific frequency according to the optical conductivity theory. The concept of electrical transport in optical conductivity examines high-energy photon interactions through the induced electron conduction derived from the complex dielectric function. Fig. 3(b) depicts the real and imaginary spectra of optical conductivity for $TlPbI_3$. The imaginary conductivity begins at zero energy before the appearance of real conductivity at 2 electron volts. The optical conductivity of $TlPbI_3$ shows its highest value at a photon energy level of 4.10 eV when under illumination. The recorded data demonstrates $TlPbI_3$ has desirable photoconductive features that make it suitable for optoelectronic applications.

The real and imaginary parts of $TlPbI_3$ dielectric function appear in Fig. 3(c). The Kramers–Kronig relations help radiofrequency techniques derive the energy-frequency relationships between real and imaginary parts of the complex dielectric function, as demonstrated in ref. 81. The momentum matrix elements determine the computation of these functions through evaluations of electronic transitions within all permitted states between occupied and unoccupied states.[82,83] The material's electrical polarization response appears in the real part, while dielectric loss from energy absorption appears in the imaginary part.[84,85] The static dielectric constant evaluation for $TlPbI_3$ reveals a value of 4.6 at zero energy level through Fig. 3(c). The ability of a material to protect against electric fields influences the recombination speed of charge carriers in optoelectronic devices, and this strength appears as the value of the static dielectric constant. Higher dielectric constants tend to slow down recombination processes to produce better device functionality. When the photon energy reaches UV levels, the real part of the dielectric function decreases until it reaches negative values. The material displays metallic reflective characteristics in the energy span between 8 and 13 eV when its value transitions to negative values. The observed multiple peaks in the visible and UV range support this behavior. As photon energy rises in Fig. 3(c), the real part shows distinct peak patterns representing energy losses which occur when electrons transition from valence band peaks to conduction band valleys. The optical behavior of the material becomes more pronounced through its prominent peak at 4.00 eV in the imaginary part. The semiconducting properties of $TlPbI_3$ match those of metal materials according to its band structure and density of states analysis.[84]

The evaluation of photon energy dissipation from interactions between materials and electromagnetic waves depends on the energy loss function $L(\omega)$ whose graph shows energy variation as presented in Fig. 3(d). $L(\omega)$ reveals the loss of energy that occurs inside materials. The energy loss function $L(\omega)$ shows minimal change before photon energies begin to elevate the values. The energy loss curve advances towards the X-axis until it meets the band gap energy of $TlPbI_3$ that measures about 2 eV. After the energy loss function reaches the band gap level of 3 eV, it achieves its peak at 16 eV.

The plasmon energy emerges as a specific trait of the substance that creates collective oscillations of charge carriers known as plasma oscillations. Strong coupling occurs between the material and the electromagnetic field when both the absorption coefficient and reflectivity decrease at this specific energy level. Laboratory experiment results indicate that Fig. 3(e) shows the reflectivity spectrum $R(\omega)$ for $TlPbI_3$ material. The reflectance peaks emerge at 4.00 eV, while 11.5 eV stands as the second peak, and both peaks have reflectance values of 0.32 and 0.34. The material displays effective light absorption due to its low reflectance values according to these data.[86]

A graph in Fig. 3(f) shows the complex parameter of refractive index. It is also a frequency or energy-dependent function. It can also be expressed as:[81]

$$N(\omega) = n(\omega) + ik(\omega) \tag{30}$$

The electromagnetic energy attenuation rate within materials is measured through $k(\omega)$, which represents the imaginary component of complex $N(\omega)$. The real part $n(\omega)$ controls the electromagnetic wave's phase velocity and establishes the amount of light refraction when the substance is traversed.[87] The visible spectrum shows that the real part of the refractive index achieves its maximum strength because photon energies remain low during this time. The refractive index value for $TlPbI_3$ reaches 2.9 at the photon energy of 2.10 eV. Due to its favorable light spectrum response, $TlPbI_3$ demonstrates great promise to be used as an optoelectronic device material.[88]

3.5 The performance of output devices

3.5.1 Band diagram. Fig. 4(a) illustrates the proposed solar cell configuration, featuring a multilayer structure composed of FTO/ETL (CdS, In_2S_3, or SnS_2)/$TlPbI_3$/Cu. The optical bandgap and structural thickness of the constituent materials serve as critical determinants influencing the overall efficiency and operational behavior of perovskite solar cells.[89] In Fig. 4(b–d), the band alignment diagram illustrates the energy levels of the $TlPbI_3$ absorber, CdS/In_2S_3/SnS_2 electron transport layer (ETL), and FTO transparent conductive oxide in a solar cell structure (Tables 3 and 4).

In PSC architecture, the absorber layer is interfaced with ETL, which often possesses differing band gaps and electron affinities. These disparities can result in unfavorable band alignments at the interfaces, such as spike-type offsets that hinder carrier extraction or cliff-type offsets that enhance interfacial recombination. Both scenarios compromise carrier dynamics and significantly limit device performance.[98] In the FTO/CdS/$TlPbI_3$ configuration, Fig. 4(b), the conduction band offset (CBO) between $TlPbI_3$ and CdS is nearly flat, minimizing band discontinuity and enabling efficient electron transport with negligible recombination losses. The large valence band offset (VBO) acts as an effective hole-blocking barrier, enhancing charge separation. The $TlPbI_3$ absorber (1.26 eV bandgap) ensures strong light absorption, CdS (2.40 eV bandgap) facilitates electron extraction, and the FTO layer (3.60 eV bandgap) offers excellent transparency and conductivity. For the FTO/In_2S_3/$TlPbI_3$ structure, Fig. 4(c), a large negative CBO forms a "cliff" at the interface, impeding electron transport and increasing recombination, though the significant VBO effectively prevents hole leakage. Despite this limitation, proper Fermi level alignment maintains charge separation. In contrast, the FTO/SnS_2/$TlPbI_3$ system, Fig. 4(d), exhibits

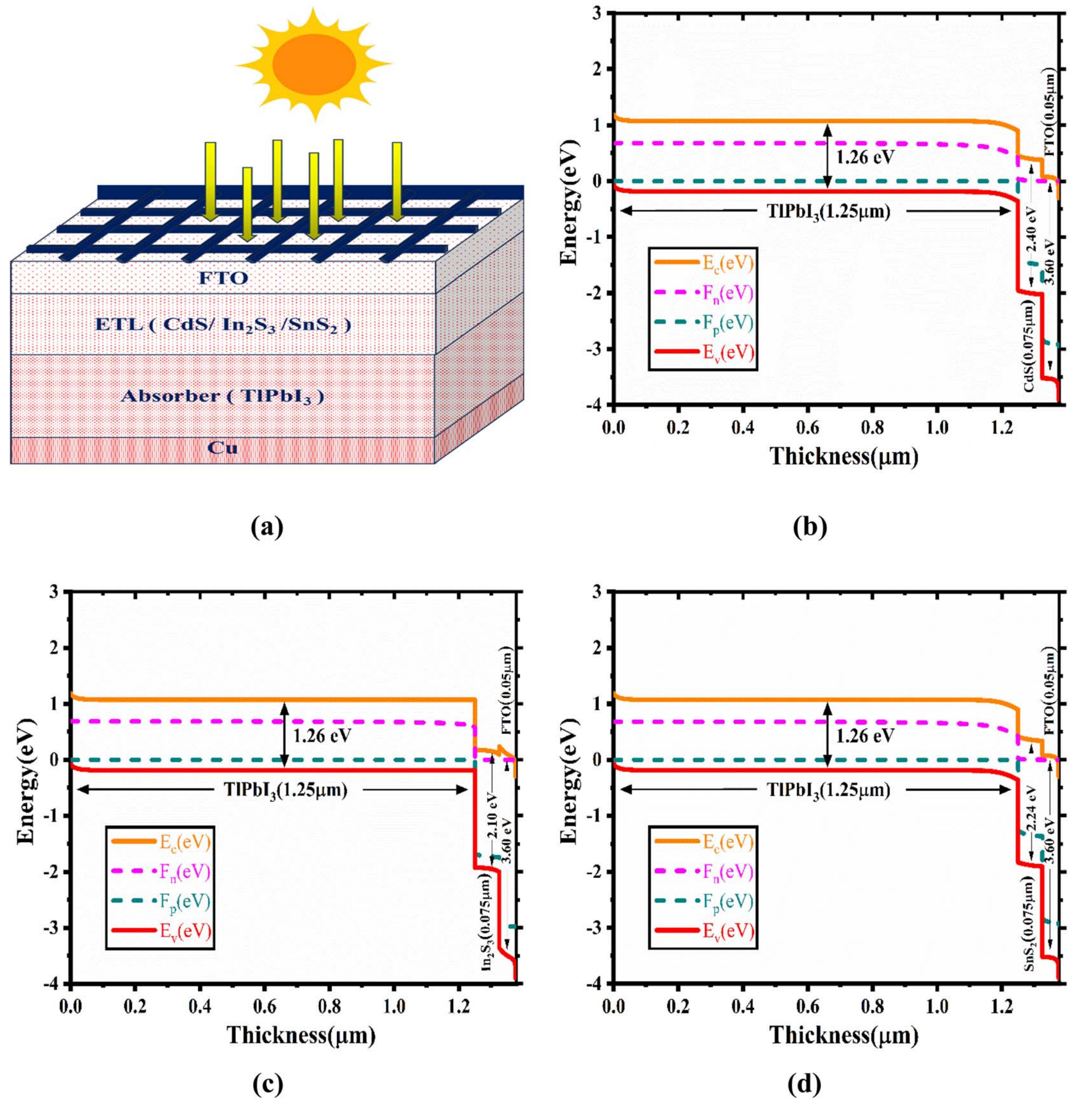

Fig. 4 Diagram depicting the band diagram of (a) $FTO/CdS/TlPbI_3$, (b) $FTO/In_2S_3/TlPbI_3$, and (c) $FTO/SnS_2/TlPbI_3$ structure.

a moderately negative CBO and strong VBO, balancing charge transport and recombination suppression. SnS_2 (2.24 eV bandgap) provides superior transparency and electron mobility, emerging as a promising ETL alternative. Overall, all configurations display favorable band bending and charge transfer characteristics, with CdS and SnS_2 offering optimal alignment for efficient and stable device performance.

3.5.2 Effect of changes in the thickness of the absorber layer. The thickness of the perovskite absorber critically affects solar cell efficiency. Optimal thickness enhances light

Table 3 Outlines the input parameters for the $TlPbI_3$-based solar cell's FTO, ETL, and absorber layer

Parameters	Terms	$TlPbI_3$	CdS[8,90,91]	In_2S_3 (ref. 8, 92 and 93)	SnS_2 (ref. 94–96)	FTO[57,60,97]
t (nm)	Thickness	1250	75	75	75	50
E_g (eV)	Band gap	1.26	2.4	2.1	2.24	3.6
χ (eV)	Electron affinity	3.75	4.2	4.65	4.24	4.5
ε_r	Dielectric (relative) permittivity	4.66	10	13.5	10	10
N_C (1 cm^{-3})	CB effective density of states	6.701×10^{18}	2.2×10^{18}	1.8×10^{19}	2.2×10^{18}	2×10^{18}
N_V (1 cm^{-3})	VB effective density of states	1.424×10^{19}	1.8×10^{19}	4×10^{13}	1.8×10^{19}	1.8×10^{19}
μ_h ($cm^2 V^{-1} s^{-1}$)	Hole mobility	75.90	25	210	50	20
μ_n ($cm^2 V^{-1} s^{-1}$)	Electron mobility	91.90	100	400	50	100
N_D (1 cm^{-3})	Hallow uniform donor density	0	1×10^{16}	1×10^{16}	1×10^{16}	1×10^{17}
N_A (1 cm^{-3})	Shallow uniform acceptor density	1×10^{16}	0	0	0	0
N_t (1 cm^{-3})	Defect density	1×10^{14}	1×10^{14}	1×10^{14}	1×10^{14}	1×10^{14}

Table 4 Information concerning the $TlPbI_3$-based solar cell's interface parameters

Interface	Parameters Energy with respect to reference E_r (eV)	Working temperature (K)	Capture cross-section holes σ_h (cm^2)	Capture cross-section electrons σ_e (cm^2)	Total defect density	Energetic distribution	Type of defect
$TlPbI_3/CdS$	0.6	300	1×10^{-19}	1×10^{-19}	10^{10}	Single	Neutral
$TlPbI_3/In_2S_3$	0.6	300	1×10^{-19}	1×10^{-19}	10^{11}	Single	Neutral
$TlPbI_3/SnS_2$	0.6	300	1×10^{-19}	1×10^{-19}	10^{10}	Single	Neutral

absorption and minimizes recombination losses, improving carrier transport and device performance.[99] An overly thin layer reduces photon capture, while an excessively thick one increases recombination and resistance, hindering charge collection and lowering overall efficiency.[100]

Fig. 5(a) illustrates the variation of V_{OC} as a function of absorber layer thickness (0.25–2.0 μm) for $TlPbI_3$-based perovskite solar cells employing three different ETLs: CdS (Device 1), In_2S_3 (Device 2), and SnS_2 (Device 3). Across all absorber thicknesses, Device 1 demonstrates the highest V_{OC} values, ranging from 0.786 V at 0.25 μm to a nearly constant 0.799 V for absorber thicknesses ≥ 2.0 μm. This indicates stable performance with minimal dependence on absorber thickness. Device 3 also exhibits comparably high V_{OC} values, starting from 0.781 V at 0.25 μm and stabilizing at 0.794 V beyond 1.0 μm. In contrast, Device 2 consistently shows the lowest V_{OC}, with values

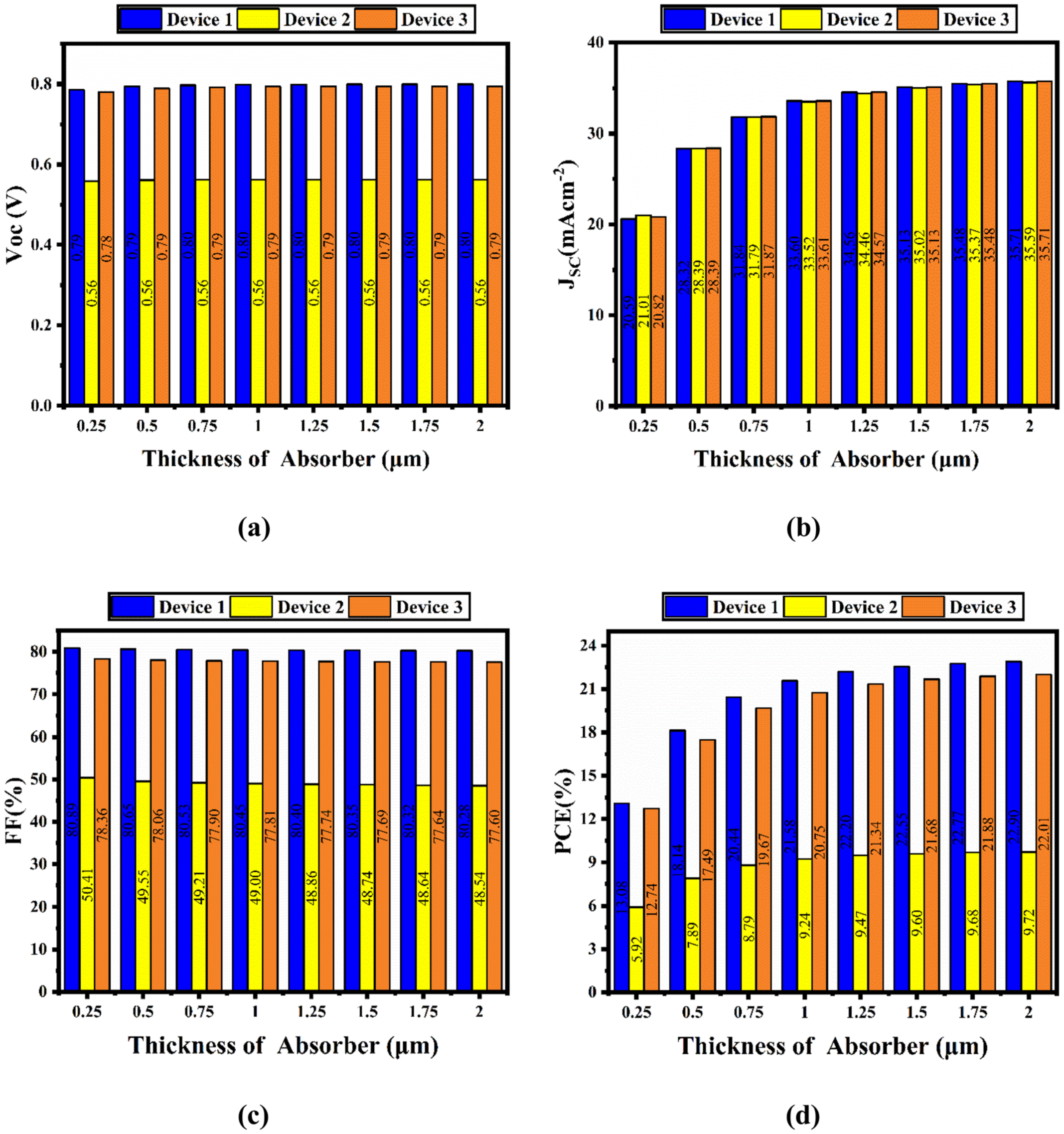

(a) (b)

(c) (d)

Fig. 5 Effects of absorber layer thickness on PV characteristics: (a) $V_{OC,}$ (b) $J_{SC,}$ (c) FF, and (d) PCE.

confined to the range of 0.559–0.563 V across all thicknesses. Overall, CdS delivers the best performance in terms of V_{OC} stability and magnitude, while SnS_2 emerges as a promising alternative to replace CdS due to its comparable performance. In contrast, In_2S_3 exhibits clear limitations as an ETL for $TlPbI_3$-based perovskite solar cells.

Fig. 5(b) presents the variation of J_{SC} as a function of absorber layer thickness (0.25–2.0 μm) for $TlPbI_3$-based perovskite solar cells using three different ETLs. All three devices exhibit a similar increasing trend in J_{SC} with absorber thickness, which is expected since thicker absorbers enhance light absorption and photo generation until saturation is reached. At 0.25 μm, Device 1 produces a J_{SC} of 20.59 mA cm^{-2}, while Device 2 and Device 3 achieve slightly higher values of 21.01 and 20.82 mA cm^{-2}, respectively. With increasing absorber thickness, J_{SC} steadily improves, reaching 28.32–28.39 mA cm^{-2} at 0.50 μm and 31.79–31.87 mA cm^{-2} at 0.75 μm for all devices. At absorber thicknesses of 1.0 μm and beyond, J_{SC} shows diminishing improvements, indicating the onset of optical absorption saturation. Specifically, J_{SC} stabilizes at about 35.5–35.7 mA cm^{-2} for thicknesses above 1.75 μm across all devices. Overall, the results confirm that absorber thickness plays a critical role in maximizing J_{SC} up to 1.25 μm, beyond which current density saturates. The near-identical performance of CdS, In_2S_3, and SnS_2 with respect to J_{SC} implies that all three ETLs are capable of facilitating efficient electron extraction once sufficient photo generation is achieved.

Fig. 5(c) illustrates the dependence of FF on absorber thickness (0.25–2.0 μm) for $TlPbI_3$-based perovskite solar cells using all three different ETLs. Across the entire range of absorber thicknesses, Device 1 exhibits the highest FF, remaining remarkably stable around 80.3–80.9%. Device 3 also shows consistently high FF values, though slightly lower than CdS, with values ranging from 77.6–78.4%. By contrast, Device 2 performs significantly worse, with FF values between 48.5–50.4%, nearly 30% lower than the CdS-based device. Overall, CdS remains the most effective ETL in terms of FF optimization, while SnS_2 demonstrates competitive performance as a potential non-toxic alternative. However, In_2S_3 shows severe limitations as an ETL due to its inability to sustain a high fill factor, regardless of absorber thickness.

Fig. 5(d) illustrates the variation in PCE (η) of $TlPbI_3$-based perovskite solar cells as a function of absorber thickness (0.25–2.0 μm) when employing three different ETLs. At a thin absorber thickness of 0.25 μm, the CdS and SnS_2-based devices exhibit relatively high efficiencies of 13.08% and 12.74%, respectively, whereas the In_2S_3-based device shows a much lower efficiency of 5.92%. As the absorber thickness increases, the PCE improves significantly for all devices due to enhanced light absorption and photocurrent generation. At 0.50 μm thickness, CdS reaches 18.14%, SnS_2 achieves 17.49%, and In_2S_3 only reaches 7.89%. Beyond 0.75 μm, the efficiency growth begins to saturate, indicating that most of the incident light is already absorbed. At 1.0 μm thickness, CdS, SnS_2, and In_2S_3 devices achieve PCE values of 21.58%, 20.75%, and 9.24%, respectively. A further increase to 2.0 μm results in near-saturation efficiencies of 22.90% (CdS), 22.01% (SnS_2), and 9.72% (In_2S_3). Overall, Device 1 demonstrates the highest efficiency across all absorber thicknesses, maintaining a consistent advantage over SnS_2 and a clear superiority over In_2S_3. Device 3 follows closely, with only ~0.5–1% lower efficiency compared to CdS, making it a competitive non-toxic alternative. Device 2, however, consistently underperforms due to its poor V_{OC} and FF, achieving less than half the efficiency of CdS and SnS_2-based devices. This analysis highlights that CdS remains the most optimized ETL for $TlPbI_3$-based perovskite solar cells, while SnS_2 emerges as a strong replacement candidate. In_2S_3, despite being non-toxic, exhibits severe limitations in performance and requires further optimization to be viable.

3.5.3 Effect of changes in the doping concentration of the absorber layer. Fig. 6(a) shows the variation of V_{OC} with respect to doping density (10^{12}–10^{18} cm^{-3}) for $TlPbI_3$-based perovskite solar cells employing CdS (Device 1), In_2S_3 (Device 2), and SnS_2 (Device 3) as ETLs. For Device 1 and Device 3, V_{OC} values remain relatively stable around 0.79–0.80 V at low doping densities (10^{12}–10^{15} cm^{-3}). As doping density increases beyond 10^{15} cm^{-3}, a gradual improvement is observed, with V_{OC} reaching 0.838 V for CdS and 0.828 V for SnS_2 at the highest doping level (10^{18} cm^{-3}). This trend indicates that higher doping concentrations effectively reduce recombination losses and enhance built-in potential, thereby improving the V_{OC}. In contrast, Device 2 exhibits significantly lower V_{OC} values across the entire doping range, starting at 0.560 V (10^{12} cm^{-3}) and only marginally increasing to 0.578 V at 10^{18} cm^{-3}. The flat response with minimal improvement suggests severe interfacial recombination and poor band alignment between In_2S_3 and $TlPbI_3$, limiting the achievable V_{OC} regardless of doping density. Comparatively, CdS and SnS_2 show nearly identical performance trends, with CdS consistently maintaining a slight advantage. In_2S_3, however, underperforms substantially, with V_{OC} values nearly 0.25 V lower than CdS and SnS_2, confirming its inefficiency as an ETL for $TlPbI_3$-based solar cells.

Fig. 6(b) illustrates the effect of absorber doping concentration (10^{12}–10^{18} cm^{-3}) on the J_{SC} of $TlPbI_3$-based solar cells with CdS (Device 1), In_2S_3 (Device 2), and SnS_2 (Device 3) as ETLs. At low to moderate doping concentrations (10^{12}–10^{15} cm^{-3}), all devices maintain nearly constant J_{SC} values, with Device 1 and Device 3 showing ~34.9 mA cm^{-2} and Device 2 slightly lower at ~34.6–34.8 mA cm^{-2}. This indicates efficient carrier generation and transport with minimal recombination losses in the absorber layer within this doping range. As the doping concentration increases beyond 10^{16} cm^{-3}, J_{SC} begins to decline significantly for all devices. At 10^{17} cm^{-3}, J_{SC} reduces to 32.3 mA cm^{-2} for all devices, and further decreases to 28.3–28.6 mA cm^{-2} at 10^{18} cm^{-3}. The reduction in J_{SC} at high doping levels can be attributed to enhanced Auger recombination and reduced carrier diffusion lengths, which limit charge extraction. Comparatively, all three ETLs exhibit similar J_{SC} behavior, with only minor variations across the doping range. CdS and SnS_2 show nearly identical performance, while In_2S_3 remains marginally lower at lower doping levels but converges at higher doping concentrations.

Fig. 6(c) shows the variation of the FF of solar cell devices employing CdS, In_2S_3, and SnS_2 as ETLs with absorber doping

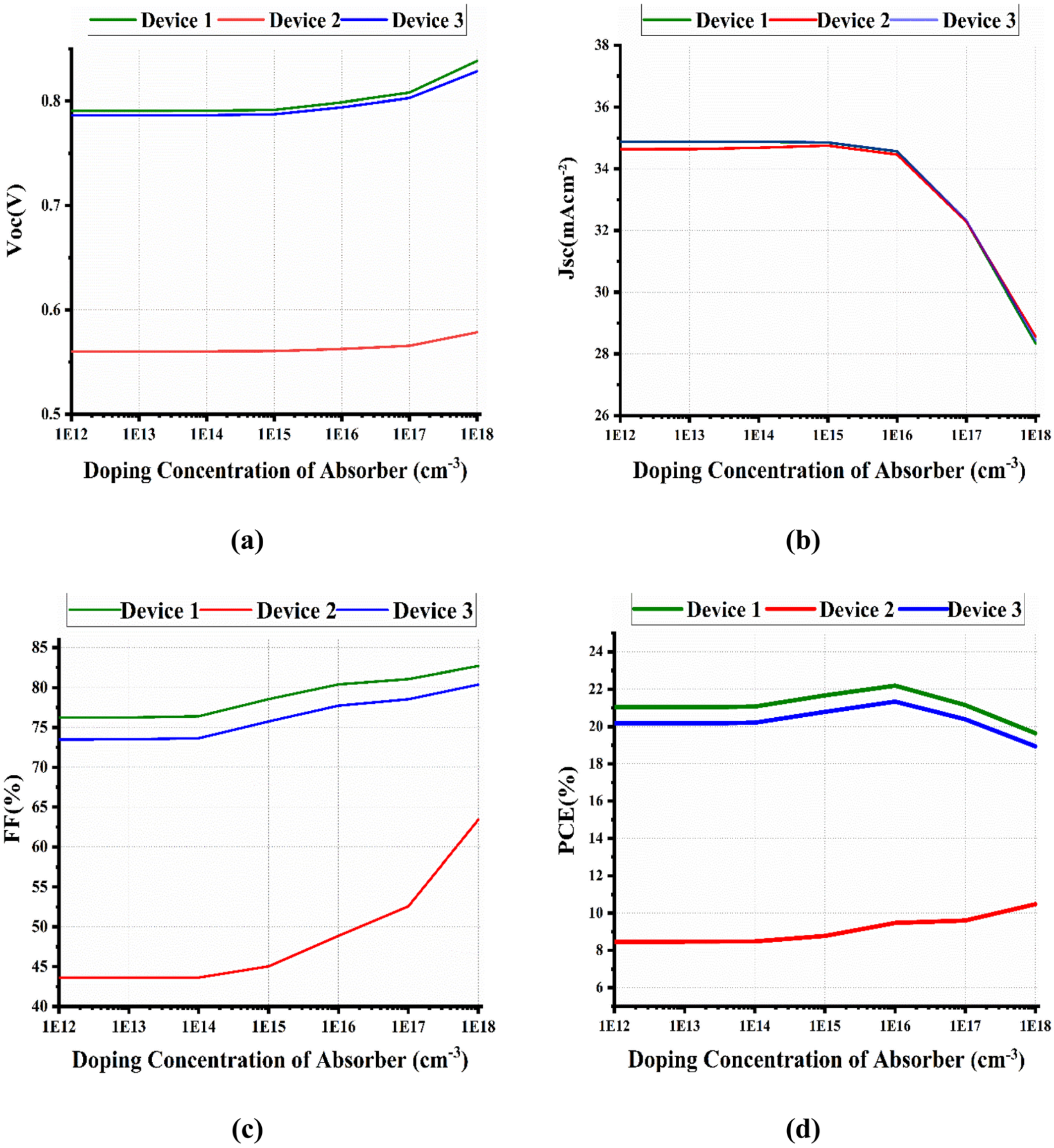

Fig. 6 Effects of absorber layer doping density on PV characteristics: (a) V_{OC}, (b) J_{SC}, (c) FF, and (d) PCE.

concentrations ranging from 10^{12} to 10^{18} cm^{-3}. For the CdS-based device, FF starts at 76.2% between 10^{12} and 10^{13} cm^{-3} and remains nearly unchanged up to 10^{14} cm^{-3}, after which it gradually increases to 78.5% at 10^{15} cm^{-3}, 80.4% at 10^{16} cm^{-3}, and reaches a peak of 82.7% at 10^{18} cm^{-3}, indicating consistently high FF values with moderate improvement at higher doping levels. In contrast, the In_2S_3-based device exhibits the lowest FF, beginning at 43.6% up to 10^{14} cm^{-3} and then rising progressively to 45.0% at 10^{15} cm^{-3}, 48.9% at 10^{16} cm^{-3}, 52.6% at 10^{17} cm^{-3}, and 63.4% at 10^{18} cm^{-3}; although it shows significant improvement with higher doping, it still underperforms compared to CdS and SnS_2 devices. Meanwhile, the SnS_2-based device records an FF of 73.5% at low doping (10^{12} cm^{-3}), which remains stable up to 10^{14} cm^{-3} before gradually increasing to 75.8% at 10^{15} cm^{-3}, 77.7% at 10^{16} cm^{-3}, 78.5% at 10^{17} cm^{-3}, and 80.4% at 10^{18} cm^{-3}, thereby demonstrating performance comparable to CdS, particularly at higher doping levels.

Fig. 6(d) illustrates the dependence of PCE on absorber doping concentration for perovskite solar cells using CdS, In_2S_3, and SnS_2 as ETLs, with doping varied from 10^{12} to 10^{18} cm^{-3}. The CdS-based device consistently achieves the highest efficiency, starting at 21.0% at low doping (10^{12}–10^{13} cm^{-3}), peaking at 22.2% at 10^{16} cm^{-3}, and then declining to 21.1% at 10^{17} cm^{-3} and 19.6% at 10^{18} cm^{-3}, indicating an optimum performance around 10^{16} cm^{-3}. In contrast, the In_2S_3-based device shows the lowest efficiency throughout, beginning at 8.47% at 10^{12} cm^{-3} and gradually increasing to 9.47% at 10^{16} cm^{-3} before reaching a maximum of 10.5% at 10^{18} cm^{-3}; although it improves steadily with doping, its overall performance remains significantly lower. The SnS_2-based device starts at 20.2% efficiency at low doping, close to CdS but slightly lower, increases to a maximum of 21.3% at 10^{16} cm^{-3}, and then

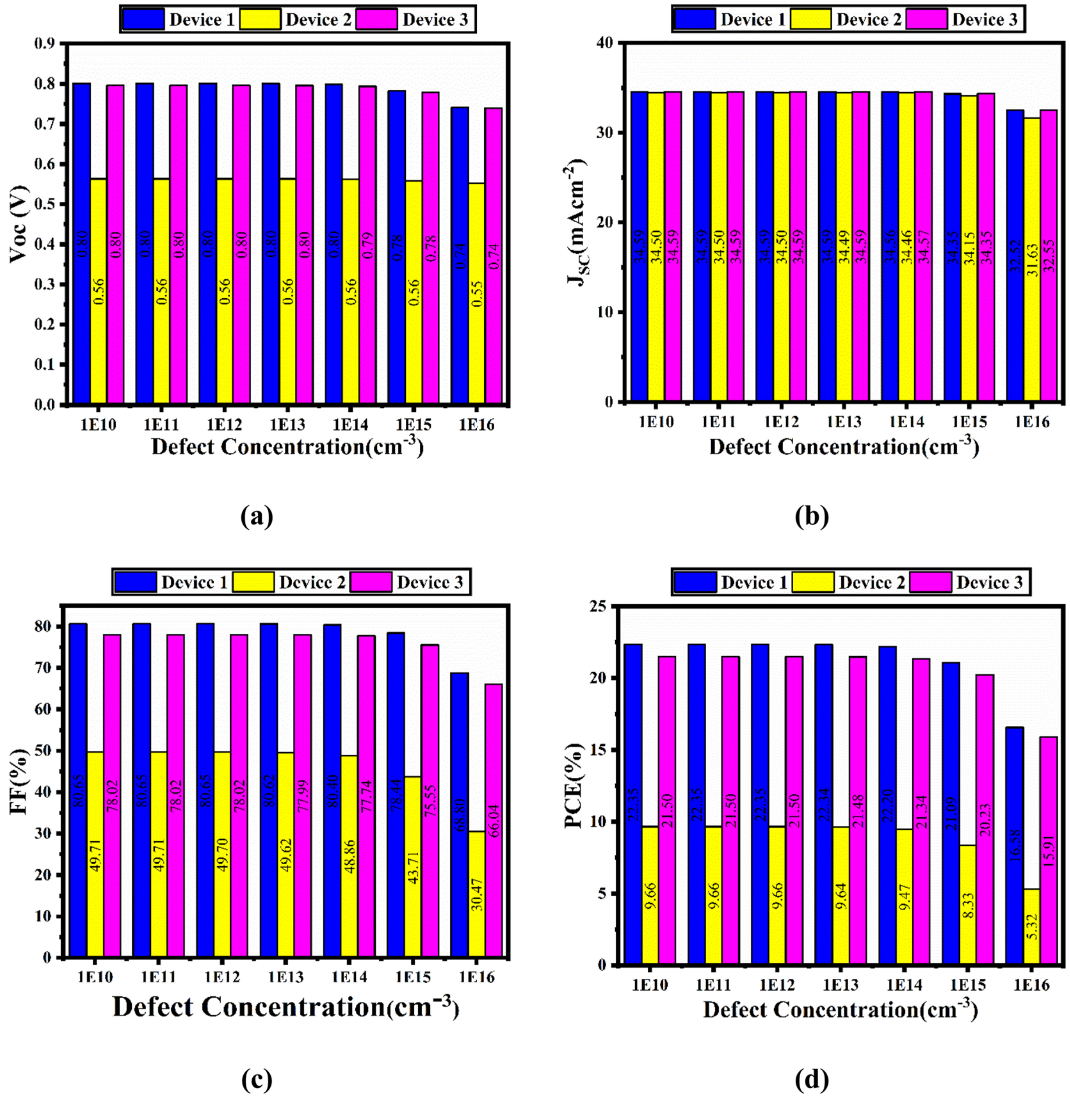

(a) (b)

(c) (d)

Fig. 7 Effects of absorber layer defect density on PV characteristics: (a) V_{OC}, (b) J_{SC}, (c) FF, and (d) PCE.

decreases to 20.4% at 10^{17} cm^{-3} and 18.9% at 10^{18} cm^{-3}, showing a similar trend to CdS where excessive doping reduces efficiency. This highlights the crucial importance of controlling and minimizing defect concentrations to maintain superior device performance and ensure long-term operational efficiency.[101]

3.5.4 Effect of changes in the defect concentration of the absorber layer. Fig. 7(a) illustrates the variation of the V_{OC} as a function of bulk defect concentration (10^{10}–10^{16} cm^{-3}) for three perovskite solar cell configurations employing different ETLs: CdS (Device 1), In_2S_3 (Device 2), and SnS_2 (Device 3). Across all devices, V_{OC} exhibits a relatively stable response in the low-to-moderate defect regime (10^{10}–10^{13} cm^{-3}). For Device 1, V_{OC} remains nearly constant at 0.80 V up to 10^{13} cm^{-3}, followed by a slight reduction to 0.799 V at 10^{14} cm^{-3}, and a more pronounced drop to 0.741 V at the highest defect density of 10^{16} cm^{-3}. Similarly, Device 3 demonstrates high V_{OC} stability, maintaining 0.797 V up to 10^{13} cm^{-3}, gradually declining to 0.794 V at 10^{14} cm^{-3}, and reaching 0.740 V at 10^{16} cm^{-3}. In contrast, Device 2 consistently exhibits a lower V_{OC} across all defect densities, remaining nearly constant at 0.563 V from 10^{10}–10^{13} cm^{-3}, and decreasing slightly to 0.552 V at 10^{16} cm^{-3}. A comparative analysis indicates that CdS and SnS_2 provide superior electronic quality and defect tolerance compared to In_2S_3, with both maintaining V_{OC} values close to 0.80 V over several orders of magnitude of defect density.

Fig. 7(b) shows the dependence of the J_{SC} on bulk defect concentration (10^{10}–10^{16} cm^{-3}) for three perovskite solar cell architectures employing CdS (Device 1), In_2S_3 (Device 2), and SnS_2 (Device 3) as ETLs. In the low-to-moderate defect regime (10^{10}–10^{14} cm^{-3}), all three devices exhibit highly stable J_{SC} values, with minimal variation. Specifically, Device 1 and Device 3 consistently deliver 34.6 mAcm^{-2}, while Device 2 records a slightly lower but comparable value of 34.5 mAcm^{-2}. These results indicate that carrier extraction efficiency and photo generation remain largely unaffected by moderate increases in defect density for all ETL configurations. A noticeable reduction in J_{SC} is observed only at very high defect concentrations ($\geq 10^{15}$

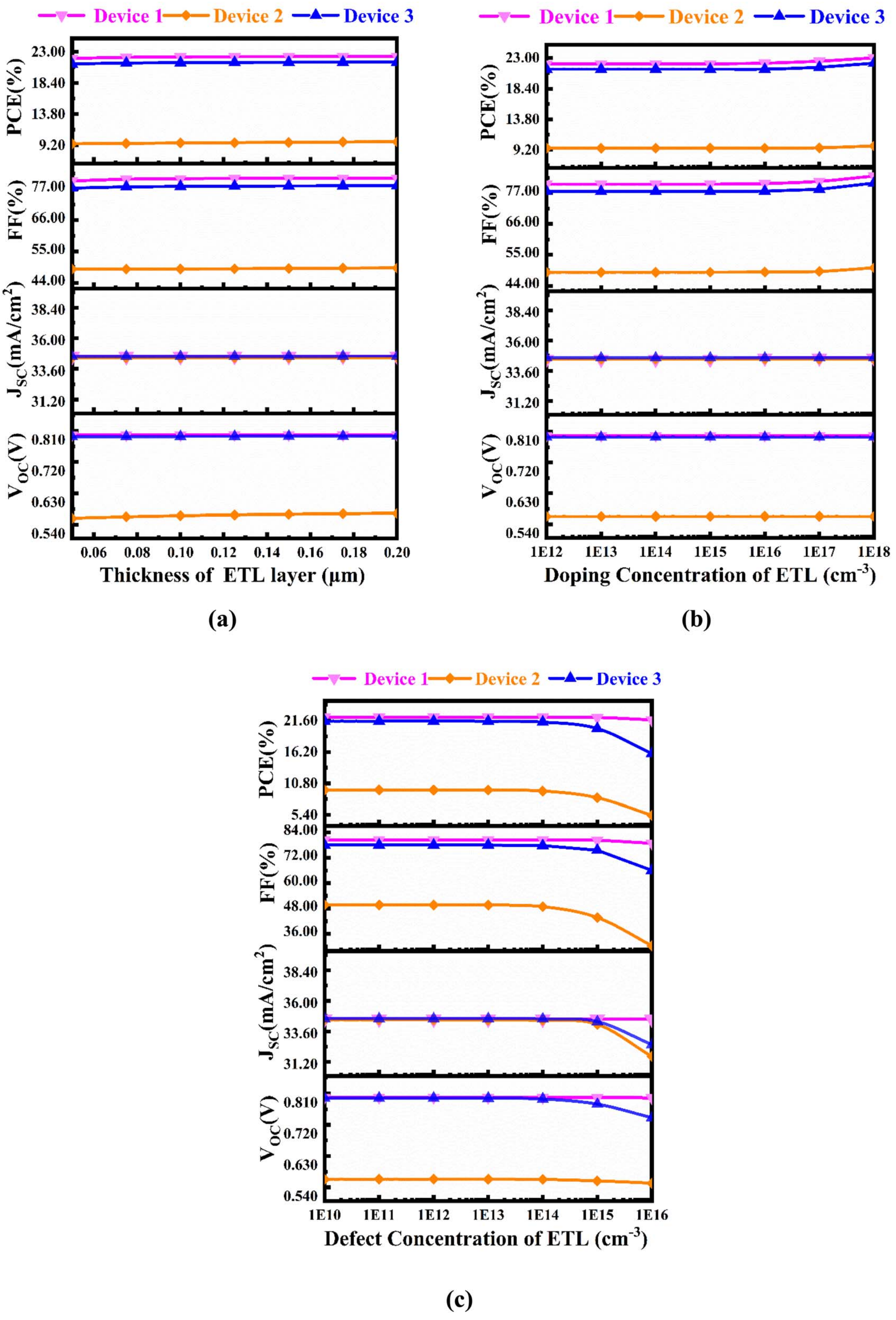

Fig. 8 Effects on PV performance parameters (V_{OC}, J_{SC}, FF, and PCE) for changing the ETL layers (a) thickness, (b) doping density, (c) defect density.

cm^{-3}). At 10^{15} cm^{-3}, J_{SC} decreases slightly to 34.15 mAcm^{-2} (CdS), 34.25 mAcm^{-2} (In_2S_3), and 34.35 mAcm^{-2} (SnS_2). The degradation becomes more significant at 10^{16} cm^{-3}, where Device 1 drops to 32.5 mAcm^{-2}, Device 2 to 31.6 mAcm^{-2}, and Device 3 to 32.6 mAcm^{-2}. The decline in J_{SC} at these extreme defect densities can be attributed to enhanced bulk recombination pathways, which suppress charge collection and reduce photocurrent output. Comparative analysis reveals that CdS and SnS_2 maintain slightly higher J_{SC} values compared to In_2S_3, both under low-defect and high-defect conditions. This suggests that CdS and SnS_2 facilitate more efficient electron transport and mitigate recombination losses more effectively than In_2S_3.

Fig. 7(c) presents the dependence of the FF on bulk defect concentration in the range of 10^{10}–10^{16} cm^{-3} for perovskite solar cells employing three different ETLs. At low defect densities (10^{10}–10^{13} cm^{-3}), Devices 1 and 3 exhibit consistently high FF values above 78%, with CdS maintaining 80.6% and SnS_2 sustaining 78.0%. In_2S_3, however, shows a significantly lower FF (49.7%) across this defect regime, indicating less efficient charge extraction and higher series or recombination losses compared to CdS and SnS_2. As defect concentration increases beyond 10^{14} cm^{-3}, all devices experience a gradual decline in FF. For Device 1, FF decreases from 80.4% at 10^{14} cm^{-3} to 78.4% at 10^{15} cm^{-3}, followed by a sharper drop to 68.8% at 10^{16} cm^{-3}. Device 3 follows a similar trend, falling from 77.7% at 10^{14} cm^{-3} to 75.6% at 10^{15} cm^{-3}, and further to 66.0% at 10^{16} cm^{-3}. In contrast, Device 2 shows a more dramatic degradation: FF falls from 48.9% at 10^{14} cm^{-3} to 43.7% at 10^{15} cm^{-3}, and finally collapses to just 30.5% at 10^{16} cm^{-3}. Overall, CdS emerges as the most robust ETL in terms of FF stability, followed closely by SnS_2, while In_2S_3 shows poor performance across all defect levels.

Fig. 7(d) illustrates the variation of PCE with defect concentration (10^{10}–10^{16} cm^{-3}) for perovskite solar cells using three different ETLs. At low to moderate defect densities (10^{10}–10^{13} cm^{-3}), both CdS and SnS_2 devices demonstrate high and stable PCEs, with Device 1 maintaining 22.3–22.4% and Device 3 achieving 21.5%. In contrast, Device 2 records a significantly lower efficiency of 9.6%, reflecting its weaker electronic compatibility and higher recombination losses compared to the other ETLs. As the defect density increases, all devices exhibit a decline in PCE due to enhanced non-radiative recombination within the perovskite bulk. For CdS-based devices, PCE decreases gradually from 22.2% at 10^{14} cm^{-3} to 21.1% at 10^{15} cm^{-3}, before dropping sharply to 16.6% at 10^{16} cm^{-3}. SnS_2 devices show a similar trend, decreasing from 21.3% at 10^{14} cm^{-3} to 20.2% at 10^{15} cm^{-3}, and reaching 15.9% at 10^{16} cm^{-3}. In_2S_3 devices experience the steepest efficiency degradation, falling from 9.5% at 10^{14} cm^{-3} to 8.3% at 10^{15} cm^{-3}, and collapsing to only 5.3% at 10^{16} cm^{-3}. In summary, CdS and SnS_2 provide robust efficiency outcomes under varying defect conditions, with CdS slightly superior in both stability and overall PCE.

3.5.5 Effect of changes in the thickness, doping, and defect of the ETL layer.

Fig. 8(a) presents the dependence of photovoltaic performance on the ETL thickness for $TlPbI_3$-based perovskite solar cells incorporating CdS (Device 1), In_2S_3 (Device 2), and SnS_2 (Device 3) as ETLs. The investigated ETL thickness range spans 0.05–0.20 μm, and the extracted parameters include V_{OC}, J_{SC}, FF, and PCE. The charge collection in $TlPbI_3$ devices is efficient even at relatively thin ETL layers, and the transport losses are negligible above 50 nm. Device 1 (CdS) consistently demonstrates superior performance, with V_{OC} values stabilized at 0.799 V, J_{SC} at 34.6 mAcm^{-2}, and FF gradually improving from 79.8% to 80.8% as the ETL thickness increases. These parameters yield a maximum PCE of 22.3%. Conversely, Device 2 demonstrates markedly inferior performance. Despite achieving a comparable J_{SC} (34.5 mAcm^{-2}), its V_{OC} is considerably lower (0.559–0.573 V), and the FF remains limited to 49%. These limitations reduce the maximum PCE to only 9.7%. Device 3 exhibits comparable characteristics to CdS, with V_{OC} values around 0.794–0.795 V, J_{SC} maintained at 34.6 mAcm^{-2}, and FF ranging between 77.3–78.1%. Consequently, the maximum PCE reaches 21.5%. Although slightly lower than that of CdS, SnS_2 proves to be a highly effective ETL, showing stable performance across the entire thickness range. In summary, CdS and SnS_2 emerge as highly suitable ETLs for $TlPbI_3$ perovskite solar cells, both delivering stable efficiencies above 21% that are largely independent of ETL thickness in the 0.05–0.20 μm range.

Fig. 8(b) illustrates the effect of ETL doping concentration (10^{12}–10^{18} cm^{-3}) on the photovoltaic performance parameters of $TlPbI_3$-based perovskite solar cells employing three different ETLs in three devices. Across all devices, the J_{SC} remains essentially constant at 34.5–34.6 mAcm^{-2}, indicating that carrier generation and collection are unaffected by ETL doping concentration within the studied range. Instead, variations in performance are predominantly governed by changes in FF and, consequently, PCE. For Device 1, V_{OC} remains stable at 0.799 V throughout the entire doping range, while FF gradually increases from 80.2% at 10^{12} cm^{-3} to 83.1% at 10^{18} cm^{-3}. This enhancement in FF leads to a corresponding improvement in PCE from 22.1% to 23.0%. In contrast, Device 2 remains the weakest performer across all doping concentrations. V_{OC} is significantly lower (0.563 V) and does not change with doping. While FF improves modestly from 48.8% at 10^{12} cm^{-3} to 50.4% at 10^{18} cm^{-3}, the maximum PCE achieved is only 9.8%. Device 3 shows a similar trend, with V_{OC} stable around 0.794 V and FF improving from 77.6% at 10^{12} cm^{-3} to 80.6% at 10^{18} cm^{-3}. As a result, the PCE increases from 21.3% to 22.2%. Although slightly lower than CdS, SnS_2 demonstrates robust and consistent performance, confirming its suitability as an alternative ETL. Overall, both CdS and SnS_2 devices benefit from increased doping, achieving stable PCE values above 22%, whereas In_2S_3 remains unsuitable despite slight improvements.

Fig. 8(c) depicts the influence of ETL defect concentration (10^{10}–10^{16} cm^{-3}) on the photovoltaic characteristics of $TlPbI_3$-based perovskite solar cells using three different ETLs. For Device 1, performance remains largely stable at lower defect densities ($\leq 10^{13}$ cm^{-3}), with V_{OC} maintained at 0.799 V, J_{SC} at 34.6 mAcm^{-2}, FF at 80.4%, and PCE 22.2%. However, as defect concentration increases to 10^{15}–10^{16} cm^{-3}, a gradual decline is observed. At 10^{16} cm^{-3}, FF drops to 78.8%, and PCE decreases slightly to 21.7%, although V_{OC} and J_{SC} are still relatively stable. In contrast, Device 2 consistently exhibits the lowest performance across all defect levels. At low defect density (10^{10} cm^{-3}), V_{OC} is limited to 0.563 V, J_{SC} to 34.5 mAcm^{-2}, FF 49.7%, and PCE 9.7%. With increasing defect concentration, the deterioration becomes significant: at 10^{15} cm^{-3}, FF falls to 43.7%, and

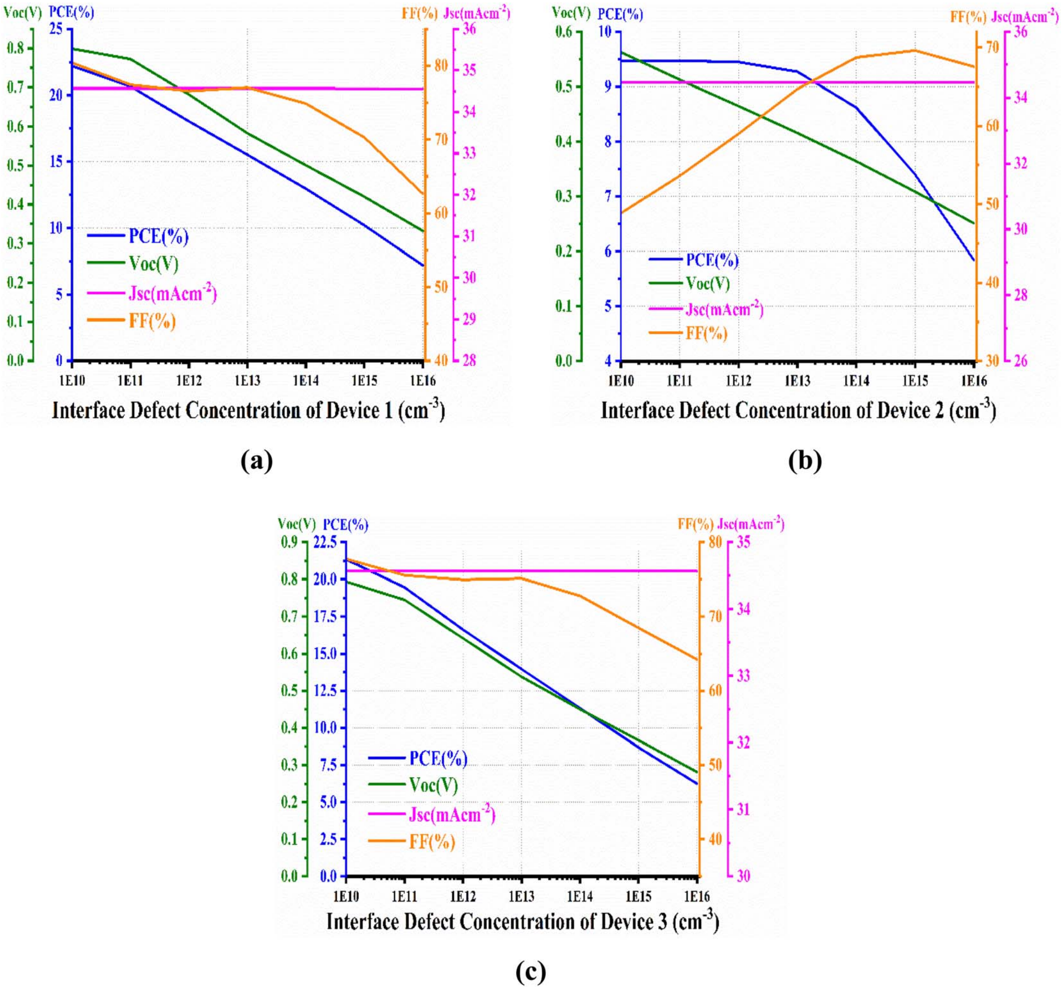

Fig. 9 Effects on PV performance parameters for changing the interface defect density between (a) absorber/device 1(CdS), (b) absorber/device 2(In_2S_3), and (c) absorber/device 3(SnS_2).

PCE drops to 8.3%; at 10^{16} cm^{-3}, V_{OC} decreases to 0.552 V, J_{SC} falls sharply to 31.6 $mAcm^{-2}$, FF reduces to 30.5%, and PCE plummets to only 5.3%. Device 3 follows a similar pattern. At low-to-moderate defect concentrations ($\leq 10^{13}$ cm^{-3}), performance is stable with V_{OC} 0.796 V, J_{SC} 34.6 $mAcm^{-2}$, FF 77.8–78.0%, and PCE 21.5%. As defects increase beyond 10^{14} cm^{-3}, V_{OC} drops to 0.779 V, J_{SC} reduces slightly to 34.4 $mAcm^{-2}$, and FF decreases to 75.6%, resulting in a PCE decline to 20.2%. At the highest defect density (10^{16} cm^{-3}), more severe degradation occurs, with V_{OC} reduced to 0.740 V, J_{SC} down to 32.6 $mAcm^{-2}$, FF falling to 66.0%, and PCE dropping to 15.9%. This demonstrates that SnS_2 is more sensitive to ETL defect density than CdS, particularly at very high defect concentrations. In summary, both CdS and SnS_2 are relatively defect-tolerant ETLs for $TlPbI_3$ solar cells, maintaining stable performance at low-to-moderate defect densities, with CdS showing the highest robustness. However, SnS_2 becomes increasingly sensitive at defect concentrations beyond 10^{14} cm^{-3}, while In_2S_3 exhibits poor tolerance to ETL defects across the entire range, resulting in severe efficiency degradation.

3.5.6 Effects of altering the interface defect density between absorber layer and ETL on the photovoltaic performance of the solar cell. Fig. 9(a) presents the device 1(CdS) dependence of photovoltaic performance parameters-PCE, V_{OC}, J_{SC}, and FF-on the interface defect concentration of the $TlPbI_3$-based perovskite solar cell. The defect density was varied over six orders of magnitude, from 10^{10} to 10^{16} cm^{-3}, to evaluate its impact on charge recombination dynamics and overall device performance. At the lowest defect density of 10^{10} cm^{-3}, the device exhibits its optimal performance with a PCE of 22.2%, corresponding to a V_{OC} of 0.799 V, J_{SC} of 34.6 $mAcm^{-2}$, and FF of 80.4%. As the defect concentration increases, however, significant degradation is observed in almost all photovoltaic parameters, with the exception of J_{SC}, which remains nearly constant throughout the entire range. Specifically, V_{OC} shows the steepest decline, decreasing from 0.799 V at 10^{10} cm^{-3} to 0.332 V at 10^{16} cm^{-3}. A similar trend is observed in PCE, which drops from 22.2% to 7.19%, underscoring the dominant role of interface defect states in suppressing device efficiency. The FF also decreases monotonically with rising defect density, from

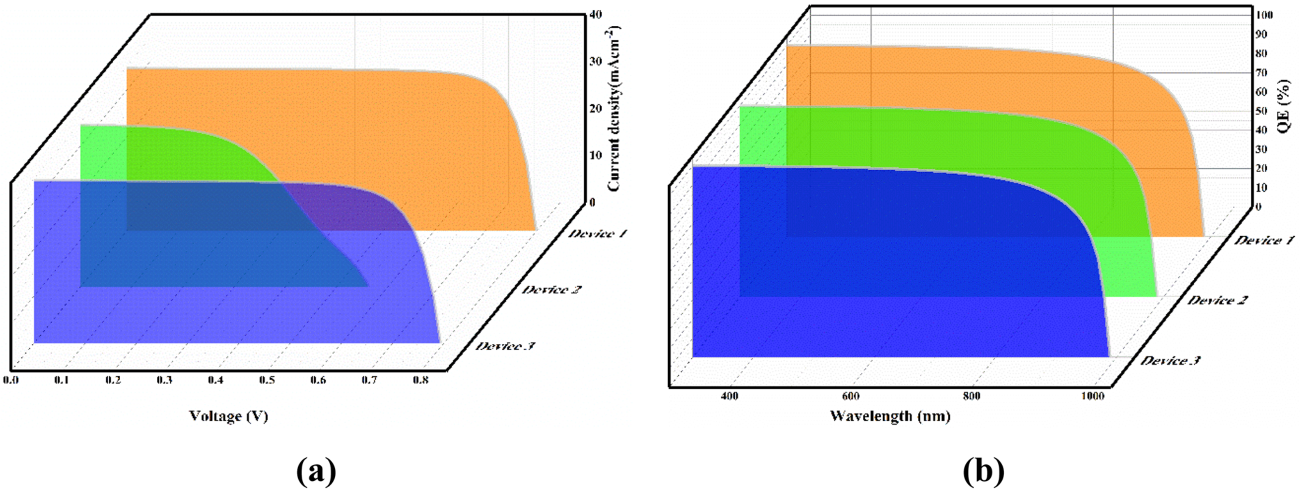

Fig. 10 (a) Current density–voltage (*J*–*V*) characteristic and (b) quantum efficiency (QE) spectrum of the CdS, In_2S_3, and SnS_2 ETL-based solar cell under standard illumination conditions.

80.4% to 62.6%. Interestingly, J_{SC} remains stable at 34.6 mAcm^{-2} across all defect densities. Overall, the results highlight that interface defect concentration is a critical factor governing the performance of $TlPbI_3$-based perovskite solar cells, primarily impacting V_{OC} and FF, which in turn determine the achievable PCE.

Fig. 9(b) illustrates the effect of interface defect concentration on the photovoltaic parameters-PCE, V_{OC}, J_{SC}, and FF-for Device 2 employing In_2S_3 as the ETL. The defect density was varied from 10^{10} to 10^{16} cm^{-3}. At the lowest defect density (10^{10}cm^{-3}), the device achieves a PCE of 9.47%, with a V_{OC} of 0.563 V, J_{SC} of 34.5 mAcm^{-2}, and a relatively low FF of 48.9%. Interestingly, as the defect concentration increases up to 10^{14} cm^{-3}, the FF exhibits a steady improvement, rising from 48.9% to 68.7%. In contrast, V_{OC} consistently decreases across the entire range, from 0.563 V to 0.251 V. The J_{SC} remains essentially constant at 34.5 mAcm^{-2}. The overall PCE follows a declining trend beyond 10^{12} cm^{-3}, dropping from 9.47% to 5.84% at the highest defect density. The initial stability in PCE despite the drop in V_{OC} is due to the compensatory effect of the increasing FF; however, once defect densities exceed 10^{14} cm^{-3}, the decline in V_{OC} dominates, leading to significant performance deterioration. These results emphasize that In_2S_3-based ETLs exhibit a different defect response compared to conventional ETLs: while moderate defect levels can improve FF, excessive defect concentrations critically reduce V_{OC} and overall PCE.

Fig. 9(c) illustrates the variation of photovoltaic parameters of the $TlPbI_3$-based perovskite solar cell employing SnS_2 as the ETL, with respect to the interface defect concentration at the ETL/perovskite junction, from 10^{10} cm^{-3} to 10^{16} cm^{-3}, and its impact on PCE, V_{OC}, J_{SC}, and FF was systematically analyzed. At a low defect concentration of 10^{10} cm^{-3}, the device achieved its optimal performance with a PCE of 21.3%, accompanied by a V_{OC} of 0.794 V, J_{SC} of 34.6 mAcm^{-2}, and FF of 77.7%. As the defect concentration increased, a pronounced decline in device performance was observed, primarily driven by reductions in both V_{OC} and PCE. For instance, when the defect density increased to 10^{13} cm^{-3}, the PCE decreased to 14.0%, with V_{OC} reduced to 0.538 V, while J_{SC} remained unaffected at 34.6 mAcm^{-2} and FF slightly decreased to 75.1%. At the highest defect density of 10^{16} cm^{-3}, the degradation was most severe: the PCE dropped to 6.25%, V_{OC} diminished drastically to 0.281 V, and FF reduced to 64.2%, whereas J_{SC} was almost unchanged. Overall, the figure demonstrates that the photovoltaic performance of the SnS_2-based device is highly sensitive to interfacial defect density. Maintaining a low interface defect concentration is therefore essential to preserving high V_{OC} and FF, thereby ensuring efficient device operation.

3.5.7 *J*–*V* and *Q*–*E* curves for solar cell. Fig. 10(a) presents the current density–voltage (*J*–*V*) characteristics of $TlPbI_3$-based perovskite solar cells incorporating three different ETLs: Device 1 (CdS), Device 2 (In_2S_3), and Device 3 (SnS_2). The curves reveal the distinct influence of ETL selection on the photovoltaic performance, particularly in terms of V_{OC} and overall current density response. For Device 1, the *J*–*V* curve exhibits a near-rectangular shape, indicative of efficient charge extraction and suppressed recombination. The device maintains a nearly constant photocurrent density of 34.5 mAcm^{-2} across the forward bias range until 0.78 V, where a sharp decline occurs, defining the V_{OC} at approximately 0.794 V. Device 3 shows very similar behavior to Device 1, with a nearly identical photocurrent density (34.6 mAcm^{-2}) and a V_{OC} close to 0.794 V, though with a slightly earlier current roll-off, suggesting marginally higher interfacial recombination losses compared to CdS. In contrast, Device 2 displays markedly inferior performance. Although the initial photocurrent density remains comparable (34.4 mAcm^{-2} at 0 V), the current density decreases significantly with increasing bias, dropping to near-zero at 0.56 V. Overall, the *J*–*V* analysis indicates that CdS and SnS_2 ETLs enable superior device performance with high current density retention and higher V_{OC}, whereas In_2S_3 leads to substantial performance degradation due to recombination and interfacial mismatch. This comparison highlights the critical role of ETL

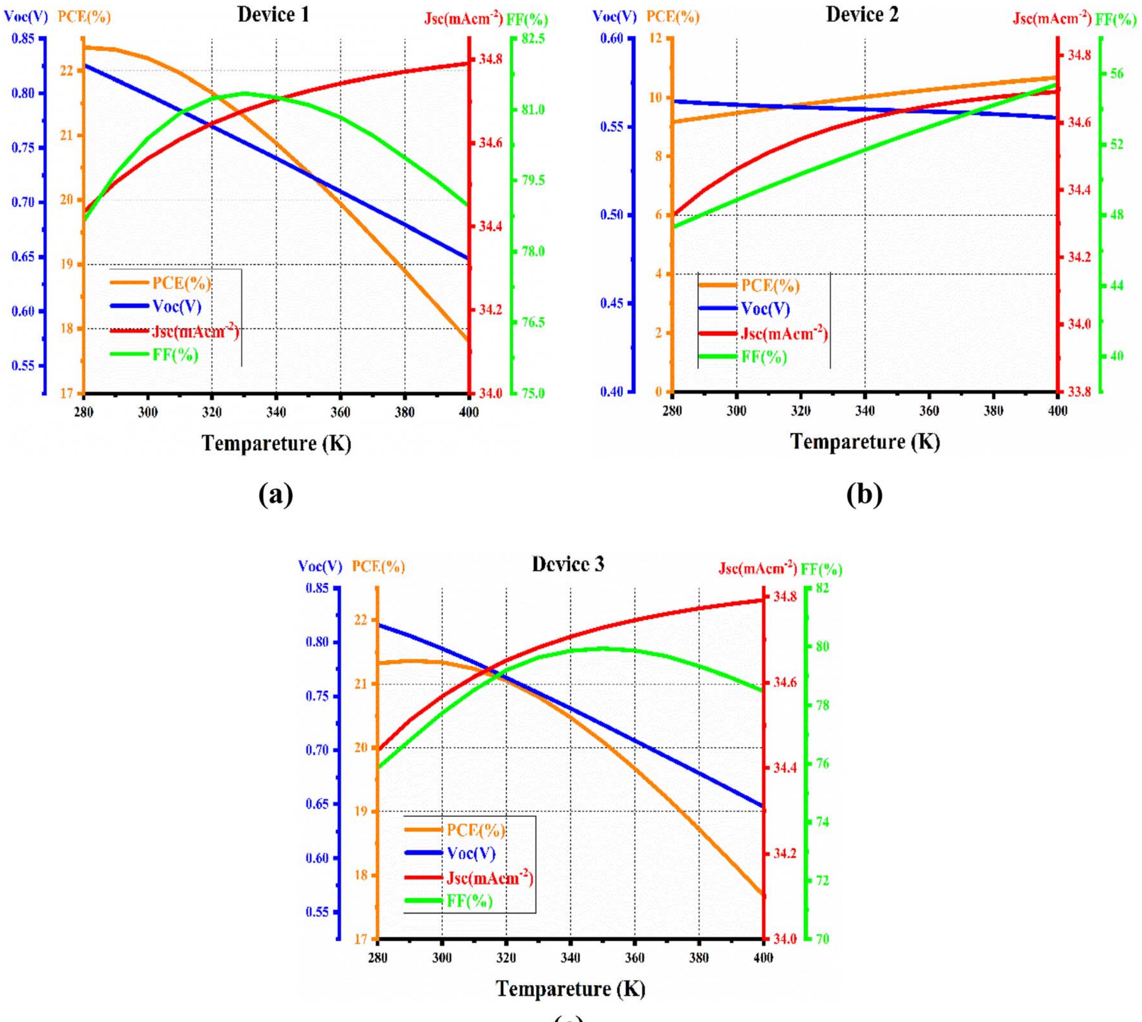

(a) (b)

(c)

Fig. 11 The effect of temperature on the photovoltaic performance of the (a) Device 1(CdS), (b) Device 2(In_2S_3), and (c) Device 3(SnS_2).

selection in optimizing charge transport and minimizing losses in $TlPbI_3$-based perovskite solar cells.

Fig. 10(b) presents the External Quantum Efficiency (EQE) spectra of $TlPbI_3$-based perovskite solar cells incorporating three distinct ETLs: CdS (Device 1), In_2S_3 (Device 2), and SnS_2 (Device 3), across the 300–1000 nm range. The EQE spectra provide direct insight into the wavelength-dependent photo response of the devices and the effectiveness of ETL selection in facilitating photo-generated carrier collection. All devices exhibit high photo response in the UV-visible region (300–800 nm), with EQE values nearing unity (95–100%), indicating efficient photon-to-electron conversion by the $TlPbI_3$ absorber and effective carrier extraction by the ETLs. Among them, Device 1 demonstrates the highest EQE across the spectrum, maintaining nearly flat, near 100% efficiency between 350–800 nm, reflecting superior electron mobility and minimal recombination at the CdS/perovskite interface. Device 2 shows slightly lower EQE, particularly beyond 700 nm, suggesting moderate recombination losses due to imperfect band alignment. Device 3 exhibits the weakest response, with EQE dropping sharply past 700 nm, indicating higher interfacial recombination and reduced charge transport efficiency. All spectra decline beyond 850 nm, reaching zero near 1000 nm, consistent with the $TlPbI_3$ bandgap (1.26 eV). The stronger spectral response of CdS devices corresponds to higher J_{SC} and overall power conversion efficiency. These results confirm that ETL choice critically impacts carrier collection, with CdS offering optimal band alignment and minimal recombination losses for superior device performance.

3.5.8 Effect of temperature on the performance of the solar cells. The impact of temperature variation, ranging from 280 K to 400 K, on the PV characteristics of PSCs has been thoroughly investigated through detailed numerical simulations, as illustrated in Fig. 11. Across this temperature span, the rates of carrier generation and recombination remain relatively balanced. However, with increasing temperature, a noticeable decline in device efficiency is observed for all structural configurations except device 2, primarily resulting from intensified charge carrier recombination and a rise in reverse saturation current density (J_0).[102]

Fig. 11(a) illustrates the influence of temperature on the photovoltaic parameters of the $TlPbI_3$-based perovskite solar cell employing CdS as the ETL (Device 1). The results reveal a clear temperature-dependent trend in device performance. The PCE exhibits a maximum value of 22.4% at 280 K and decreases steadily with rising temperature, reaching 17.8% at 400 K, primarily due to reductions in the V_{OC} and FF. The V_{OC} shows a nearly linear decline from 0.826 V at 280 K to 0.648 V at 400 K, consistent with enhanced non-radiative recombination and increased saturation current density at elevated temperatures. In contrast, the J_{SC} demonstrates a slight upward trend, increasing from 34.4 to 34.8 mA cm^{-2} across the same temperature range, which can be attributed to improved charge carrier mobility and reduced resistive losses at higher thermal energies. The FF initially rises from 78.6% at 280 K to a peak of 81.3% around 330–340 K, suggesting improved carrier extraction at moderate temperatures, but subsequently declines to 79.0% at 400 K due to recombination and resistive effects. Overall, the analysis indicates that Device 1 achieves optimal performance in the low-temperature region (280–300 K), where high V_{OC} and stable FF values sustain efficiencies above 22%. However, at elevated temperatures, efficiency degradation becomes evident, emphasizing the thermal sensitivity of CdS-based $TlPbI_3$ perovskite solar cells and the need for strategies to enhance stability under operational conditions.

Fig. 11(b) presents the temperature-dependent photovoltaic characteristics of the $TlPbI_3$-based perovskite solar cell using In_2S_3 as the ETL (Device 2). Unlike Device 1, this device shows an improvement in overall performance with increasing temperature. The PCE gradually rises from 9.17% at 280 K to 10.7% at 400 K, primarily driven by enhancements in the FF and J_{SC}. The FF exhibits a significant and nearly linear increase from 47.3% at 280 K to 55.4% at 400 K, indicating better charge extraction and reduced series resistance at elevated temperatures. Similarly, J_{SC} increases slightly from 34.3 to 34.7 mA cm^{-2}, reflecting improved carrier mobility. In contrast, the V_{OC} shows a slow but consistent decline, decreasing from 0.565 V at 280 K to 0.555 V at 400 K, which is consistent with enhanced recombination at higher temperatures. Despite this reduction in V_{OC}, the positive contributions from FF and J_{SC} dominate, leading to the observed rise in efficiency.

Fig. 11(c) illustrates the variation of photovoltaic parameters of the $TlPbI_3$-based perovskite solar cell employing SnS_2 as the ETL (Device 3) under different operating temperatures. The PCE starts at 21.3% at 280 K, reaching a maximum of 21.4% near 290 K, before showing a gradual decline with increasing temperature, dropping to 17.7% at 400 K. This reduction is primarily attributed to the continuous decrease in V_{OC}, which decreases monotonically from 0.816 V at 280 K to 0.648 V at 400 K, reflecting increased non-radiative recombination losses at elevated temperatures. The J_{SC}, on the other hand, shows a slight but steady increase with temperature, rising from 34.4 mA cm^{-2} at 280 K to 34.8 mA cm^{-2} at 400 K, which indicates enhanced carrier mobility and photo generation under thermal excitation. The FF improves initially from 75.9% at 280 K to around 79.9% at 340–360 K, before stabilizing and exhibiting a minor decline at higher temperatures, finishing at 78.5% at 400 K. Despite the modest improvement in J_{SC} and FF, the sharp decline in V_{OC} dominates the device behavior, resulting in the observed drop in PCE at elevated temperatures. These results highlight that while SnS_2-based devices exhibit strong efficiency at low to moderate temperatures, their thermal stability is limited by voltage losses, suggesting the necessity of further optimization for stable operation under high-temperature conditions.

3.5.9 The impact of shunt and series resistance on solar cell performance.

Fig. 12(a) presents the variation of V_{OC} of the $TlPbI_3$-based perovskite solar cell with CdS as the ETL (Device 1) as a function of both series resistance (R_s) and shunt resistance (R_{sh}). The 3D bar chart demonstrates that V_{OC} remains largely stable across a wide range of R_s and R_{sh} values, indicating minimal dependence of this parameter on resistance variations. At very low resistance conditions ($R_{sh} = 0\ \Omega\ cm^2$, $R_s = 0\ \Omega\ cm^2$), the V_{OC} is negligible (3.46×10^{-8} V), confirming strong leakage pathways and recombination losses. However, as R_{sh} increases beyond 200 Ω cm^2, V_{OC} rises sharply to approximately 0.794 V and then stabilizes. Further increments in both R_{sh} (200–1400 Ω cm^2) and R_s (0–7 Ω cm^2) result in only marginal improvements, with V_{OC} saturating around 0.798–0.799 V. This behavior signifies that the device is relatively insensitive to R_s but highly influenced by R_{sh}, especially at low shunt resistance, where leakage currents dominate. Once R_{sh} exceeds a threshold, the V_{OC} plateaus, reflecting the intrinsic V_{OC} limit of the device. Overall, the results indicate that CdS-based Device 1 maintains excellent V_{OC} stability under varying resistance conditions, provided that shunt leakage is minimized, which is crucial for achieving high device reliability and efficiency.

Fig. 12(b) shows the dependence of the J_{SC} of the $TlPbI_3$-based perovskite solar cell with CdS as the ETL (Device 1) on R_s and R_{sh}. The 3D bar chart indicates that J_{SC} is highly sensitive to shunt resistance at very low values but remains remarkably stable once R_{sh} exceeds 200 Ω cm^2. At $R_{sh} = 0\ \Omega\ cm^2$ and $R_s = 0\ \Omega\ cm^2$, the J_{SC} is at its maximum (34.6 mA cm^{-2}). However, when R_s is introduced under the same low R_{sh} condition, J_{SC} drops drastically to negligible values (10^{-9}–10^{-6} mA cm^{-2}), reflecting severe recombination and leakage current pathways. In contrast, as R_{sh} increases to 200 Ω cm^2 and beyond, J_{SC} recovers significantly, maintaining values in the range of 33.3–34.6 mA cm^{-2} across the R_s sweep (0–7 Ω cm^2). Further increments in R_{sh} (400–1400 Ω cm^2) stabilize J_{SC} around 34.2–34.6 mA cm^{-2}, showing only minor dependence on R_s. This behavior highlights that shunt resistance primarily governs J_{SC} in Device 1, with minimal sensitivity to series resistance at practical operating conditions. The results demonstrate the robustness of CdS-based devices in preserving photocurrent density, provided shunt leakage is minimized, which is crucial for achieving high PCE.

Fig. 12(c) illustrates the variation of the FF of the $TlPbI_3$-based perovskite solar cell employing CdS as the ETL (Device 1) with respect to both R_s and R_{sh}. The results reveal that FF is strongly dependent on both parameters, unlike V_{OC}, which was relatively stable. At very low shunt resistance ($R_{sh} = 0\ \Omega\ cm^2$), the FF is completely suppressed (0%), reflecting severe leakage current losses. As R_{sh} increases to 200 Ω cm^2, the FF recovers significantly, reaching values between 53.7% and 72.2%, depending on the corresponding R_s. Further increases in R_{sh}

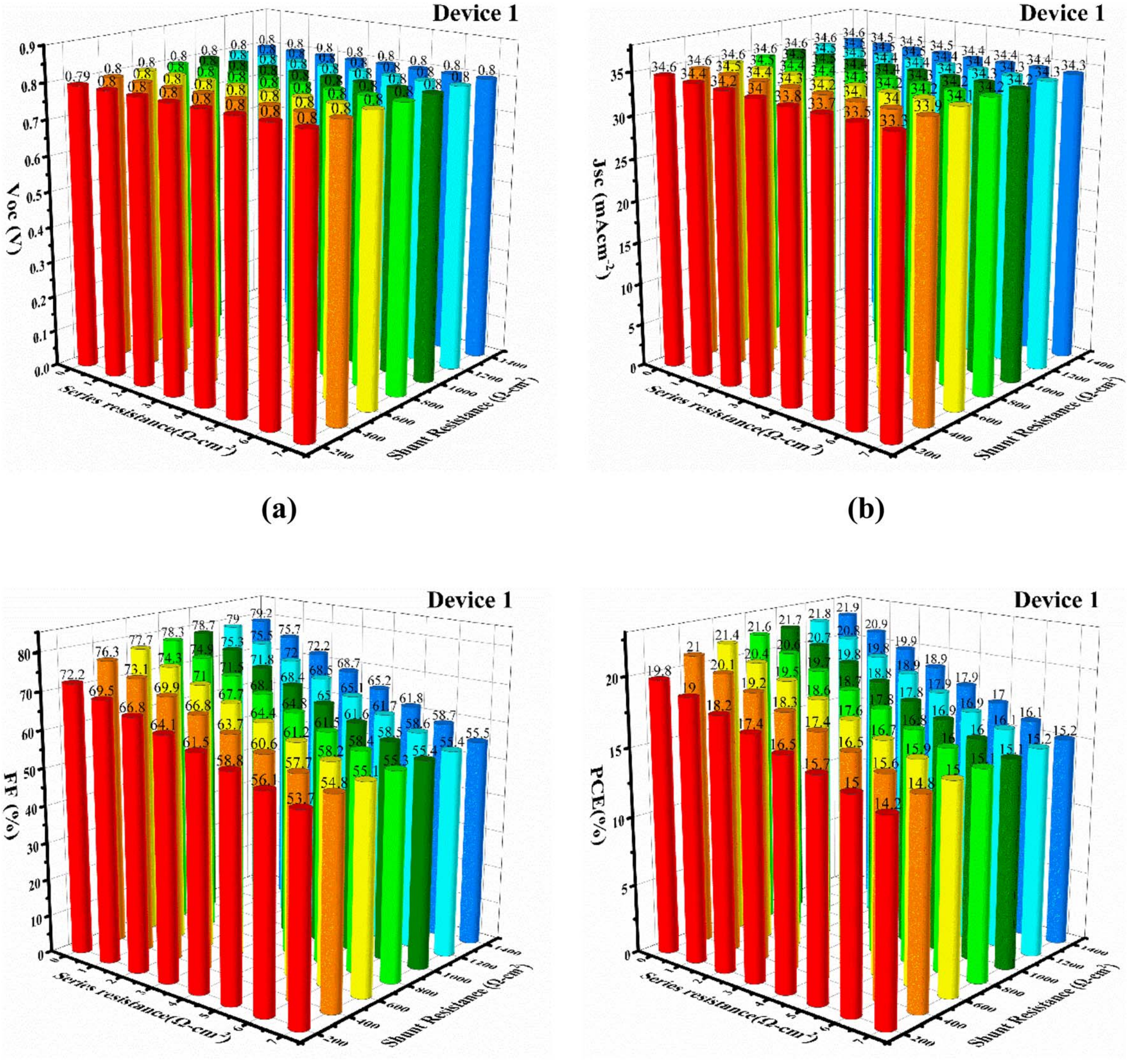

(a) (b)

(c) (d)

Fig. 12 Effects on PV performance parameters for changing the series and shunt resistance (a) $V_{OC,}$ (b) $J_{SC,}$ (c) FF, and (d) PCE of device 1(CdS) for the best-optimized framework.

lead to a steady improvement in FF, with the values reaching 79.2% at $R_{sh} = 1400\ \Omega\ cm^2$ and $R_s = 0\ \Omega\ cm^2$. However, the influence of R_s becomes apparent across all R_{sh} values: at higher R_s, FF decreases gradually due to resistive losses, dropping from 79.2% at $R_s = 0\ \Omega\ cm^2$ to 55.5% at $R_s = 7\ \Omega\ cm^2$ (when $R_{sh} = 1400\ \Omega\ cm^2$). This behavior indicates that minimizing both series resistance and shunt leakage is crucial for maintaining a high FF. Overall, Device 1 shows strong resilience at moderate to high R_{sh} values, with FF saturating near 78–79% when R_s is minimized, underscoring the importance of contact quality and resistance optimization in achieving high device performance.

Fig. 12(d) illustrates the effect of varying R_s and R_{sh} on the PCE of Device 1. The 3D bar chart clearly shows that PCE is highly sensitive to both resistive parameters. At very low shunt resistance ($R_{sh} = 0\ \Omega\ cm^2$), the PCE is essentially zero regardless of the series resistance, reflecting strong leakage pathways that dominate device performance. As R_{sh} increases to 200 $\Omega\ cm^2$, the PCE improves significantly, reaching values between 14.2% and 19.8%, depending on the R_s value. With further increases in R_{sh} up to 1400 $\Omega\ cm^2$, the PCE continues to improve, stabilizing in the range of 15.2% to 21.9%. The series resistance also influences the efficiency trend. At low R_s (0–1 $\Omega\ cm^2$), the PCE reaches its maximum values, peaking around 21.9% for $R_{sh} = 1400\ \Omega\ cm^2$. However, as R_s increases to 7 $\Omega\ cm^2$, the PCE declines notably, dropping to 15.2% even at high R_{sh}. This indicates that higher series resistance limits charge transport and reduces overall device performance. In summary, the figure demonstrates that Device 1 achieves optimal efficiency under conditions of low series resistance and high shunt resistance, where charge extraction is maximized, and leakage losses are minimized. The highest PCE (21.9%) is achieved at $R_s = 0\ \Omega\ cm^2$ and $R_{sh} \geq 1200\ \Omega\ cm^2$, while efficiency steadily decreases with increasing R_s or decreasing R_{sh}.

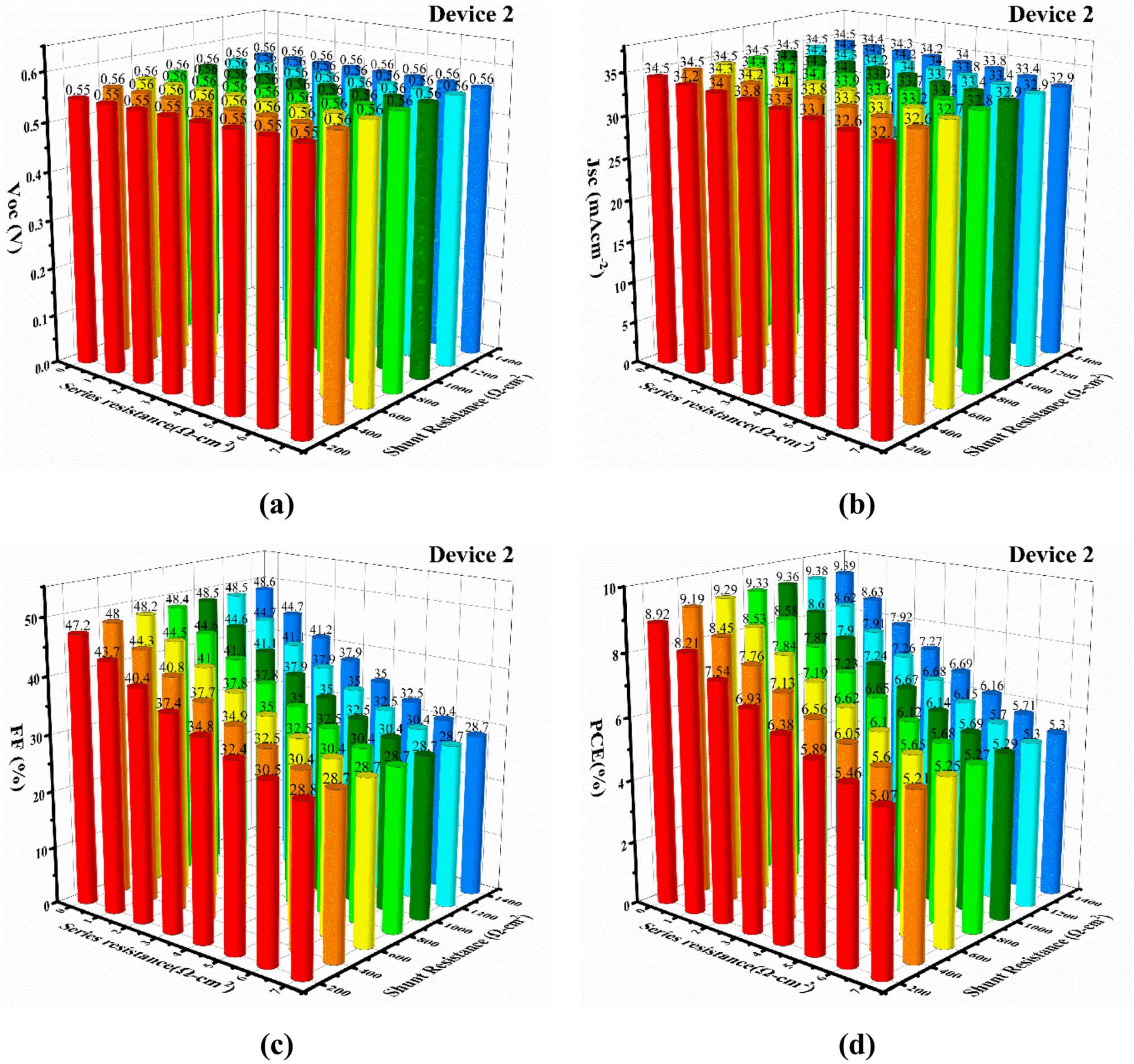

(a) (b)

(c) (d)

Fig. 13 Effects on PV performance parameters for changing the series and shunt resistance (a) $V_{OC,}$ (b) $J_{SC,}$ (c) FF, and (d) PCE of device 2(In_2S_3) for the best-optimized framework.

Fig. 13(a) for Device 2 employing In_2S_3 ETL illustrates the variation of V_{OC} as a function of both R_s and R_{sh}. The data show that at very low shunt resistance ($R_{sh} = 0\ \Omega\ cm^2$), V_{OC} is almost negligible (3.45×10^{-8} V), which reflects strong leakage current suppressing voltage generation. However, as R_{sh} increases to 200 Ω cm^2, V_{OC} sharply improves to around 0.548–0.549 V, and further rises with increasing R_{sh}. At higher values of R_{sh} (≥400 Ω cm^2), V_{OC} stabilizes in the range of 0.556–0.561 V, showing only minimal changes with further increases in resistance. Interestingly, series resistance has almost no significant effect on V_{OC} across the entire range; the bars remain nearly constant for each R_{sh} level, indicating that V_{OC} is mainly governed by R_{sh} rather than R_s. The maximum V_{OC} observed is approximately 0.561 V, achieved at $R_s = 0–7\ \Omega\ cm^2$ and $R_{sh} \geq 1200\ \Omega\ cm^2$. In summary, this figure demonstrates that V_{OC} in Device 2 is strongly dependent on shunt resistance, with higher R_{sh} values suppressing leakage currents and thereby allowing V_{OC} to reach its maximum stable value (0.56 V). Conversely, series resistance does not play a major role in V_{OC} performance for this device.

Fig. 13(b) for Device 2 demonstrates the variation of the J_{SC} as a function of both R_s and R_{sh}. The results indicate that J_{SC} is relatively less sensitive to R_s and R_{sh} compared to other photovoltaic parameters like V_{OC} and FF, but noticeable trends are still observed. At very low $R_{sh} = 0\ \Omega\ cm^2$, J_{SC} drops drastically, with values collapsing from 34.5 mA cm^{-2} (at $R_s = 0\ \Omega\ cm^2$) to almost negligible levels (4.9×10^{-6} mA cm^{-2} at $R_s = 7\ \Omega\ cm^2$). This sharp decline highlights that low shunt resistance causes severe leakage current, leading to significant current loss. As R_{sh}

increases to 200 Ω cm^2, J_{SC} improves substantially, ranging from 34.5 mA cm^{-2} at $R_s = 0$ Ω cm^2 to 32.1 mA cm^{-2} at $R_s = 7$ Ω cm^2. This demonstrates that higher series resistance slightly reduces current extraction efficiency, but the effect is moderate compared to the shunt resistance influence. For higher R_{sh} values (400–1400 Ω cm^2), J_{SC} remains relatively stable, ranging between 34.5 and 32.9 mA cm^{-2} across the R_s range. The maximum J_{SC} (34.5 mA cm^{-2}) is observed at low R_s (0 Ω cm^2) and high R_{sh} (≥400 Ω cm^2), while the lowest values (32.9 mA cm^{-2}) occur at high Rs (7 Ω cm^2), even when R_{sh} is large. In summary, Fig. 13(b) shows that J_{SC} in Device 2 is strongly suppressed by very low shunt resistance due to leakage pathways. Once R_{sh} exceeds 200 Ω cm^2, J_{SC} becomes more stable and only slightly decreases with increasing R_s.

Fig. 13(c) for Device 2 illustrates the effect of both R_s and R_{sh} on the FF. The data reveal that FF is highly sensitive to variations in both R_s and R_{sh}. At a very low shunt resistance ($R_{sh} = 0$ Ω cm^2), the FF remains at 0%, indicating that strong leakage pathways prevent efficient power conversion. As R_{sh} increases to 200 Ω cm^2, FF rises significantly, ranging from about 47.2% (at $R_s = 0$ Ω cm^2) down to 28.8% (at $R_s = 7$ Ω cm^2). This demonstrates that higher series resistance degrades FF even when shunt resistance is moderately high. Further increases in R_{sh} (400–1400 Ω cm^2) lead to an improvement and stabilization of FF values. For low R_s (0–1 Ω cm^2), FF achieves its highest values of 48.6%, reflecting efficient device performance. However, at higher R_s (6–7 Ω cm^2), FF saturates at 28.7%, showing that excessive series resistance strongly limits fill factor regardless of

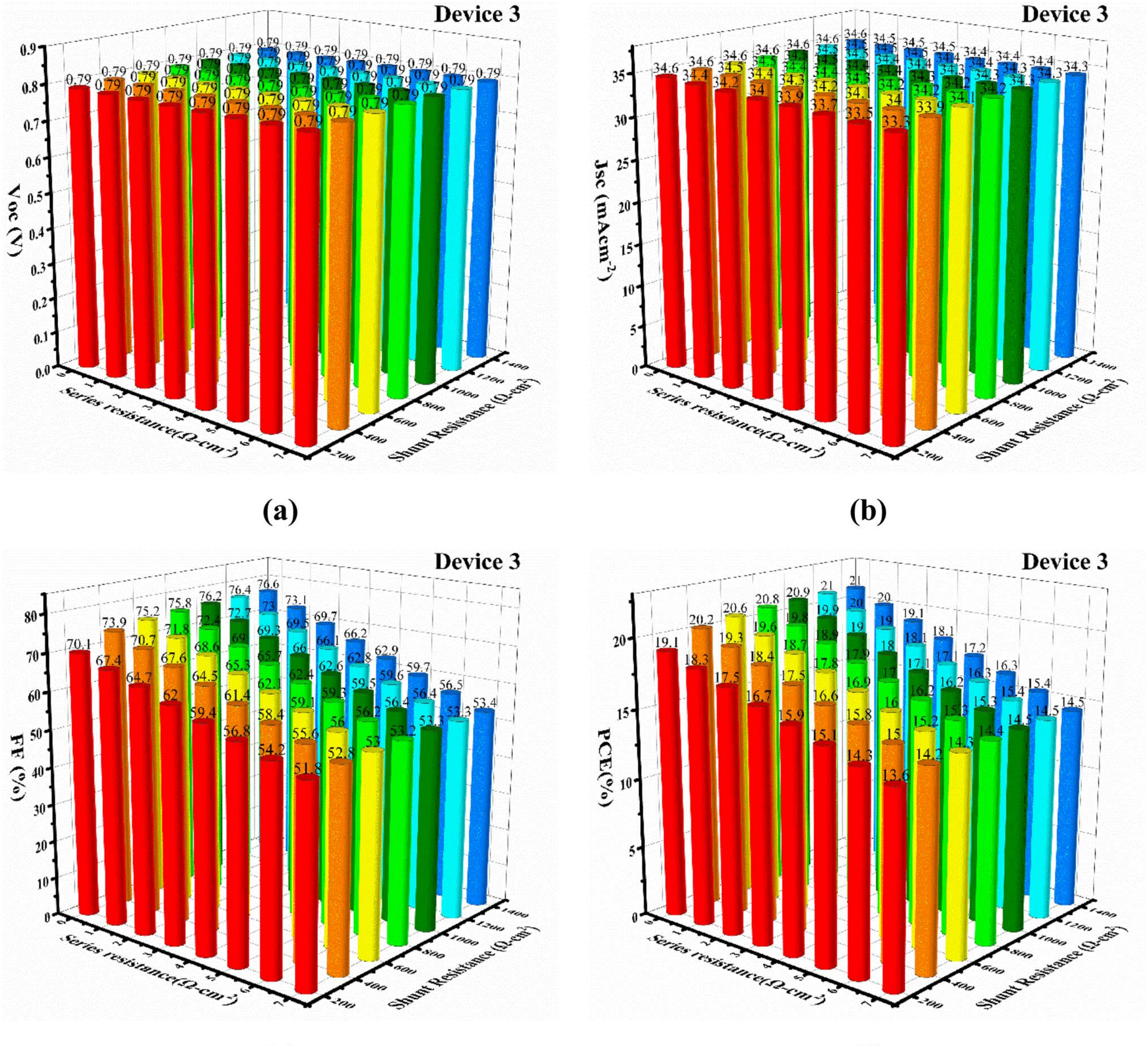

Fig. 14 Effects on PV performance parameters for changing the series and shunt resistance (a) $V_{OC,}$ (b) $J_{SC,}$ (c) FF, and (d) PCE of device 3(SnS$_2$) for the best-optimized framework.

R_{sh} improvements. In summary, Fig. 13(c) shows that FF in Device 2 improves with increasing shunt resistance, reaching maximum values above 48% for low series resistance. However, as series resistance increases, FF rapidly decreases, highlighting that while high shunt resistance suppresses leakage and improves efficiency, minimizing series resistance is critical for maintaining high FF.

Fig. 13(d) for Device 2 illustrates the variation of PCE with respect to both series resistance (R_s) and shunt resistance (R_{sh}). This 3D plot highlights the combined influence of parasitic resistances on overall device efficiency. At a very low shunt resistance ($R_{sh} = 0\ \Omega\ cm^2$), the PCE collapses completely (0%), regardless of R_s. This indicates that leakage currents dominate, preventing any useful power generation. When R_{sh} increases to 200 Ω cm^2, the PCE improves significantly, ranging from 8.92% at $R_s = 0\ \Omega\ cm^2$ to 5.07% at $R_s = 7\ \Omega\ cm^2$. This clearly shows that higher series resistance reduces efficiency due to resistive losses in current transport. For higher R_{sh} values (400–1400 Ω cm^2), PCE continues to rise and eventually stabilizes. At low R_s (0 Ω cm^2), maximum PCE values are obtained, reaching 9.39%. As R_s increases, PCE gradually decreases: for instance, at $R_s = 7\ \Omega$ cm^2, PCE drops to 5.3%, even when R_{sh} is high. Overall, the figure demonstrates that Device 2 achieves its best performance (PCE $\approx$ 9.39%) under the condition of high R_{sh} ($\geq$800 Ω cm^2) and very low R_s (0–1 Ω cm^2). On the other hand, poor shunt resistance or excessive series resistance strongly reduces efficiency.

Fig. 14(a) for Device 3 employing SnS_2 ETL illustrates the dependence of the V_{OC} on both R_s and R_{sh}. At $R_{sh} = 0\ \Omega\ cm^2$, the device V_{OC} is practically zero (3.46×10^{-8} V), indicating complete leakage losses, which is expected in the absence of shunt resistance. However, once R_{sh} increases to 200 Ω cm^2, V_{OC} rises sharply to 0.789 V and remains nearly constant as R_s increases from 0 to 7 Ω cm^2. As R_{sh} continues to increase (400–1400 Ω cm^2), V_{OC} further improves, reaching 0.794 V, with only a slight positive shift across higher R_{sh} values. Importantly, changes in R_s have almost no impact on V_{OC}, as all bars across the R_s axis remain at nearly the same height. Overall, this figure demonstrates that shunt resistance rather than series resistance dominates V_{OC} in Device 3. Once R_{sh} is sufficiently high ($\geq$600 Ω cm^2), V_{OC} stabilizes around 0.794 V, reflecting efficient charge separation and minimal recombination. The consistently high V_{OC} values also highlight the good intrinsic quality of Device 3 compared to other devices.

Fig. 14(b) presents the variation of the J_{SC} of Device 3 as a function of R_s and R_{sh}. At $R_{sh} = 0\ \Omega\ cm^2$, J_{SC} shows abnormal behavior: while the first data point at $R_s = 0\ \Omega\ cm^2$ gives a value of 34.6 mA cm^{-2}, subsequent values drop drastically to negligible levels (in the order of 10^{-5} to 10^{-6} mA cm^{-2}). This indicates severe current leakage through the device at zero shunt resistance, which prevents efficient charge collection. With increasing R_{sh} ($\geq$200 Ω cm^2), J_{SC} stabilizes at significantly higher values. For example, at $R_{sh} = 200\ \Omega\ cm^2$, J_{SC} ranges from 34.6 mA cm^{-2} ($R_s = 0\ \Omega\ cm^2$) to 33.3 mA cm^{-2} ($R_s = 7\ \Omega\ cm^2$). The general trend shows a gradual decrease in J_{SC} with rising Rs, consistent with the expected effect of ohmic losses that hinder current extraction. As R_{sh} increases further, J_{SC} approaches saturation. At $R_{sh} = 600\ \Omega\ cm^2$, the J_{SC} values remain in the range of 34.6–34.1 mA cm^{-2}, while at the maximum studied R_{sh} of 1400 Ω cm^2, J_{SC} becomes nearly constant, varying only slightly between 34.6 mA cm^{-2} ($R_s = 0\ \Omega$ cm^2) and 34.3 mA cm^{-2} (Rs = 7 Ω cm^2). This behavior indicates that once the shunt resistance is sufficiently high, leakage pathways are minimized, and J_{SC} is mainly determined by intrinsic photo generation and carrier collection efficiency. Overall, Fig. 14(b) demonstrates that J_{SC} is strongly dependent on R_{sh} at low values, but becomes nearly independent once R_{sh} exceeds 600 Ω cm^2. In contrast, increasing R_s consistently reduces J_{SC}, although the effect is relatively minor compared to that of R_{sh}.

Fig. 14(c) illustrates the variation of the FF of Device 3 as a function of both R_s and R_{sh}. At $R_{sh} = 0\ \Omega\ cm^2$, the FF is zero across all values of R_s, indicating complete current leakage and the absence of diode functionality in the device under this condition. Once R_{sh} increases to 200 Ω cm^2, the FF rises significantly, reaching values between 70.1% (at $R_s = 0\ \Omega\ cm^2$) and 51.8% (at Rs = 7 Ω cm^2). This strong dependence highlights the critical role of shunt resistance in suppressing leakage pathways and improving the device's rectifying behavior. As R_{sh} continues to increase, the FF improves further. For instance, at $R_{sh} = 600\ \Omega\ cm^2$, FF values range from 75.2% ($R_s = 0\ \Omega\ cm^2$) to 53.0% ($R_s = 7\ \Omega\ cm^2$), while at the highest examined R_{sh} of 1400 Ω cm^2, FF stabilizes around 76.6% ($R_s = 0\ \Omega\ cm^2$) and 53.4% (Rs = 7 Ω cm^2). These results clearly indicate that higher shunt resistance significantly enhances FF, though the positive effect diminishes once R_{sh} exceeds 800 Ω cm^2. On the other hand, increasing R_s consistently reduces FF, with the decline being more pronounced at lower R_{sh} values. For example, at $R_{sh} = 200\ \Omega$ cm^2, the FF decreases from 70.1% at $R_s = 0\ \Omega\ cm^2$ to only 51.8% at $R_s = 7\ \Omega\ cm^2$. Even at higher R_{sh} values, this negative influence of R_s persists, reflecting its impact on series ohmic losses, which limit current extraction and PCE. In summary, Fig. 14(c) demonstrates that the FF of Device 3 is highly sensitive to both R_s and R_{sh}.

Fig. 14(d) illustrates the dependence of the PCE of Device 3 on variations in R_s and R_{sh}. The results demonstrate the strong sensitivity of PCE to both resistive parameters, highlighting their combined effect on device performance. At $R_{sh} = 0\ \Omega\ cm^2$, the device shows complete suppression of efficiency (0%) across all R_s values, which is attributed to severe current leakage and the inability of the cell to sustain charge separation under these conditions. As R_{sh} increases to 200 Ω cm^2, PCE improves significantly, ranging from 19.1% at $R_s = 0\ \Omega\ cm^2$ to 13.6% at $R_s = 7\ \Omega\ cm^2$. Further improvements are observed with increasing R_{sh}. At 600 Ω cm^2, PCE rises to 20.6% ($R_s = 0\ \Omega\ cm^2$) but gradually decreases with higher R_s, reaching 14.3% at $R_s = 7\ \Omega$ cm^2. This trend persists across higher R_{sh} values, with the highest efficiency obtained at R_{sh} = 1200–1400 Ω cm^2, where PCE stabilizes at 21.0% ($R_s = 0\ \Omega\ cm^2$). Even under these optimal conditions, PCE diminishes progressively with R_s, dropping to 14.5% at the maximum R_s of 7 Ω cm^2. Overall, the figure reveals that R_{sh} plays a more dominant role than R_s in governing device efficiency. Increasing R_{sh} beyond 800 Ω cm^2 leads to marginal improvements, suggesting that the device

Table 5 The $TlPbI_3$-based solar cell demonstrates superior power conversion efficiency relative to other perovskite solar cells reported with different device architectures

Structure	V_{OC} (V)	J_{SC} (mA cm^{-2})	FF (%)	PCE (%)	Ref.
FTO/CdS/$TlPbI_3$/Cu	0.7987	34.56	80.40	22.20	This work
FTO/In_2S_3/$TlPbI_3$/Cu	0.5626	34.46	48.86	9.47	This work
FTO/SnS_2/$TlPbI_3$/Cu	0.7941	34.57	77.74	21.34	This work
ITO/WS_2/$CsPbI_3$/CBTS/Au	0.997	20.98	85.22	17.82	103
FTO/TiO_2/$CsPbI_3$/PTAA/Au	1.084	19.72	75.70	16.07	103
FTO/SnO_2/$MAPbI_3$/Spiro-OMeTAD/Au	1.023	21.19	67.8	14.69	104
Perovskite QDSSC ($CH_3NH_3PbI_3/TiO_2$)	0.706	15.82	0.586	6.54	105

approaches saturation in suppressing leakage losses. In contrast, the negative influence of R_s remains consistent across all R_{sh} values, with higher R_s steadily degrading performance due to enhanced resistive losses. This analysis confirms that Device 3 achieves its maximum efficiency of 21.0% under conditions of low R_s ($\leq 1\ \Omega\ cm^2$) and high R_{sh} ($\geq 1200\ \Omega\ cm^2$). These results emphasize that optimizing both series and shunt resistances is essential to attaining high-performance $TlPbI_3$-based perovskite solar cells.

Table 5 compares the photovoltaic performance of the proposed $TlPbI_3$-based solar cells with reported perovskite devices. The FTO/CdS/$TlPbI_3$/Cu structure shows the best performance, achieving a PCE of 22.20% with J_{SC} = 34.56 mAcm^{-2}, V_{OC} = 0.7987 V, and FF = 80.40%. The FTO/SnS_2/$TlPbI_3$/Cu device also delivers a high efficiency of 21.34%, while the In_2S_3-based configuration exhibits a much lower PCE of 9.47% due to its reduced fill factor. Compared with reported $CsPbI_3$, $MAPbI_3$, and perovskite QD-based solar cells (PCE = 6.54–17.82%), the proposed $TlPbI_3$ devices demonstrate superior current density and overall efficiency, underscoring the effectiveness of CdS and SnS_2 as ETLs. It should be noted that the reported photovoltaic efficiencies are theoretical values predicted by the SCAPS-1D simulation under the assumed model parameters and optimized conditions, and therefore, they represent simulated device potential rather than experimentally demonstrated performance.

In practical applications, however, the actual device performance may be lower than the simulated values due to several non-ideal factors, including imperfect film quality, higher bulk and interface defect densities, trap-assisted recombination, contact resistance, unfavorable band alignment, and environmental or thermal instability during fabrication and operation. Moreover, achieving high-quality $TlPbI_3$ absorber layers with controlled stoichiometry and low defect concentration may be experimentally challenging, which can further limit the photovoltaic performance of real devices.

3.6 Machine learning-based analysis of solar cell parameters

3.6.1 Comparing random forest, gradient boosting, decision tree, and lightGBM models using MAE, R^2, and RMSE. The comparative performance analysis presented in Table 6 evaluates four machine learning models—random forest, gradient boosting, decision tree, and lightGBM—for predicting the photovoltaic performance of the three $TlPbI_3$-based solar devices: $TlPbI_3$–CdS, $TlPbI_3$–In_2S_3, and $TlPbI_3$–SnS_2. The dataset used for this analysis was generated from SCAPS-1D simulations and comprises 43 200 samples in total, with 14 400 data points for each device architecture. Model accuracy was assessed using R^2, RMSE, and MAE, which collectively reflect predictive precision and error magnitude. These metrics were computed using five-fold cross-validation, and the averaged values were reported to ensure a robust and unbiased evaluation of predictive performance. In addition, an 80 : 20 train-test split was employed to generate the actual-*versus*-predicted plots and related visual diagnostics, thereby providing a clear assessment of model generalization on unseen data. For

Table 6 Comparative performance metrics of random forest, gradient boosting, decision tree, and lightGBM models for PCE prediction across different devices

Device	Model	R^2	RMSE	MAE
$TlPbI_3$–CdS	Random forest	0.99944128	0.09597836	0.0512535
	Gradient boosting	0.90257883	1.26925004	0.99339494
	Decision tree	0.99965233	0.07503562	0.01707186
	LightGBM	0.99107396	0.38432883	0.28891486
$TlPbI_3$–In_2S_3	Random forest	0.99970416	0.06408461	0.03248777
	Gradient boosting	0.91537953	1.08466669	0.83863286
	Decision tree	0.99979735	0.05123015	0.00829792
	LightGBM	0.9920475	0.33272488	0.25447979
$TlPbI_3$–SnS_2	Random forest	0.99940735	0.0945991	0.05153306
	Gradient boosting	0.90967126	1.16968848	0.90770556
	Decision tree	0.99930062	0.1010263	0.01988236
	LightGBM	0.99143124	0.36003949	0.27640629

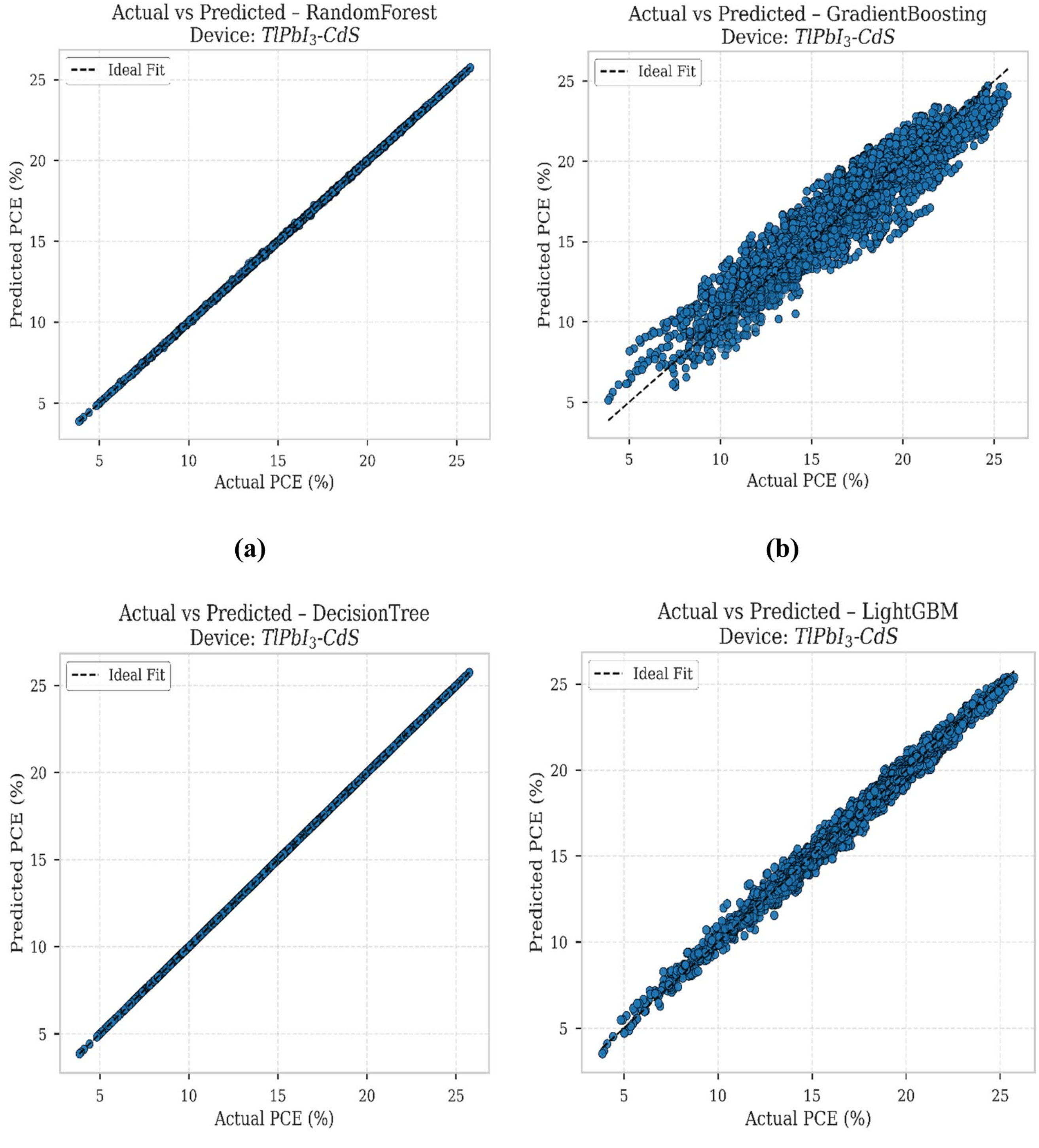

(a) (b)

(c) (d)

Fig. 15 Actual *vs.* predicted PCE using (a) random forest, (b) gradient boosting, (c) decision tree, and (d) lightGBM models for $TlPbI_3$–CdS-based device.

transparency and reproducibility, the complete dataset has also been provided in the SI.

Among the tested algorithms, the decision tree model consistently achieved the highest accuracy ($R^2 \approx 0.9993$–0.9998) with the lowest RMSE and MAE, indicating near-perfect prediction capability. Random Forest performed similarly well ($R^2 > 0.9994$), demonstrating excellent generalization and stability across all devices. In contrast, Gradient Boosting

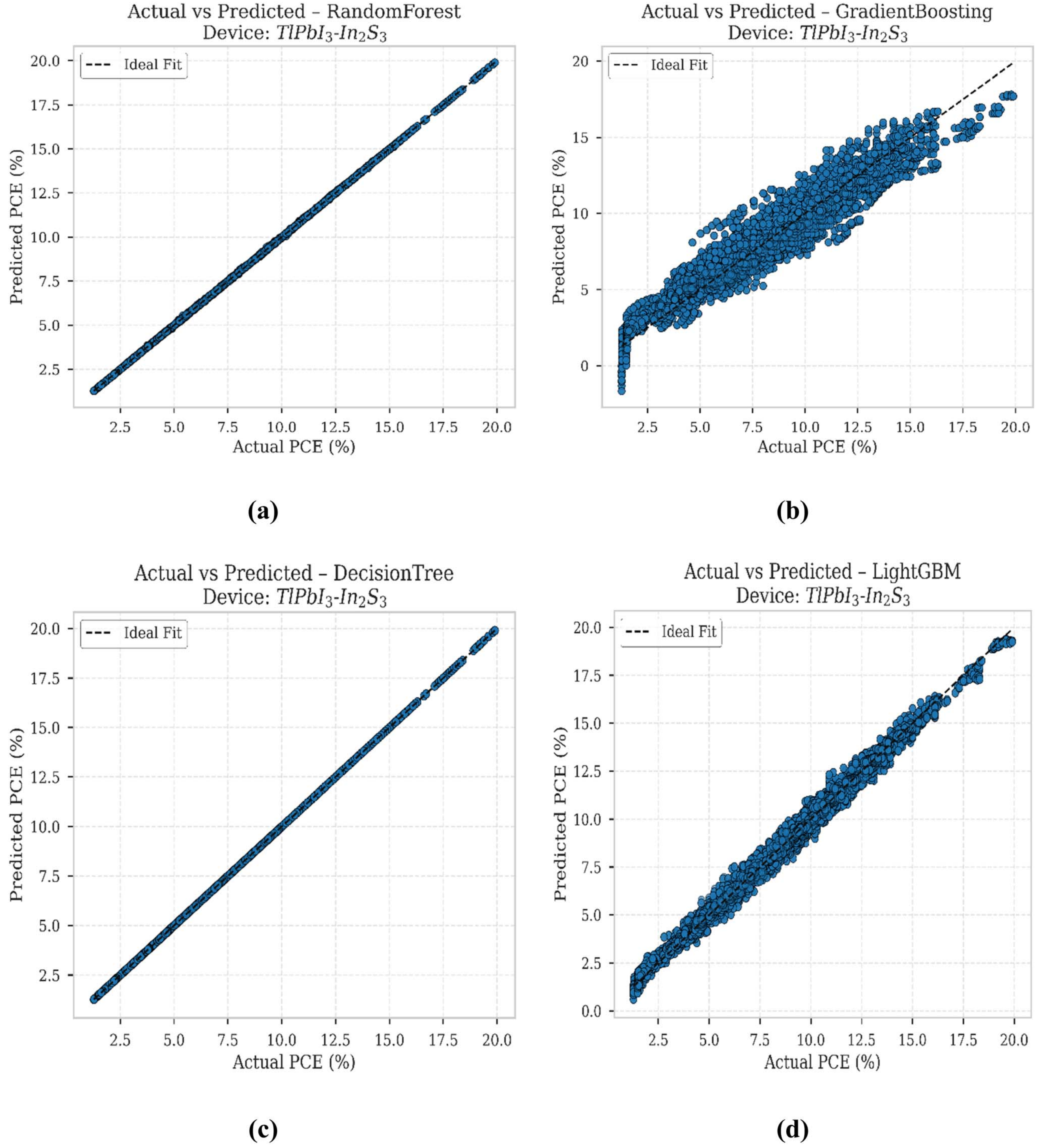

(a)

(b)

(c)

(d)

Fig. 16 Actual *vs.* predicted PCE using (a) random forest, (b) gradient boosting, (c) decision tree, and (d) lightGBM models for $TlPbI_3$–In_2S_3-based device.

showed markedly lower accuracy ($R^2 \approx 0.90$–0.91; RMSE $\approx$ 1.08–1.26; MAE $\approx$ 0.83–0.99), likely reflecting overfitting or inadequate hyperparameter optimization. LightGBM achieved intermediate results ($R^2 \approx 0.991$–0.992; RMSE $\approx$ 0.33–0.38; MAE $\approx$ 0.25–0.28), outperforming Gradient Boosting but lagging behind the top-performing tree-based models. Device-wise, the $TlPbI_3$–In_2S_3 configuration demonstrated the greatest predictive consistency across all algorithms, while $TlPbI_3$–SnS_2 exhibited slightly higher LightGBM and Gradient Boosting errors, possibly due to greater data variability or complex feature interactions. Overall, the findings highlight the superior capability of Decision Tree and Random Forest models in

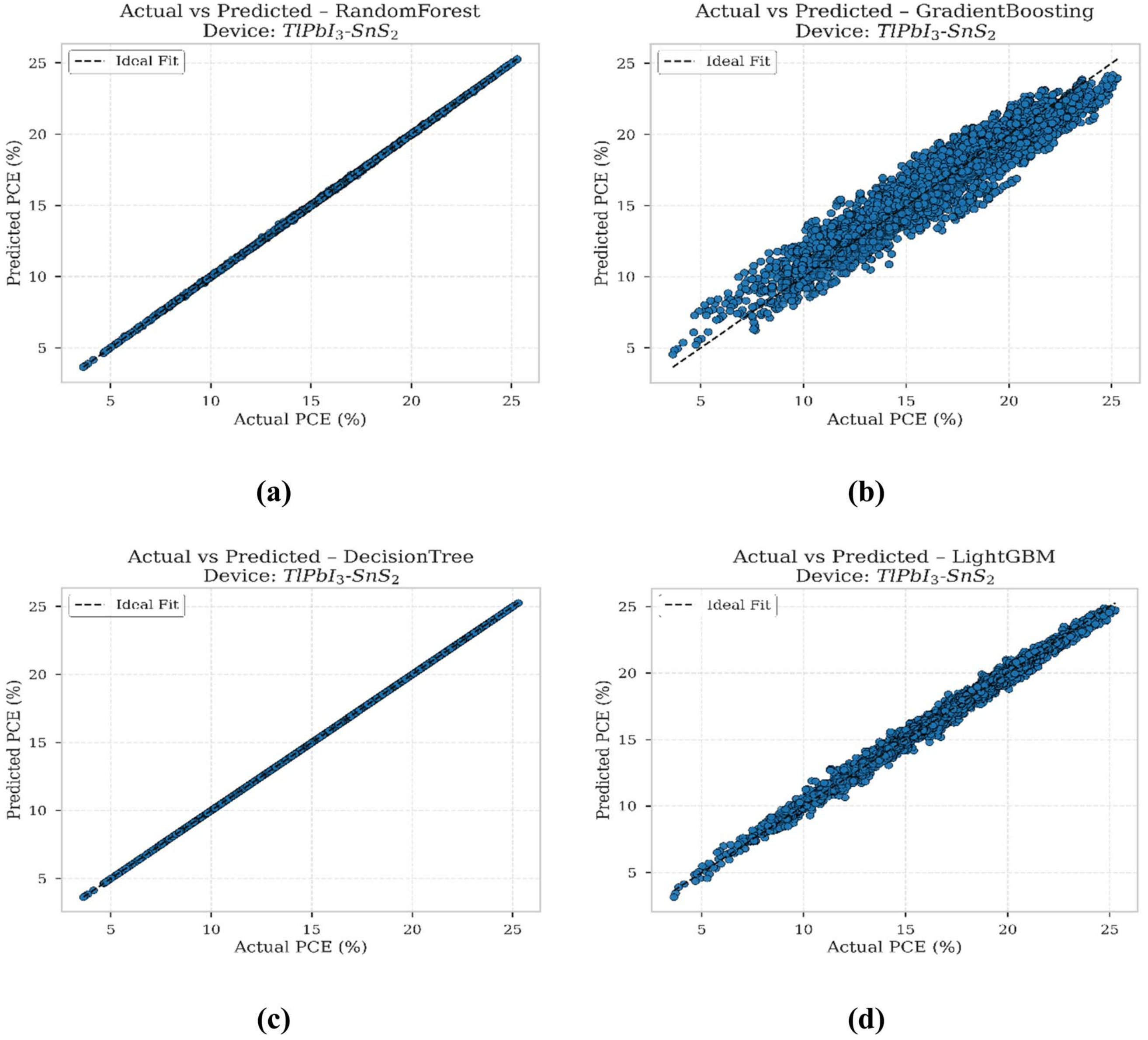

Fig. 17 Actual *vs.* predicted pce using (a) random forest, (b) gradient boosting, (c) decision tree, and (d) lightGBM models for $TlPbI_3$–SnS_2-based device.

capturing non-linear dependencies between material features and device efficiency, confirming their reliability for data-driven modeling of $TlPbI_3$-based photovoltaic systems.

3.6.2 Comparison between actual and predicted PCE using machine learning models. Fig. 15–17 illustrate the comparison between actual and predicted PCE values across four machine learning models—random forest, gradient boosting, decision tree, and lightgbm. In all cases, random forest and decision tree exhibit nearly perfect alignment along the ideal diagonal line, indicating highly accurate predictions. Gradient boosting shows larger deviations, particularly at lower PCE values, while LightGBM achieves moderately consistent results with slight scatter around the line. Overall, the results demonstrate that simpler tree-based ensemble models (random forest and decision tree) outperform the boosting models in predicting PCE for $TlPbI_3$-based devices.

In Fig. 15, the random forest and decision tree models (top-left and bottom-left) show nearly perfect alignment along the diagonal line, indicating very accurate predictions. In contrast, gradient boosting (top-right) and lightGBM (bottom-right) exhibit slight dispersion around the line, suggesting minor prediction errors.

For Fig. 16 showing the $TlPbI_3$–In_2S_3-based device, similar trends appear. The random forest and decision tree again show almost ideal one-to-one relationships, while gradient boosting reveals noticeable deviations at lower PCE values. LightGBM performs better than gradient boosting but still shows a wider spread than the tree-based models.

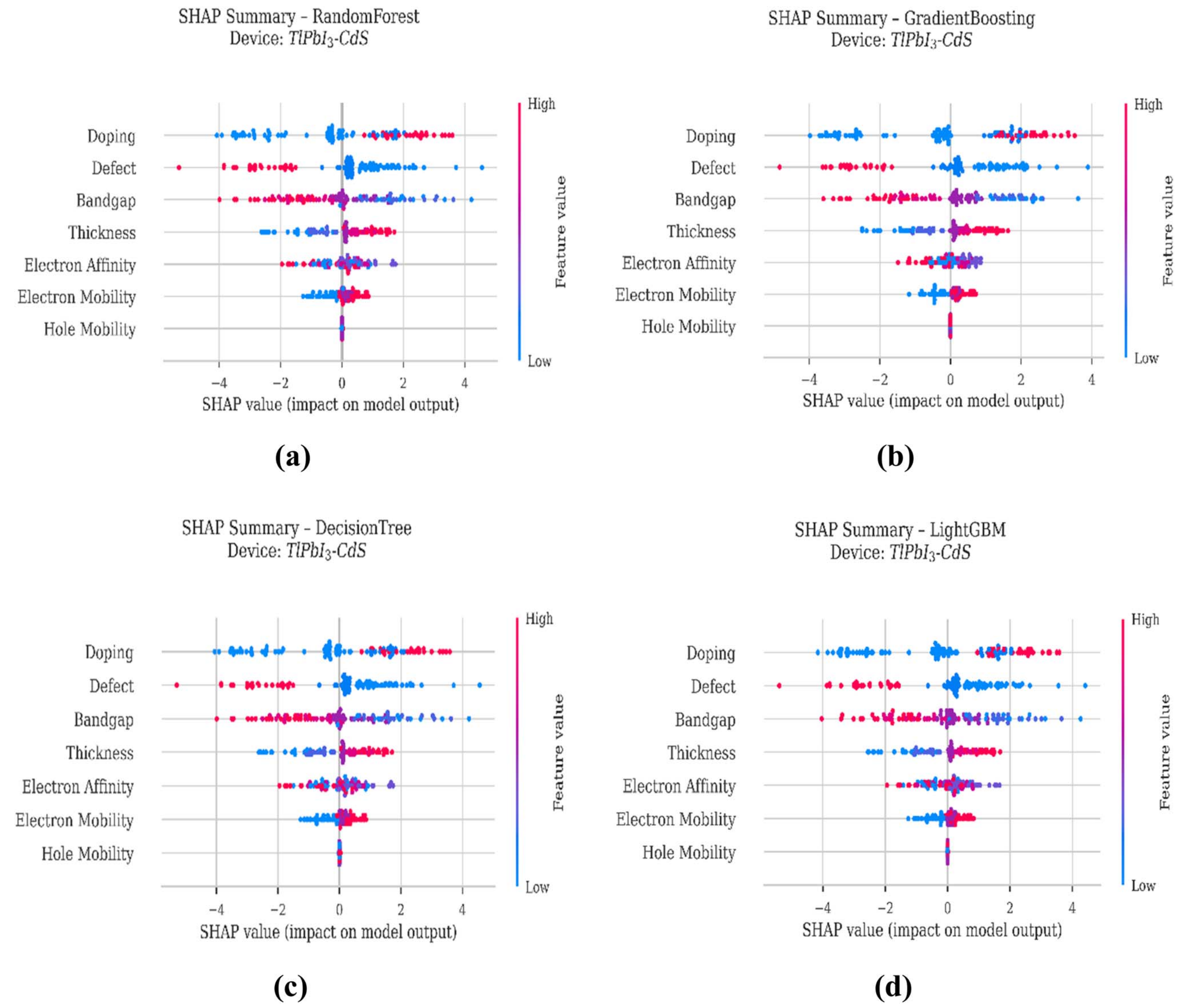

Fig. 18 SHAP summary plots showing different feature impact on pce predictions for (a) random forest, (b) gradient boosting models, (c) decision tree, and (d) lightGBM models for $TlPbI_3$–CdS-based device.

Finally, in Fig. 17, both random forest and decision tree maintain excellent prediction accuracy with a clean diagonal fit. gradient boosting and lightGBM show improved alignment compared to the In_2S_3 device, but still deviate slightly from the ideal line, particularly at extreme PCE values.

Overall, across all devices, random forest and decision tree provide the most precise predictions with minimal error, while gradient boosting and lightGBM display moderate variability. These results suggest that simpler ensemble methods perform more consistently for predicting PCE in $TlPbI_3$-based devices.

3.6.3 SHAP summary plots showing different feature impact on PCE predictions. In this research, SHAP (Shapley Additive Explanations) analysis was employed to interpret the predictive behavior of the models and identify the key factors influencing PV performance. SHAP values provide a transparent and intuitive framework for quantifying the contribution of each feature to the model's output, thereby offering a deeper understanding of how different input parameters drive predictions. By using this approach, the interpretability of the results is significantly enhanced, enabling a clearer explanation of the underlying relationships between material properties and device efficiency.[106] Fig. 18–20 present four SHAP summary plots that explain how different machine learning models interpret the features of the $TlPbI_3$–CdS, $TlPbI_3$–In_2S_3, and $TlPbI_3$–SnS_2 devices, respectively. Each plot represents a specific model—random forest, gradient boosting, decision tree, and lightGBM. The *x*-axis shows the SHAP value, which tells how much each feature influences the model's prediction. The color scale, ranging from blue (low) to red (high), represents the feature value. The features include doping, defect, bandgap, thickness, electron affinity, electron mobility, and hole mobility. The random forest and decision tree models show balanced and stable feature impacts, while gradient boosting

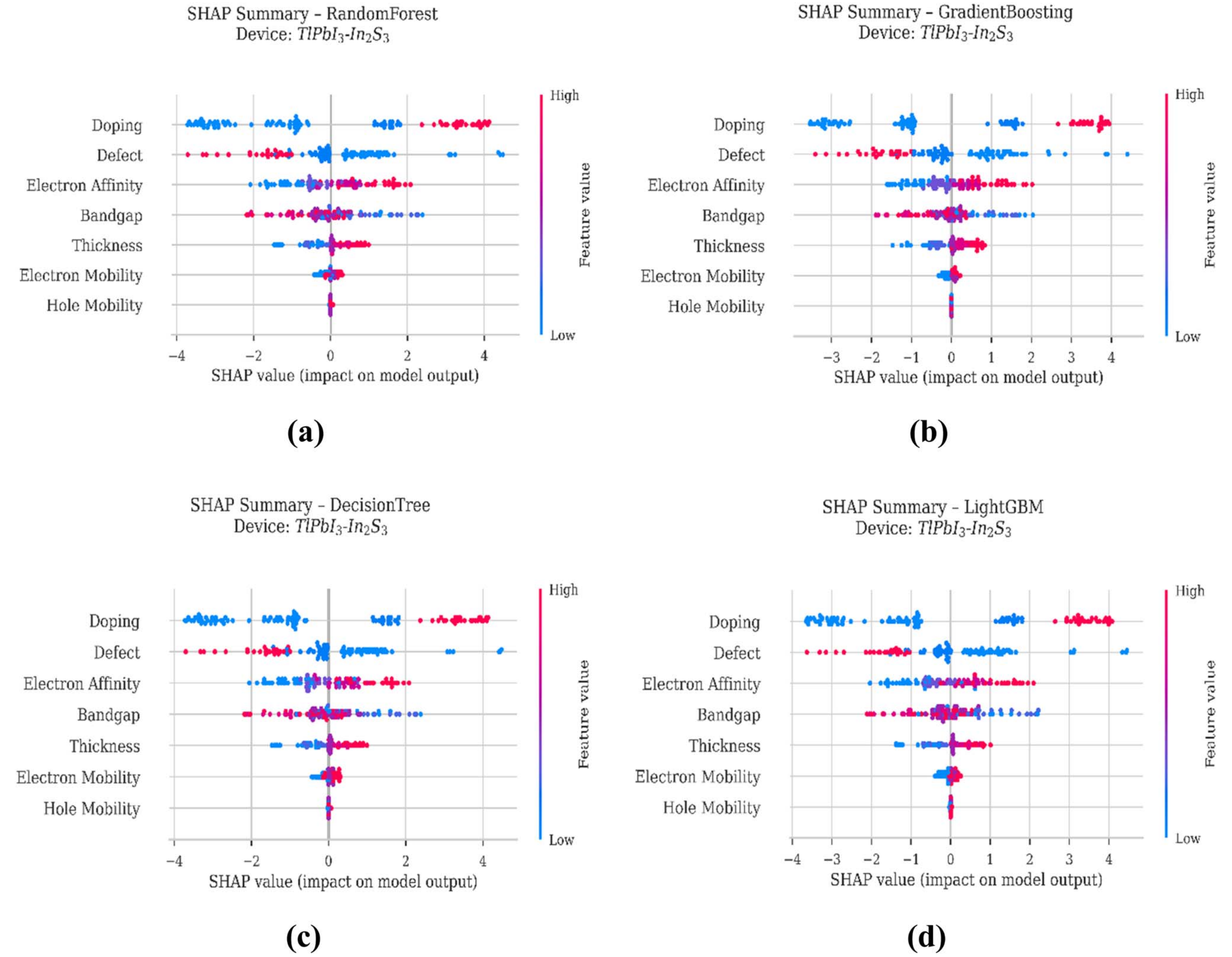

Fig. 19 SHAP summary plots showing different feature impact on PCE predictions for (a) random forest, (b) gradient boosting models, (c) decision tree, and (d) lightGBM models for $TlPbI_3$–In_2S_3-based device.

and lightGBM reveal greater variability, reflecting more complex interactions among the device parameters.

In Fig. 18, among the features, doping, defect, and bandgap show the strongest impact on the model outputs across all four methods. Their wide spread along the *x*-axis means that changes in these features cause larger shifts in predictions. On the other hand, features like hole mobility and thickness have smaller spreads, suggesting they have less influence. The decision tree and random forest plots look more scattered, showing that these models produce a wider range of feature effects. Gradient boosting and lightGBM appear more compact, reflecting their smoother and more stable learning process.

In Fig. 19, the random forest and decision tree models, SHAP values are symmetrically distributed around zero, reflecting stable and interpretable relationships between predictors and outcomes. Gradient boosting and lightGBM show broader SHAP dispersions, suggesting more complex, non-linear dependencies between variables. High doping and bandgap values typically contribute positively to PCE, whereas lower electron affinity and mobility values reduce model output.

For Fig. 20, across all models, doping, defect density, and bandgap exhibit the strongest and most consistent effects on PCE, followed by electron affinity and film thickness. Electron and hole mobility show smaller yet stable contributions. The Random Forest and Decision Tree plots demonstrate balanced distributions around zero, implying stable predictions and interpretability. Gradient Boosting and LightGBM reveal wider spreads in SHAP values, suggesting more complex non-linear effects. High doping and bandgap values positively affect predicted efficiency, while higher defect density and low mobility tend to reduce it.

Overall, these SHAP plots help us see which material properties are most important for predicting the device's behavior. They also show how different models learn and emphasize various aspects of the data, helping researchers understand and improve model performance for the $TlPbI_3$–CdS, $TlPbI_3$–In_2S_3, and $TlPbI_3$–SnS_2 systems.

3.6.4 Comparison of feature importance heatmap across multiple models and devices for PCE prediction. Fig. 21(a–c) provides a comprehensive comparative analysis of how different

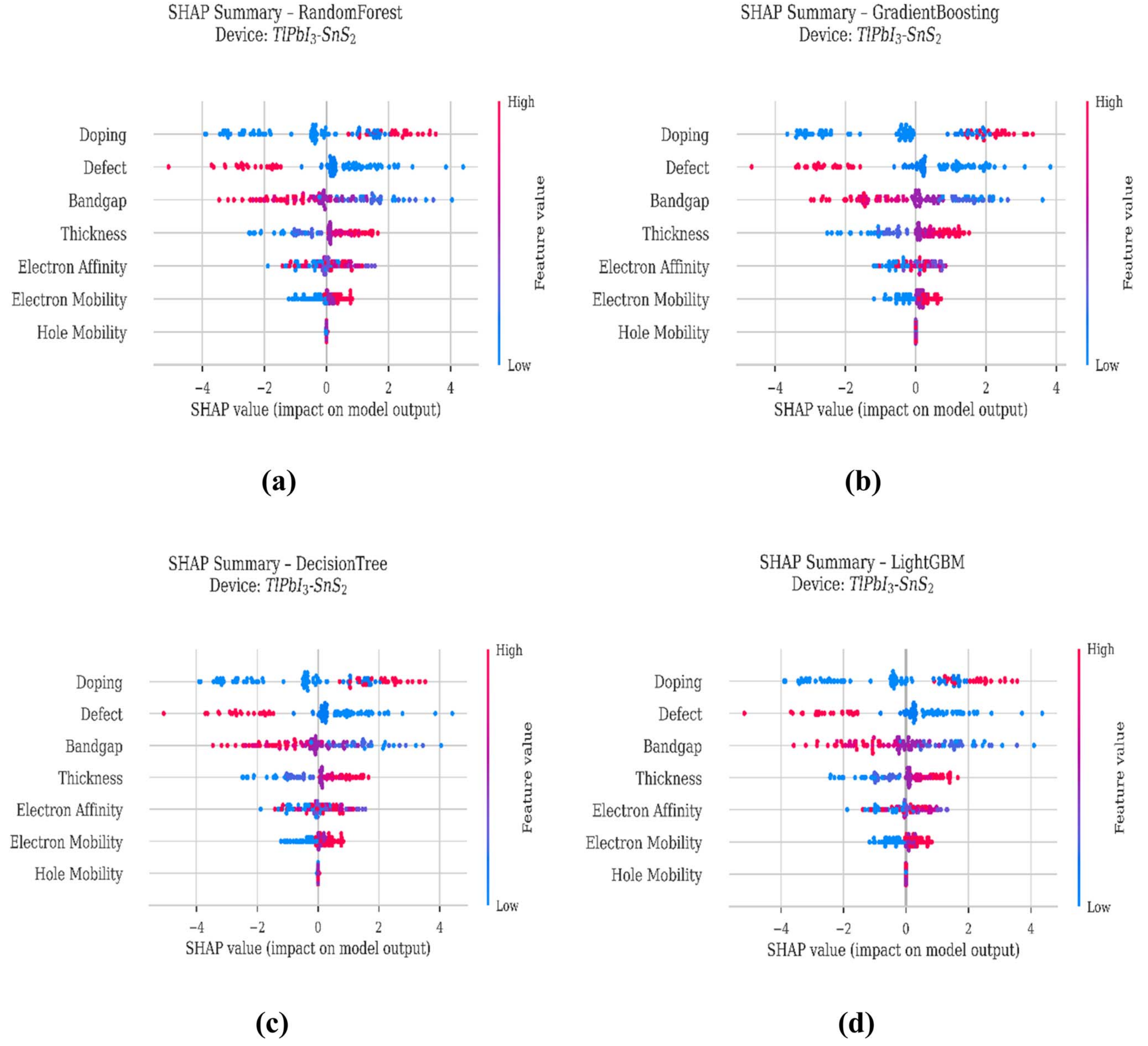

Fig. 20 SHAP summary plots showing different feature impact on PCE predictions for (a) random forest, (b) gradient boosting models, (c) decision tree, and (d) lightGBM models for $TlPbI_3$–SnS_2-based device.

physical and electronic parameters contribute to PCE prediction across four machine learning models and three $TlPbI_3$-based devices—(a) $TlPbI_3$–CdS, (b) $TlPbI_3$–In_2S_3, and (c) $TlPbI_3$–SnS_2. The *x*-axis represents a combination of device types and their corresponding features, such as bandgap, defect, doping, electron affinity, mobility, and thickness, while the *y*-axis lists the four predictive models: random forest, gradient boosting, decision tree, and lightGBM. The color gradient indicates the relative importance of each feature, where darker shades correspond to higher feature influence on the model output.

Across all models and $TlPbI_3$-based devices, doping concentration consistently emerges as the most influential feature, with importance values between 0.43 and 0.46, particularly in the $TlPbI_3$–In_2S_3 system. The dominance underscores doping's critical role in tuning electronic structure and carrier density, directly affecting PCE. Bandgap and defect density follow as key parameters, influencing light absorption and recombination dynamics, while electron affinity, carrier mobilities, and thickness exhibit lower importance, suggesting a more indirect effect on device efficiency. Among the models, random forest and gradient boosting show the highest feature sensitivity and consistency, emphasizing doping, bandgap, and defect density with nearly identical weighting trends. LightGBM distributes feature importance more evenly, while decision tree highlights a narrower set of dominant variables. These variations reflect differences in model learning behavior—ensemble methods capture repetitive predictive features, whereas boosting models focus on cumulative refinement. Overall, the

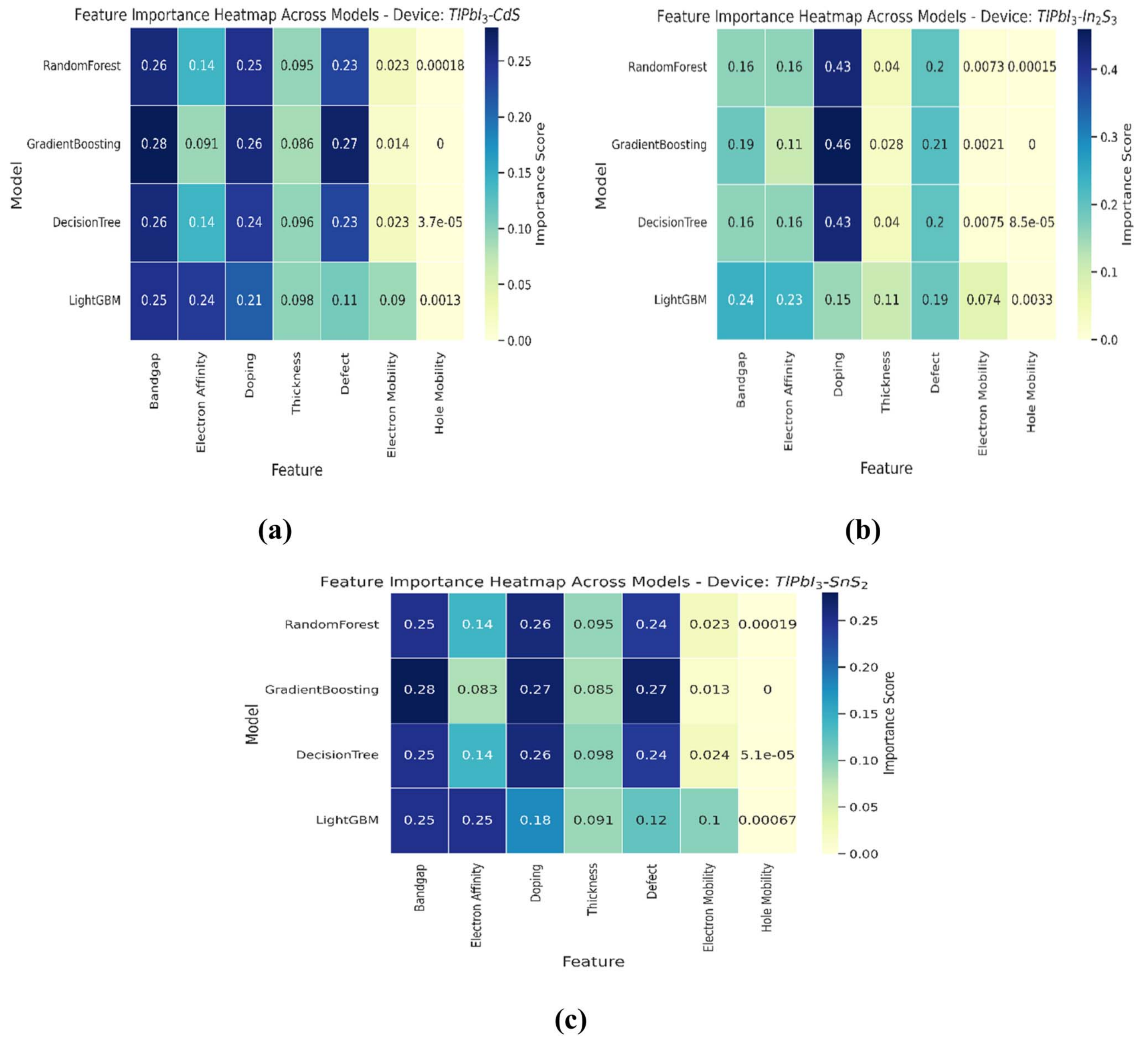

Fig. 21 Comparison of feature importance heatmap from random forest, gradient boosting, decision tree, and lightGBM models for (a) CdS-ETL-based device, (b) In_2S_3-ETL-based device, and (c) SnS_2-ETL-based device.

heatmap confirms that electronic properties—especially doping, bandgap, and defect density—govern PCE prediction accuracy more strongly than structural factors. These findings demonstrate the robustness of tree-based ensemble models in identifying physically meaningful parameters for optimizing $TlPbI_3$-based perovskite solar devices and guiding efficient material design strategies.

In addition to achieving high predictive accuracy, the machine-learning analysis offers insight beyond that obtainable from conventional parameter sweeping. Unlike sweep-based analysis, which mainly reveals trends by varying one parameter at a time, the ML models learn the coupled and nonlinear relationships among multiple device parameters and their collective effect on PCE. The SHAP analysis further strengthens this interpretation by quantifying the relative contribution and directional influence of each feature, thereby highlighting the key physical factors controlling device performance in the investigated $TlPbI_3$-based solar cells. Moreover, the trained models provide a fast predictive platform for estimating performance under new parameter combinations without repeated SCAPS calculations, making device optimization and design-space exploration more efficient.

3.6.5 Environmental and toxicity considerations. Although $TlPbI_3$ exhibits promising structural, optoelectronic, and photovoltaic characteristics, the presence of thallium raises important environmental and safety concerns that must be acknowledged when considering practical application. Thallium is a highly toxic element, and therefore any future experimental development or large-scale deployment of $TlPbI_3$-based solar devices would require strict precautions during material synthesis, device fabrication, handling, and disposal. In particular, robust encapsulation strategies would be essential to minimize the risk of toxic-material leakage during operation or degradation, while appropriate recycling and end-of-life management protocols would be necessary to reduce environmental impact. Accordingly, the present work should be interpreted primarily as a theoretical and simulation-based assessment of the photovoltaic potential of $TlPbI_3$. Its practical feasibility will ultimately depend not only on performance optimization, but also on the development of effective toxicity-control and lifecycle-management strategies.

4 Conclusion

In this comprehensive investigation, we assessed the potential of $TlPbI_3$ as an absorber material for photovoltaic applications by integrating density functional theory, SCAPS-1D simulations, and machine learning. The results collectively demonstrate that $TlPbI_3$ possesses the fundamental material characteristics, device-level performance, and predictive optimization capacity required to position it as a promising candidate for next-generation solar energy conversion. From the structural and mechanical perspective, $TlPbI_3$ crystallizes in a cubic phase with stability confirmed by the satisfaction of Born's criteria. The elastic parameters, bulk modulus of 13.44 GPa, shear modulus of 8.21 GPa, and Young's modulus of 15.91 GPa, point toward a mechanically stable yet ductile material. A Poisson's ratio of 0.30 further indicates metallic bonding contributions, while the predicted melting temperature of 757 K demonstrates sufficient thermal resilience under operational conditions. These properties are advantageous for scalable thin-film growth and long-term device durability. The electronic properties reveal a direct band gap of 1.26 eV at the Γ point, placing $TlPbI_3$ within the Shockley–Queisser optimal range for single-junction solar cells. Orbital-resolved density of states indicates that electronic transport is primarily governed by the hybridization between I-5p states in the valence band and Tl-6p states in the conduction band, complemented by Pb–I covalent interactions. The charge density distribution confirms the coexistence of ionic Tl–I and covalent Pb–I bonds, which not only strengthen lattice stability but also enhance carrier delocalization, thereby improving transport properties. The optical analysis provides strong evidence of $TlPbI_3$'s suitability as a solar absorber. Its high absorption coefficient in the visible region, low reflectivity, and static dielectric constant of ~4.6 suggest efficient photon harvesting and reduced recombination. The calculated refractive index also supports strong light–matter interactions, which are critical for maximizing current output in thin-film devices. The SCAPS-1D device simulations provided crucial insights into the practical potential of $TlPbI_3$ in heterojunction solar cell configurations. Among the simulated devices, the FTO/CdS/$TlPbI_3$/Cu structure demonstrated the best performance with a PCE of 22.20% ($V_{OC} = 0.7987$ V, $J_{SC} = 34.56$ mA cm^{-2}, FF = 80.40%). The FTO/SnS_2/$TlPbI_3$/Cu configuration also achieved a high efficiency of 21.34% ($V_{OC} = 0.7941$ V, $J_{SC} = 34.57$ mA cm^{-2}, FF = 77.74%). In contrast, the FTO/In_2S_3/$TlPbI_3$/Cu device yielded a lower efficiency of 9.47% ($V_{OC} = 0.5626$ V, $J_{SC} = 34.46$ mA cm^{-2}, FF = 48.86%), indicating less favorable band alignment and interface properties with In_2S_3. These results clearly demonstrate that careful selection of buffer and electron transport layers plays a decisive role in optimizing device performance. Finally, the incorporation of machine learning into the study provided predictive capability beyond conventional simulations. The ML models confirmed absorber thickness and defect concentration as the dominant parameters influencing efficiency and enabled rapid screening of design configurations. This demonstrates the added value of data-driven approaches in accelerating the materials discovery process.

Author contributions

Md. Harun-Or-Rashid: conceptualization, methodology, resources, software, validation, investigation, data curation, formal analysis, visualization, writing – original draft, writing – review & editing, supervision, project administration, funding acquisition. Hanane Etabti, Md. Tauki Tazwar: software, investigation, data curation, visualization, validation, writing – original draft, writing – review & editing. Md Amzad Sadik Abid: software, validation, formal analysis, resources, writing – review & editing. Md Farhan Shahriyar: software, validation, visualization, writing – original draft, writing – review & editing. Nosir Khurramov, Hayitov Abdulla Nurmatovich, Sardor Sabirov: validation, formal analysis, resources, writing – review & editing. Lakhdar Benahmedi: software, validation, writing – original draft, writing – review & editing. Md. Monirul Islam: software, validation, formal analysis, writing – original draft, writing – review & editing. Md. Ferdous Rahman: supervision, validation, resources, writing – review & editing.

Conflicts of interest

The authors have no conflicts of interest.

Data availability

The data that support the findings of this study are available from the corresponding author upon reasonable request.

Supplementary information (SI) is available. See DOI: https://doi.org/10.1039/d6ra01288d.

Acknowledgements

This research was supported by the National Science and Technology (NST) Fellowship, Ministry of Science and Technology, Government of the People's Republic of Bangladesh. The authors sincerely acknowledge Dr Marc Burgelman and the EIS group at Ghent University for providing access to the SCAPS-1D simulation software. They also extend their gratitude to the Quantum ESPRESSO Foundation (QEF) for offering the open-source Quantum ESPRESSO package used in this research.

References

1 G. Semieniuk, L. Taylor, A. Rezai and D. K. Foley, Plausible energy demand patterns in a growing global economy with climate policy, *Nat. Clim. Chang.*, 2021, **11**(4), 313–318, DOI: 10.1038/s41558-020-00975-7.

2 J. Szlufcik, S. Sivoththaman, J. F. Nlis, R. P. Mertens and R. Van Overstraeten, Low-cost industrial technologies of crystalline silicon solar cells, *Proc. IEEE*, 1997, **85**(5), 711–730, DOI: 10.1109/5.588971.

3 C. Ballif, F.-J. Haug, M. Boccard, P. J. Verlinden and G. Hahn, Status and perspectives of crystalline silicon photovoltaics in research and industry, *Nat. Rev. Mater.*, 2022, **7**(8), 597–616, DOI: 10.1038/s41578-022-00423-2.

4 S. M. Sivasankar and C. D. O. Amorim, *Progress in Thin-Film Photovoltaics : A Review of Key Strategies to Enhance the Efficiency of CIGS , CdTe , and CZTSSe Solar Cells*, 2025.

5 L. Benahmedi, A. Besbes, R. Djelti, S. Bendehiba and A. Aissani, First-principles investigation of structural, electronic, optical, elastic, and thermoelectric properties of cubic francifluorite perovskites FrXF3 (X = Si, Ge, and Sn) for optoelectronic and thermoelectric applications, *Phys. Scr.*, 2024, **99**(12), 125979, DOI: 10.1088/1402-4896/ad9225.

6 R. Okumura, T. Oku and A. Suzuki, Electronic structures of ABX3 perovskite crystals with a monovalent copper ion as the A-site cation, *Chem. Phys. Impact*, 2024, **8**, 100534, DOI: 10.1016/j.chphi.2024.100534.

7 L. Benahmedi, A. Besbes, R. Djelti, S. Moulebhar, A. Aissani and S. Bendehiba, Theoretical insights into Rb2Pt1-xPdxBr6 perovskite alloys for solar Cells: A combined DFT and SCAPS-1D study, *Sol. Energy*, 2025, **300**, DOI: 10.1016/j.solener.2025.113860.

8 M. Elhadi, *et al.*, Optimization and Comparative Analysis of Electron Transport Layers for High-Performance InGeCl3-Based Perovskite Solar Cells, *ChemistrySelect*, 2025, **10**(26), 1–18, DOI: 10.1002/slct.202501364.

9 F. Huang, M. Li, P. Siffalovic, G. Cao and J. Tian, From scalable solution fabrication of perovskite films towards commercialization of solar cells, *Energy Environ. Sci.*, 2019, **12**(2), 518–549, DOI: 10.1039/C8EE03025A.

10 P. Wang, Y. Wu, B. Cai, Q. Ma, X. Zheng and W.-H. Zhang, Solution-Processable Perovskite Solar Cells toward Commercialization: Progress and Challenges, *Adv. Funct. Mater.*, 2019, **29**(47), 1807661, DOI: 10.1002/adfm.201807661.

11 A. Kojima, K. Teshima, Y. Shirai and T. Miyasaka, Organometal halide perovskites as visible-light sensitizers for photovoltaic cells, *J. Am. Chem. Soc.*, 2009, **131**(17), 6050–6051, DOI: 10.1021/ja809598r.

12 D. Zhou, T. Zhou, Y. Tian, X. Zhu and Y. Tu, Perovskite-Based Solar Cells: Materials, Methods, and Future Perspectives, *J. Nanomater.*, 2018, **2018**(1), 8148072, DOI: 10.1155/2018/8148072.

13 Y. H. Park, *et al.*, Solar Cells: Inorganic Rubidium Cation as an Enhancer for Photovoltaic Performance and Moisture Stability of HC(NH2)2PbI3 Perovskite Solar Cells (Adv. Funct. Mater. 16/2017), *Adv. Funct. Mater.*, 2017, **27**(16), DOI: 10.1002/adfm.201770096.

14 H. J. Snaith, Perovskites: The Emergence of a New Era for Low-Cost, High-Efficiency Solar Cells, *J. Phys. Chem. Lett.*, 2013, **4**(21), 3623–3630, DOI: 10.1021/jz4020162.

15 M. A. Green, K. Emery, Y. Hishikawa, W. Warta and E. D. Dunlop, Solar cell efficiency tables (version 41), *Prog. Photovoltaics Res. Appl.*, 2013, **21**(1), 1–11, DOI: 10.1002/pip.2352.

16 R. Jacobs, G. Luo and D. Morgan, Materials Discovery of Stable and Nontoxic Halide Perovskite Materials for High-Efficiency Solar Cells, *Adv. Funct. Mater.*, 2019, **29**(23), 1804354–Jun, DOI: 10.1002/adfm.201804354.

17 J. Li, B. Pradhan, S. Gaur and J. Thomas, Predictions and Strategies Learned from Machine Learning to Develop High-Performing Perovskite Solar Cells, *Adv. Energy Mater.*, 2019, **9**(46), 1901891, DOI: 10.1002/aenm.201901891.

18 S. A. Kulkarni, N. Yantara, K. S. Tan, N. Mathews and S. G. Mhaisalkar, Perovskite nanostructures: Leveraging quantum effects to challenge optoelectronic limits, *Mater. Today*, 2020, **33**, 122–140, DOI: 10.1016/j.mattod.2019.10.021.

19 J. J. Yoo, *et al.*, Efficient perovskite solar cells via improved carrier management, *Nature*, 2021, **590**(7847), 587–593, DOI: 10.1038/s41586-021-03285-w.

20 N. J. Jeon, J. H. Noh, Y. C. Kim, W. S. Yang, S. Ryu and S. Il Seok, Solvent engineering for high-performance inorganic–organic hybrid perovskite solar cells, *Nat. Mater.*, 2014, **13**(9), 897–903, DOI: 10.1038/nmat4014.

21 J. Duan, *et al.*, Improved 3D–2D Perovskite for Efficient Perovskite Photovoltaics with Low-Temperature Carbon Electrodes, *ACS Omega*, 2024, **9**(1), 642–650, DOI: 10.1021/acsomega.3c06322.

22 Z. Liu *et al.*, *Electronic Properties of a New All-Inorganic Perovskite TlPbI 3 Simulated by the First Principles*, 2017, DOI: 10.1186/s11671-017-2015-y.

23 W. Lin, *et al.*, Inorganic Halide Perovskitoid TlPbI3 for Ionizing Radiation Detection, *Adv. Funct. Mater.*, 2021, **31**(13), 2006635, DOI: 10.1002/adfm.202006635.

24 Y. Yan, *et al.*, Evaluation of the electronic properties of layered TlPbI3 perovskites, *Phys. B Condens. Matter*, 2023, **667**, 415190, DOI: 10.1016/j.physb.2023.415190.

25 S. Moulebhar, C. Bendenia, H. Merad-Dib, S. Bendenia, S. Merabet and S. A. Khantar, Hybrid Optimization Approach Using Multiobjective Genetic Algorithm NSGA-II, SCAPS-1D Simulation, and Response Surface Methodology for Organic Solar Cell Analysis, *Phys. status solidi*, 2025, **222**(2), 2400654, DOI: 10.1002/pssa.202400654.

26 S. Moulebhar, C. Bendenia, S. Bendenia, H. Merad-Dib, S. A. Khantar and S. Merabet, Enhancing Organic Solar Cells through Dual Electron Transport Layers: A Machine Learning Approach for Prediction of Organic and Metal Oxide Electron Transport Layer Compatibility, *Phys. status solidi*, 2025, **222**(15), 2500317, DOI: 10.1002/pssa.202500317.

27 J. P. Perdew, K. Burke, and M. Ernzerhof, *Generalized Gradient Approximation Made Simple*, 1996.

28 J. M. Smith, S. P. Jones and L. D. White, Rapid Communication, *Gastroenterology*, 1977, **72**(1), 193, DOI: 10.1016/S0016-5085(77)80340-5.

29 D. R. Hamann, M. Schlüter and C. Chiang, Norm-Conserving Pseudopotentials, *Phys. Rev. Lett.*, 1979, **43**(20), 1494–1497, DOI: 10.1103/PhysRevLett.43.1494.

30 G. Kresse and J. Hafner, Norm-conserving and ultrasoft pseudopotentials for first-row and transition elements, *J. Phys. Condens. Matter*, 1994, **6**(40), 8245–8257, DOI: 10.1088/0953-8984/6/40/015.

31 P. Giannozzi, *et al.*, QUANTUM ESPRESSO: A modular and open-source software project for quantum simulations of materials, *J. Phys. Condens. Matter*, 2009, **21**(39), DOI: 10.1088/0953-8984/21/39/395502.

32 A. Niemegeers and M. Burgelman, *Modelling of ac-Characteristics Solar Cells*, IEEE Photovoltaics Spec. Conf., 1996, pp. 901–904.

33 M. Burgelman, P. Nollet and S. Degrave, Modelling polycrystalline semiconductor solar cells, *Thin Solid Films*, 2000, **361–362**, 527–532, DOI: 10.1016/S0040-6090(99)00825-1.

34 S. M. Seyed-Talebi, M. Mahmoudi and C. H. Lee, A Comprehensive Study of CsSnI3-Based Perovskite Solar Cells with Different Hole Transporting Layers and Back Contacts, *Micromachines*, 2023, **14**(8), DOI: 10.3390/mi14081562.

35 V. C. Karade, *et al.*, Unraveling the Effect of Compositional Ratios on the Kesterite Thin-Film Solar Cells Using Machine Learning Techniques, *Crystals*, 2023, **13**(11), 1–10, DOI: 10.3390/cryst13111581.

36 A. Ghosh, A. A. Hassan, H. A. Alrafai and S. K. A. Abdelrahim, A comprehensive study on electron and hole transport layers for designing and optimizing the efficiency of MoSe2-Based solar cells using numerical simulation techniques, *Heliyon*, 2024, **10**(16), e35061, DOI: 10.1016/j.heliyon.2024.e35061.

37 Y. He, L. Xu, C. Yang, X. Guo and S. Li, Design and numerical investigation of a lead-free inorganic layered double perovskite cs4cusb2cl12 nanocrystal solar cell by scaps-1d, *Nanomaterials*, 2021, **11**(9), 1–19, DOI: 10.3390/nano11092321.

38 M. K. Hossain, *et al.*, An extensive study on multiple ETL and HTL layers to design and simulation of high-performance lead-free CsSnCl3-based perovskite solar cells, *Sci. Rep.*, 2023, **13**(1), 1–24, DOI: 10.1038/s41598-023-28506-2.

39 M. F. Rahman, A. Lubaba, L. Ben Farhat, S. Ezzine, M. H. Rahman and M. Harun-Or-Rashid, Efficiency enhancement above 31 % of Sb2Se3 solar cells with optimizing various BSF layer, *Mater. Sci. Eng. B*, 2024, **307**, DOI: 10.1016/j.mseb.2024.117527.

40 B. Sultana, *et al.*, A new design and optimization of SnSe-based dual absorber solar cell with efficiency above 28%, *J. Nanoparticle Res.*, 2024, **26**(8), 181, DOI: 10.1007/s11051-024-06085-1.

41 M. F. Wahid, *et al.*, Performance Enhancement of Lead-Free CsSnI3 Perovskite Solar Cell: Design and Simulation With Different Electron Transport Layers, *IEEE Access*, 2024, **12**(December 2023), 8296–8312, DOI: 10.1109/ACCESS.2024.3352444.

42 Z. Jin, J. Shang, Q. Zhu, C. Ling, W. Xie and B. Qiang, RFRSF: Employee Turnover Prediction Based on Random Forests and Survival Analysis, *Lect. Notes Comput. Sci.*, 2020, **12343**(LNCS), 503–515, DOI: 10.1007/978-3-030-62008-0_35.

43 A. Natekin and A. Knoll, Gradient boosting machines, a tutorial, *Front. Neurorobot.*, 2013, **7**, DOI: 10.3389/fnbot.2013.00021.

44 C. Qi, E. Yilmaz, and Q. Chen, 6 – Background of machine learning, in *Woodhead Publishing Series in Civil and Structural Engineering*, C. Qi, E. Yilmaz, Q. B. T.-M. L. A., and I. S. A. Chen, Elsevier, 2024, pp. 93–130,DOI: 10.1016/B978-0-443-15524-6.00015-7.

45 A. Ampountolas and S. AlGharbi, An innovative hybrid LightGBM-BPNN model for enhanced commodity forecasting accuracy, *Financ. Res. Open*, 2025, **1**(1), 100004, DOI: 10.1016/j.finr.2025.100004.

46 M. Elhadi *et al.*, Optimization and Comparative Analysis of Electron Transport Layers for High-Performance InGeCl 3 -Based Perovskite Solar, 2025, vol. **01364**, pp. 1–18, DOI: 10.1002/slct.202501364.

47 W. Travis, E. N. K. Glover, H. Bronstein, D. O. Scanlon and R. G. Palgrave, On the application of the tolerance factor to inorganic and hybrid halide perovskites: A revised system, *Chem. Sci.*, 2016, **7**(7), 4548–4556, DOI: 10.1039/c5sc04845a.

48 G. Han, *et al.*, Additive Selection Strategy for High Performance Perovskite Photovoltaics, *J. Phys. Chem. C*, 2018, **122**(25), 13884–13893, DOI: 10.1021/acs.jpcc.8b00980.

49 P. Bhumla, M. Jain, S. Sheoran and S. Bhattacharya, Vacancy-Ordered Double Perovskites Cs2BI6 (B = Pt, Pd, Te, Sn): An Emerging Class of Thermoelectric Materials, *J. Phys. Chem. Lett.*, 2022, **13**(50), 11655–11662, DOI: 10.1021/acs.jpclett.2c02852.

50 M. Jain, D. Gill, S. Monga and S. Bhattacharya, Oxynitride, Oxyfluoride, and Nitrofluoride Perovskites: Theoretical Evaluation of Photon Absorption Properties for Solar Water Splitting, *J. Phys. Chem. C*, 2023, **127**(31), 15620–15629, DOI: 10.1021/acs.jpcc.3c03449.

51 M. F. Rahman, *et al.*, A Deep Analysis and Enhancing Photovoltaic Performance Above 31% with New Inorganic RbPbI 3 -Based Perovskite Solar Cells via DFT and SCAPS-1D, *Adv. Theory Simulations*, 2024, **2400476**, 1–12, DOI: 10.1002/adts.202400476.

52 M. Harun-Or-Rashid, M. F. Rahman, M. Amami, L. Ben Farhat, M. M. Islam and A. Benami, Exploring new lead-free halide perovskites RbSnM3 (M = I, Br, Cl) and achieving power conversion efficiency > 32 %,, *J. Phys. Chem. Solids*, 2025, **197**(221), 112437, DOI: 10.1016/j.jpcs.2024.112437.

53 A. Ba, H. O. Rashid, L. Ben Farhat, A. Brahmia and M. K. A. Mohammed, Analysis of the role of A - cations in

lead - free -, *J. Mater. Sci.*, 2024, **3**, 0123456789, DOI: 10.1007/s10853-024-09579-4.

54 R. K. Pingak, *et al.*, Lead-free perovskites InSnX3 (X = Cl, Br, I) for solar cell applications: a DFT study on the mechanical, optoelectronic, and thermoelectric properties, *Mater. Res. Express*, 2023, **10**(9), 95507, DOI: 10.1088/2053-1591/acf984.

55 D. Abdullah and D. C. Gupta, Analyzing the structural, optoelectronic, and thermoelectric properties of InGeX3 (X = Br) perovskites via DFT computations, *Sci. Rep.*, 2024, **14**(1), 23575, DOI: 10.1038/s41598-024-72745-w.

56 A. Nazir, E. Ahmad Khera, M. Manzoor, B. Ali Al-Asbahi, Y. Anil Kumar and R. Sharma, A density functional theory study of the structural, mechanical, optoelectronics and thermoelectric properties of InGeX3 (X = F, Cl) perovskites, *Polyhedron*, 2024, **257**, DOI: 10.1016/j.poly.2024.117009.

57 M. Harun-Or-Rashid, *et al.*, High-efficiency InPbI3 perovskite solar cells: A multiscale approach from first-principles to machine learning, *Mater. Today Commun.*, 2025, **49**, 114060, DOI: 10.1016/j.mtcomm.2025.114060.

58 M. Harun-Or-Rashid, *et al.*, Unveiling the potential of GaPbI3 perovskite: Structural, mechanical, and optoelectronic insights for next-generation solar cells, *Mater. Today Commun.*, 2025, **42**, 111490, DOI: 10.1016/j.mtcomm.2025.111490.

59 J. Chen, *et al.*, Structural, mechanical and optoelectronic properties of perovskites XPbI3 (X = Al, Ga, In, Tl) for photovoltaic applications based on density functional theory, *Phys. Scr.*, 2025, **100**(6), 65903, DOI: 10.1088/1402-4896/adcfd8.

60 M. Harun-Or-Rashid, *et al.*, Unveiling the potential of GaPbI3 perovskite: Structural, mechanical, and optoelectronic insights for next-generation solar cells, *Mater. Today Commun.*, 2025, **42**, 111490, DOI: 10.1016/j.mtcomm.2025.111490.

61 M. R. Islam, *et al.*, Strain-induced tunability of the optoelectronic properties of inorganic lead iodide perovskites APbI3 (A= Rb and Cs), *Phys. B Condens. Matter*, 2022, **638**, 413960, DOI: 10.1016/j.physb.2022.413960.

62 A. Nazir, E. Ahmad Khera, M. Manzoor, B. Ali Al-Asbahi, Y. Anil Kumar and R. Sharma, A density functional theory study of the structural, mechanical, optoelectronics and thermoelectric properties of InGeX3 (X = F, Cl) perovskites, *Polyhedron*, 2024, **257**, 117009, DOI: 10.1016/j.poly.2024.117009.

63 D. Islam, *et al.*, High-efficiency InPbI 3 perovskite solar cells : A multiscale approach from first-principles to machine learning, *Mater. Today Commun.*, 2025, **49**, 114060, DOI: 10.1016/j.mtcomm.2025.114060.

64 D. Abdullah and D. C. Gupta, Investigation of Structural, Electronic, Optical, and Elastic Properties of Ru-Based Inorganic Halide Perovskites ARuBr3 (A = K, Rb, Cs) *via* DFT Computations, *Arab. J. Sci. Eng.*, 2025, **50**(9), 6823–6833, DOI: 10.1007/s13369-024-09524-2.

65 B. Ghebouli, *et al.*, Theoretical prediction of the structural, elastic, electronic, optical and thermal properties of the cubic perovskites CsXF3 (X = Ca, Sr and Hg) under pressure effect, *Solid State Sci.*, 2012, **14**(7), 903–913, DOI: 10.1016/j.solidstatesciences.2012.04.019.

66 M. Jawad, A. U. Rahman, S. H. Mirza, S. Azam, N. ul Amin and A. Shakoor, Comprehensive analysis of the effect of Na doping concentration on the essential physical properties of K2PdO2: A first principle study, *Phys. B Condens. Matter*, 2025, **700**, 416925, DOI: 10.1016/j.physb.2025.416925.

67 A. Shakoor, *et al.*, DFT investigation of structural, electronic, optical, mechanical, and thermoelectric properties of halide perovskites XZnCl3(X = Ag, Au, Cu), *Phys. B Condens. Matter*, 2025, **712**, 417309, DOI: 10.1016/j.physb.2025.417309.

68 A. G, A. V, M. M. S. Sirajuddeen and A. Alam, Theoretical investigation of structural, electronic, elastic, and optical properties of rubidium-based perovskites RbSrX3 (X = Cl, Br) for optoelectronic device applications – A DFT study, *Phys. B Condens. Matter*, 2024, **682**, 415858, DOI: 10.1016/j.physb.2024.415858.

69 X. X. Li and N. Dft, *Nanoscale Advances Mechanical Stability and Optoelectronic Properties of Alkali-Based Single Halide Perovskite Compounds*, 2024, pp. 4479–4491, DOI: 10.1039/d4na00305e.

70 M. A. Ali, A. A. A. Bahajjaj, S. Al-Qaisi, M. Sillanpää, A. Khan and X. Wang, Structural, electronic, magnetic and thermoelectric properties of Tl2NbX6 (X = Cl, Br) variant perovskites calculated via density functional theory, *J. Comput. Chem.*, 2023, **44**(23), 1875–1883, DOI: 10.1002/jcc.27166.

71 M. A. Ali, *et al.*, Spin-based transport properties of Cs2WX6 (X = Cl, Br) ferromagnets for spin-injected thermoelectric current, *Eur. Phys. J. Plus*, 2021, **136**(5), 568, DOI: 10.1140/epjp/s13360-021-01554-1.

72 W.-J. Yin, J.-H. Yang, J. Kang, Y. Yan and S.-H. Wei, Halide perovskite materials for solar cells: a theoretical review, *J. Mater. Chem. A*, 2015, **3**(17), 8926–8942, DOI: 10.1039/C4TA05033A.

73 D.-Y. Chen, *et al.*, Superconducting properties in a candidate topological nodal line semimetal ${\mathrm {SnTaS}}_{2}$ with a centrosymmetric crystal structure, *Phys. Rev. B*, 2019, **100**(6), 64516, DOI: 10.1103/PhysRevB.100.064516.

74 A. Islam, B. Chandra, A. Ghosh and N. S. Awwad, Materials Science & Engineering B Performance assessment and machine learning-driven optimization of Ca 3 NBr 3 -based bifacial perovskite solar cells : improving V OC *via* HTL and charge transport layer analysis, *Mater. Sci. Eng. B*, 2025, **322**(June), 118600, DOI: 10.1016/j.mseb.2025.118600.

75 M. A. Fadla, B. Bentria, T. Dahame and A. Benghia, First-principles investigation on the stability and material properties of all-inorganic cesium lead iodide perovskites CsPbI3 polymorphs, *Phys. B Condens. Matter*, 2020, **585**, 412118, DOI: 10.1016/j.physb.2020.412118.

76 P. Sharma, P. Ranjan and T. Chakraborty, Study of Tl-based perovskite materials TlZX3 (Z = Ge, Sn, Be, Sr; X = Cl, Br, I)

for application in scintillators: DFT and TD-DFT approach, *Chem. Phys. Impact*, 2023, **7**, 100344, DOI: 10.1016/j.chphi.2023.100344.

77 M. W. Iqbal, *et al.*, DFT insights on the opto-electronic and thermoelectric properties of double perovskites K2AgSbX6 (X = Cl, Br) via halides substitutions for solar cell applications, *Mater. Sci. Eng. B*, 2023, **290**, 116338, DOI: 10.1016/j.mseb.2023.116338.

78 S. A. Khandy and D. C. Gupta, Intrinsic magnetism and thermoelectric applicability of novel halide perovskites Cs2GeMnX6 (X = Cl, Br): Route towards spintronics and energy harvesting technologies, *Mater. Sci. Eng. B*, 2021, **265**, 114985, DOI: 10.1016/j.mseb.2020.114985.

79 S. Bouhmaidi, A. Harbi, R. K. Pingak, A. Azouaoui, M. Moutaabbid and L. Setti, First-principles calculations to investigate lead-free double perovskites CsInSbAgX6 (X = Cl, Br and I) for optoelectronic and thermoelectric applications, *Comput. Theor. Chem.*, 2023, **1227**, 114251, DOI: 10.1016/j.comptc.2023.114251.

80 R. K. Pingak, *et al.*, A DFT investigation of lead-free TlSnX3 (X = Cl, Br, or I) perovskites for potential applications in solar cells and thermoelectric devices, *RSC Adv.*, 2023, **13**(48), 33875–33886, DOI: 10.1039/d3ra06685a.

81 M. Z. Rahaman, M. A. Rahman and M. A. R. Sarker, Prediction of a new transition metal oxide MgRhO3 with SrTiO3-type structure: Stability, structure and physical characteristics, *Chinese J. Phys.*, 2017, **55**(4), 1489–1494, DOI: 10.1016/j.cjph.2017.03.021.

82 M. A. Ali, *et al.*, A theoretical study of the structural, thermoelectric, and spin-orbit coupling influenced optoelectronic properties of CsTmCl3 halide perovskite, *Int. J. Quantum Chem.*, 2019, **120**, DOI: 10.1002/qua.26141.

83 M. A. Ali, *et al.*, Insight into pressure tunable structural, electronic and optical properties of *via* DFT calculations, *Eur. Phys. J. Plus*, 2020, **135**(3), 309, DOI: 10.1140/epjp/s13360-020-00325-8.

84 X. Liu, *et al.*, A high dielectric constant non-fullerene acceptor for efficient bulk-heterojunction organic solar cells, *J. Mater. Chem. A*, 2018, **6**(2), 395–403, DOI: 10.1039/C7TA10136H.

85 S. Saha, T. P. Sinha and A. Mookerjee, Electronic structure, chemical bonding, and optical properties of paraelectric BaTiO3, *Phys. Rev. B*, 2000, **62**(13), 8828–8834.

86 M. Ud Din, J. Munir, M. Jamil, M. A. Saeed and Q. Ain, Electronic structure and optical response of double perovskite Rb2NaCoF6 for optoelectronic devices, *Phys. B Condens. Matter*, 2022, **627**, 413533, DOI: 10.1016/j.physb.2021.413533.

87 M. M. Rahaman, *et al.*, Mechanical, electronic, optical, and thermodynamic properties of orthorhonmbic LiCuBiO4 crystal: a first–priciples study, *J. Mater. Res. Technol.*, 2019, **8**(5), 3783–3794, DOI: 10.1016/j.jmrt.2019.06.039.

88 M. Roknuzzaman, K. (Ken) Ostrikov, K. Chandula Wasalathilake, C. Yan, H. Wang and T. Tesfamichael, Insight into lead-free organic-inorganic hybrid perovskites for photovoltaics and optoelectronics: A first-principles study, *Org. Electron.*, 2018, **59**, 99–106, DOI: 10.1016/j.orgel.2018.04.051.

89 A. Ghosh, *et al.*, Improving the performance of AgCdF 3 -based perovskite solar cells using machine learning-driven adjustment of active layer and charge transport materials with SCAPS-1D, *Inorg. Chem. Commun.*, 2025, **179**(P2), 114829, DOI: 10.1016/j.inoche.2025.114829.

90 L. Et-Taya, A. Benami and T. Ouslimane, Study of CZTSSe-Based Solar Cells with Different ETMs by SCAPS, *Sustain*, 2022, **14**(3), DOI: 10.3390/su14031916.

91 M. A. H. Pappu, S. N. Shiddique, B. K. Mondal, M. I. R. Ebon, T. Ahmed and J. Hossain, Numerical simulation on an efficient n-CdS/p-ZnSnN2/p+-Cu2SnS3/p++- CuGaSe2 thin film solar cell, *Mater. Today Commun.*, 2024, **38**, DOI: 10.1016/j.mtcomm.2024.108474.

92 A. Ghosh, A. A. Hassan, H. A. Alrafai and S. K. A. Abdelrahim, A comprehensive study on electron and hole transport layers for designing and optimizing the efficiency of MoSe2-Based solar cells using numerical simulation techniques, *Heliyon*, 2024, **10**(16), e35061, DOI: 10.1016/j.heliyon.2024.e35061.

93 M. S. Reza, *et al.*, Design and Optimization of High-Performance Novel RbPbBr3-Based Solar Cells with Wide-Band-Gap S-Chalcogenide Electron Transport Layers (ETLs), *ACS Omega*, 2024, **9**(18), 19824–19836, DOI: 10.1021/acsomega.3c08285.

94 M. F. Rahman, *et al.*, A Deep Analysis and Enhancing Photovoltaic Performance Above 31% with New Inorganic RbPbI3-Based Perovskite Solar Cells via DFT and SCAPS-1D, *Adv. Theory Simulations*, 2024, **7**(10), 2400476, DOI: 10.1002/adts.202400476.

95 M. S. Reza, *et al.*, Boosting efficiency above 28% using effective charge transport layer with Sr3SbI3 based novel inorganic perovskite, *RSC Adv.*, 2023, **13**(45), 31330–31345, DOI: 10.1039/d3ra06137j.

96 F. Rahman, R. Islam and A. Ghosh, Exploring the impact of strain on the electronic and optical properties of inorganic novel cubic perovskite Sr 3 PI 3, *Phys. Scr.*, 2023, **98**(11), 115105, DOI: 10.1088/1402-4896/acfce9.

97 M. Elhadi, *et al.*, Optimization and Comparative Analysis of Electron Transport Layers for High-Performance InGeCl3-Based Perovskite Solar Cells, *ChemistrySelect*, 2025, **10**(26), e01364, DOI: 10.1002/slct.202501364.

98 S. A. Dar and B. S. Sengar, *Strategic Optimization of Gradient-Structured HTL-free Lead-free Double-Perovskite Solar Cells for Enhanced Photovoltaic Performance*, 2025, DOI: 10.1021/acsaelm.5c01211.

99 S. A. Dar and B. S. Sengar, Solar Energy Materials and Solar Cells Breakthrough in sustainable photovoltaics : Achieving 30 . 86 % efficiency with innovative lead-free bilayer perovskite solar cells using SCAPS-1D and DFT framework, *Sol. Energy Mater. Sol. Cells*, 2025, **282**, 113352, DOI: 10.1016/j.solmat.2024.113352.

100 A. I. Shimul, *et al.*, Investigating Optoelectronic Characteristics and Improving the Efficiency of Mg 3 AsBr 3 Perovskite Solar Cells through Machine Learning and Numerical Simulations Utilizing Diverse Charge

Transport, *Materials*, 2025, **3**, DOI: 10.1021/acs.langmuir.5c01821.

101 A. Sikder, A. Ghosh, A. Islam, H. A. Alturaifi and N. S. Awwad, Journal of Physics and Chemistry of Solids Boosting the performances of Mg 3 SbBr 3 -Based perovskite solar cell with machine learning analysis over 27 % utilizing effective transport layers, *J. Phys. Chem. Solids*, 2025, **205**, 112828, DOI: 10.1016/j.jpcs.2025.112828.

102 A. I. Shimul, R. Sarker and A. Ghosh, Exploring the optoelectronic properties and the machine learning driven impact of the hole transport layer on lead-free Ca 3 PCl 3 perovskite, *New J. Chem.*, 2025, **49**, 14300–14321, DOI: 10.1039/D5NJ01856K.

103 M. K. Hossain, M. Rubel, G. F. Toki, I. Alam, M. Rahman, and H. Bencherif, Effect of various electron and hole transport layers on the performance of CsPbI3-based perovskite solar cells: A numerical investigation in DFT, SCAPS-1D, and wxAMPS frameworks, *arXiv*, 2022, preprint, arXiv.2211.02968, DOI: 10.48550/arXiv.2211.02968.

104 M. Li, *et al.*, Modeling and Simulation of MAPbI3-Based Solar Cells with SnS2 as the Electron Transport Layer (ETL) and MoS2 as the Hole Transport Layer (HTL), *ACS Appl. Electron. Mater.*, 2024, **6**(8), 5997–6004, DOI: 10.1021/acsaelm.4c00936.

105 J. H. Im, C. R. Lee, J. W. Lee, S. W. Park and N. G. Park, 6.5% Efficient Perovskite Quantum-Dot-Sensitized Solar Cell, *Nanoscale*, 2011, **3**(10), 4088–4093, DOI: 10.1039/c1nr10867k.

106 A. I. Shimul, B. Chandra Biswas, A. Ghosh, H. A. Alrafai and A. A. Hassan, A study on optoelectronic properties and charge transport layer influence in novel Sr3PF3-Based perovskite solar cells using numerical simulation and machine learning, *Sol. Energy Mater. Sol. Cells*, 2025, **293**, 113838, DOI: 10.1016/j.solmat.2025.113838.